Development of polymer micromachined flapping-wing nano air vehicle using iterative design window search methodology

著者	Rashmi Kant
year	2022-09
その他のタイトル	ポリマー微細加工によって作成される羽ばたき翼微小飛行体のデザインウィンドウ探索法による開発
学位授与年度	令和4年度
学位授与番号	17104甲情工第369号
URL	http://doi.org/10.18997/00009006

Doctoral Thesis

DEVELOPMENT OF POLYMER MICROMACHINED FLAPPING-WING NANO AIR VEHICLE USING ITERATIVE DESIGN WINDOW SEARCH METHODOLOGY

By

RASHMI KANT

Department of Computer Science and System Engineering

Graduate School of Computer Science and System Engineering

KYUSHU INSTITUTE OF TECHNOLOGY, JAPAN

September 2022

Advisory Committee

Professor Daisuke Ishihara, Ph.D. advisor

Professor Akiyoshi Baba

Professor Keisuke Suzuki

Associate Professor Tomoya Niho

Associate Professor Sunao Murakami

ACKNOWLEDGMENTS

First of all, I would like to thank Goddess Shiva to keep me healthy and well. Next, I would like to express my special appreciation and sincere gratitude to my doctoral supervisor **Professor Daisuke Ishihara**, for his precious time, kind support, and patient guidance in supervising this research work. I would like to thank him for giving chance to engage myself in Biomimetic Robotics in the area of Computational Mechanics and for encouraging my research skill to grow as a research scientist. His advice on both research as well as on my career has been essential and priceless. Also, I wish to thank Professor Tomoyoshi Horie and Associate Professor Tomoya Niho for their kind support, invaluable advice, and guidance in research. These professors highly contributed to the completion and improvement of this thesis work. I sincerely thank them for their valuable advice during its elaboration.

I would like to express my gratitude for serving on my doctoral thesis examination committee to Professor Daisuke Ishihara, Professor Akiyoshi Baba, Professor Keisuke Suzuki, Associate Professor Tomoya Niho, and Associate Professor Sunao Murakami. Thank you very much for all the discussions, comments, and advice building up this thesis.

My sincere thanks and appreciation goes to Dr. Prakasha Chigahalli Ramegowda, Mr. Minato Onishi, Mr. Vinay Shankar, Mr. Jyupei Ueo, Mr. Takeru Kumagai, Mr. Ryotaro Suetsugu, and Mr. Ishiba Kazuya for their generous support to carry out research work smoothly. I would like to thank other lab members for being kind and supportive of me.

I like to thank my roommates: Mr. Yutaka Terayama, Mr. Yueh-Hsun Tsai, Mr. Vinay Shankar, and other friends for their continuous support in happily living in Japan which was also much important to keep my mind refreshed.

My deepest and most esteemed appreciation goes to my parents Mr. Satyadev Pratap and Mrs. Rukmini Devi, whose warm support and blessing were essential for fulfilling this work. I would like to thank my late grandmother, my late sister, and my late uncle, they are the real inspiration in my life.

RASHMI KANT

Kyushu Institute of Technology, Japan

TABLE OF CONTENTS

ABSTRACT

The specific flight mechanisms of insects like hovering and maneuverability along with their tiny size nature grasp the attention of many researchers across the globe to utilize the phenomena for the development of biomimetic flapping wing air vehicles which can be used in the wide areas like hazardous environment exploration, rescue, agriculture, pipeline inspection, and earthquake or tsunami disaster management, etc where human access is difficult. Consequently, many researchers have developed flapping wing air vehicles ranging from macro scale to the nanoscale (the largest dimension should be less than or equal to 10 cm) i.e., flapping-wing nano air vehicles (FWNAVs). The research on insect-inspired FWNAVs indicates that FWNAVs generally consist of micro transmission for getting desired flapping motion, a pair of micro wings, an actuator for the power source, and a supporting frame to support the overall structure. Recently, FWNAVs up to a size of 30 mm have been developed based on the insect's size. However, the evolution of insects indicates that the size of ultimate small insects is about 1 mm. The further miniaturization of current FWNAVs is difficult because of the large assembly of components and complicated mechanical transmission mechanism.

Though, there are mainly two difficulties to successfully developing FWNAVs at the scale of mm-size. The first is the manufacturing difficulty because of the very small structure to realize the wing's complicated motions. The second is the design difficulty because of multisystem and involvement of coupled Multiphysics like fluid-structure interaction (FSI) design. Along with these difficulties other difficulty includes enough lift to drag ratio for hover and thrust for forwarding flight motion due to fluid mechanics at low Reynolds no ($Re < 3000$).

These difficulties can be overcome by developing FWNAVs based on a design window search methodology where a design solution can be obtained for the design problem satisfying all the design requirements. Further fabricating the FWNAVs using advanced engineering technologies such as microelectromechanical systems (MEMS) technologies which seem to be suitable for mm-size prototypes.

Computational analysis and design can be utilized for finding the design window search for FWNAVs. The finite element method (FEM) has been the standard choice as a numerical

tool for performing the simulation of Multisystem, because of its capabilities to analyze the geometries of complex shapes, detailed analysis of coupled effect, boundary, and initial conditions.

The purpose of this study is to develop 10 mm insect-inspired FWNAV using a 2.5-dimensional structure novel approach, iterative design window search methodology, and polymer micromachining. The proposed FWNAV consists of a micro transmission with a support frame, a micro wing, and a piezoelectric bimorph actuator. The novelty of this research includes, (1) the novel transmission mechanism using two parallel elastic hinges based on geometrically nonlinear bending deformation that produces a large rotational displacement from a small translational displacement, (2) the complete 2.5-D structure which can be fabricated using the polymer micromachining technique without any post-assembly (3) the novel design approach or iterative design window (DW) search method using the advanced computational analysis and design. The advantage of the proposed FWNAV over other FWNAVs includes the lowest energy loss due to no post assembly (friction loss is less), reducing total weight, ease in miniaturization, and enough performance without resonance mechanism. In order to develop the proposed FWNAV, firstly I have designed micro transmissions with a support frame and micro wing and later I have designed FWNAV which has been further miniaturized to design 10mm FWNAV using the iterative DW search method. I have also estimated fatigue life arising due to random cyclic stress, which is mostly ignored by the researchers. Computational flight performance of the proposed FWNAV has been evaluated using Multiphysics coupled analysis i.e., fluid-structure interaction analysis where governing equilibrium equation of motion of micro wing and surrounding airflow has been directly solved by finite element methods. The computational flight performance indicates that mean lift force is comparable to the weight of FWNAV which provides that the proposed FWNAV can lift off. The polymer micromachining has been demonstrated by fabricating the transmission which is a key and central component of FWNAV which indicates the feasibility of polymer micromachining for the development of 10 mm FWNAV. Thus, 10 mm flyable FWNAV can be developed which has enough fatigue life.

LIST OF FIGURES

FIGURES Page

FIGURES Page

FIGURES Page

FIGURES Page

FIGURES Page

LIST OF TABLES

TABLE Page

CHAPTER 1

GENERAL INTRODUCTION

1.1 Motivation

Bird's and insect's flights have attracted the attention of many scientists and researchers across the globe to utilize the phenomena of flying mechanisms for developing engineering alternatives to nature's solutions. Consequently, fixed-wing flight systems have been developed which have the advantages like carrying higher payloads and having a longer endurance but these flights required large space for their take-off and landing. As a result, rotary-wing flight systems have been developed which are useful for wide space applications only. Hence, the researcher has tried further to reduce its size from macro to micro scale for confined space applications where human access is impossible [1].

In 1997, the United States Defence Advanced Research Projects Agency (DARPA) announced its 'Micro Air Vehicles (MAVs) program which defined a MAV as an unmanned aerial vehicle with the largest linear dimension of 15 cm and should have good flight performance including flight range of 10 km, peak velocities over 13 m/sec and minimum endurance time 20 minutes [2]. Therefore, various fixed-wing and rotary-wing type MAVs [2–7] have been developed like the *Black widow* MAV [2] a prototype of a fixed-wing type MAV has been developed by AeroVironment Inc. while *Micro coaxial Rotorcraft* (MICOR) [7] a prototype of a rotary-wing type MAV, has been developed by Alfred Gessow Rotorcraft Centre (University of Maryland). Since, fixed-wing type MAVs can't hover and have poor collision avoidance characteristics so they can be used for outdoor surveillance, such as monitoring streets [8]. While rotary-wing type MAVs can hover but they can't maneuverer and have poor collision properties with walls so they have the limited indoor application [8].

The research on flapping-wing type air vehicles became necessary and important for confined space applications like hazardous environment exploration where maneuverability and hovering characteristics of flight systems are essential [9]. So, flapping-wing air vehicles have been developed ranging from macro to micro scale [10–18]. There are two main types of flapping wing

air vehicles [9]: the first is a bird-like air vehicle or the 'Ornithopter' e.g. *DelFly*, a prototype developed by the Delft University of Technology [19], and the second is insect-like air vehicles or the 'Entomopters' such as *RoboBee*, a prototype developed by Wood Group (Harvard University) [20]. Entomopters have good maneuverability and better hovering efficiency than ornithopters because insects can perform vertical take-offs and hover more easily than birds [21].

Insects have specific characteristic motions including feathering, flapping, and wingtip path for hovering and maneuvering. The flapping and feathering of insect motion are shown in Fig. 1.1 [22]. In this figure, the oscillatory motion of wings especially the leading-edge along the out of plane direction demonstrates the flapping motion whereas the relative motion of the wing membrane with respect to the leading-edge demonstrates the feathering motion.

In order to increase 30% endurance and 20% more payloads than the current MAVs [23], DARPA pushed the limits of unmanned aerial vehicles by announcing the 'Nano-Air Vehicle' program in 2005, which had the requirements of 10 g or fewer vehicles with 10 cm maximum dimension, able to fly 1 km or more. Consequently, many researchers and scientists have developed flapping-wing nano air vehicles across the globe for applications like rescue, earthquake, or tsunami disaster management [24–29]. Thus, research on flapping-wing nano air vehicles (FWNAVs) is important because of their advantages over other types in miniaturizing air vehicles [21]. The research on insect flight mechanics indicates that the FWNAVs with a wingspan of less than 15 cm will produce better flight performance [29, 30].

Fig. 1.2 shows the scale of all familiar flying objects in which the weight of the flying object is plotted against its wingspan, adapted from Ref. [31]. From this figure, it is clear that heavier flying vehicles or creatures have wider wingspans so that they can generate more lift to offset their mass. Large flying objects like an airplane and helicopters usually weigh several tons or more due to the need for a high payload. Conversely, smaller vehicles such as MAVs and NAVs are commonly used for data collection, so the payload is not a key criterion. The lower bounds of weight and wingspan of NAVs are nowadays limited by technology and the evolution of insects [32]. Similarly, the Reynolds number and the mass of flying objects have a strong relationship [33] as shown in Fig. 1.3, adapted from Ref. [33]. From this figure, it is observed that the Reynolds number is continuously decreased from the larger flying objects to the MAVs and NAVs and the unsteady aerodynamic mechanism increases as the mass of the flying object decreases [33].

By understanding flapping flight at the low Reynolds number region, it was

found that lift producing mechanisms are intrinsically unsteady and vortex-dominated, some of the unsteady mechanisms are clap-and-fling [34–38], leading-edge vortex (LEV) [39–42], rotational lift [39, 43], wake capture [39, 44], wing-wing interactions, and body-wing interactions [45].

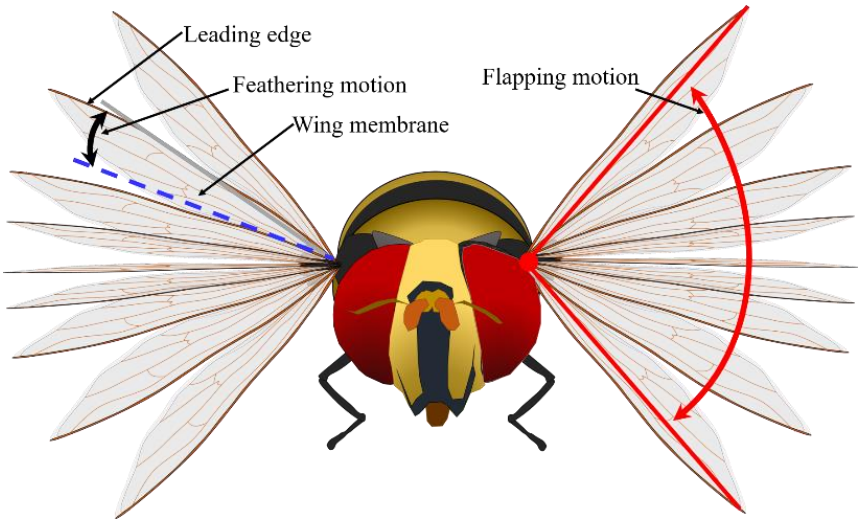

Figure 1.1: Schematic view of insect's flight mechanism and its characteristic motions

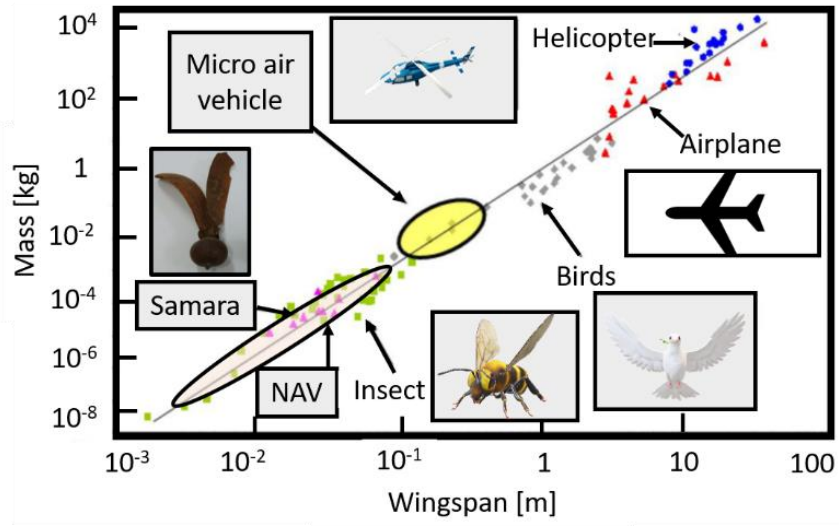

Figure 1.2: MAVs and NAVs design range compared to other flying objects, adapted from Ref. [31]

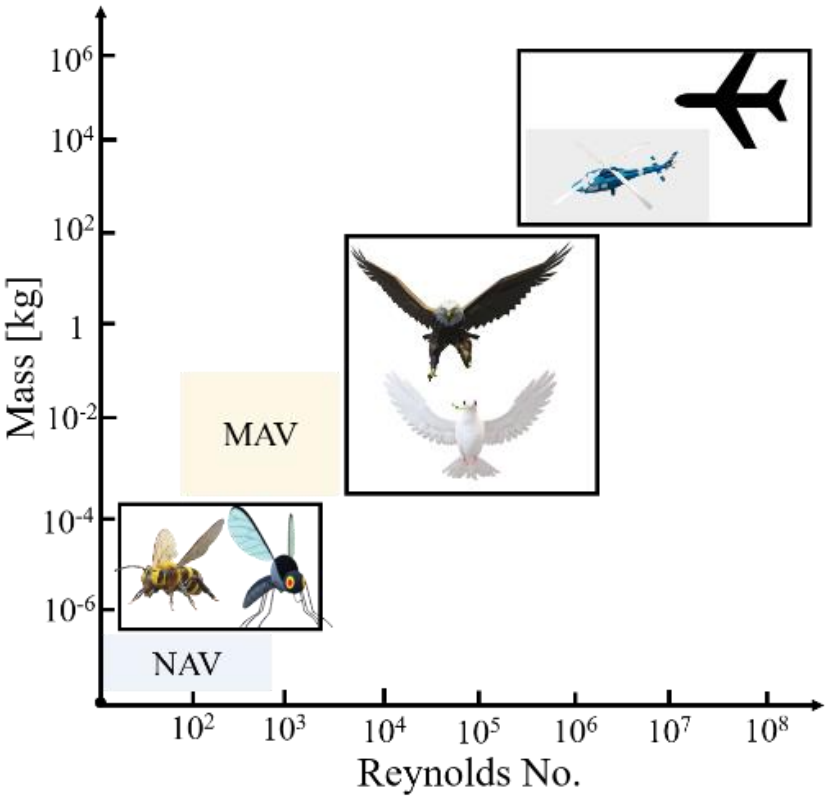

Figure 1.3: Relationship between Reynolds number and mass of the flying objects, adapted from Ref. [33]

Due to these characteristics and advantages of the insect-inspired flapping air vehicles, I have focused my attention on the research about biomimetic FWNAVs. Though, designing and developing FWNAVs is difficult because of two important aspects; first is the design aspect due to multisystem and Multiphysics coupled analysis like electro aeromechanical design [46, 47], and the second is the fabrication difficulty because of a very small structure to realize the wing's complicated motion and assembly of the components. The other problem includes fluid mechanics at a low Reynolds number (Re < 1000) [9] to produce enough lift force to support the weight of FWNAV.

These challenges can be overcome by utilizing the computational biomimetic concept [46, 48, 49] for the design of FWNAV which includes Multiphysics and multisystem strong coupled analysis (Fluid-structure-electric-circuit interaction analysis) and fabrication of FWNAVs using micro-electro-mechanical system (MEMS) technology i.e., standard microfabrication techniques including etching, photolithography, deposition, and curing [50–54]. The existence of computational methods and fabrication technology with the emergence of fast-growing technology shows the evidence that the development of FWNAVs is possible

which further motivates me to focus my attention on this topic.

Fig. 1.4 shows the concept of FWNAVs surrounded by fluid media which will be fabricated using MEMS technology [55, 56], hence it can be called a MEMS flyer too. Fig. 1.4 indicates that FWNAVs will consist of a transmission mechanism for producing desired flapping motion, a pair of micro wings, an actuation mechanism for working as a power source, and a support structure [55, 56] for providing the strength to the overall structure.

In order to develop FWNAV, the other objective that motivated me for this research includes the study of fluid mechanics of flapping flight [46, 57–61], understanding of computation methods, and software technology used for the design of the structures [9, 46, 48, 56, 62–65], insight about the microfabrication technique [50, 54], experience in experimental studies, and the last design window search methodology because of Multiphysics and multisystem coupled analysis [63, 66]. These studies, experience, and understanding can be utilized to design and develop other engineering devices.

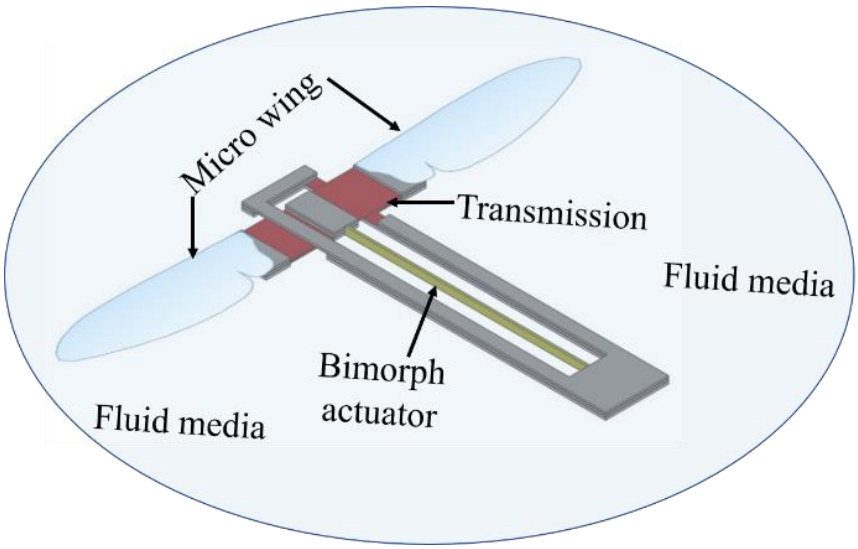

Figure 1.4: MEMS Flyer

1.2 Model Insect

In order to design and develop insect-inspired FWNAVs, the selection of model insects is very important because of their actual realization and replication. The design of FWNAVs depends upon the model insect's aerodynamic mechanism, which depends upon the morphological and kinematics parameters of the insect [67]. Depending upon the shape, size, and flight mechanism, insects are divided into different orders like Dipterans, Hymenopterans, Neuropterans, Odonatans, etc [68]. However, dipteran insects such as *Eristalis tenax* (drone fly), *Episyrphus balteatus* (hoverfly), *Tipula obsolete* (crane fly), and *Drosophila Melongster* (fruit fly) are especially proficient at hovering [69] and maneuvering [70]. The morphological and kinematic parameters of these dipteran insects are discussed here because the kinematics and flight mechanism [71] of each insect are different from one another and one of them is used in this thesis for the design of FWNAV. They are discussed as follows:

a. *Eristalis Tenax*: A drone fly usually hovers in the horizontal stroke plane (stroke plane inclined at about 13° from the horizontal plane) and the insect can maneuver sharply [70]. The lift coefficient of this insect is about 2.2-2.6 because the feathering angle is about 40°-55° [70]. The actual image of this insect and its wing morphology can be seen in Refs. [72, 73, and 74]. Understanding of wing morphology and body is needed for the approximate replication during the design of the FWNAV. Based on the detailed literature survey of the Refs. [69, 70, 73–75], the morphological and kinematic parameters of this insect are given in Table 1.1, which is required for the design of FWNAVs, especially in order to design the size of the micro wing and keep the mass of FWNAV equivalent to model insects.

Table 1.1: Kinematic and morphological parameters of the drone fly [70]

Span length (L_w) (mm)	Mass (mg)	Aspect ratio (r_a)	Dimensionless radius of second-moment area (r_2)	Stroke angle (°) (Φ)	Flapping frequency (f) (Hz)
10.8–11.5	95.0–103.6	6.87–7.30	0.53–0.54	86–107	169–183

b. *Episyrphus balteatus*: Hoverfly can hover in the horizontal as well as inclined stroke planes [69, 73] and they have high and rapid maneuverability [69]. The actual shape or body of the hoverfly can be seen in Ref. [76] while the wing morphology of the hoverfly can be checked from Ref. [77]. It is observed that the wing of the hoverfly has two distinct wing areas: the upper part is stiff and the lower part is flexible [73] and this morphology gives the flip motion to the wing [78]. The need of understanding the shape of insects and wing morphology are important in a similar way as discussed above. As per the literature survey of the Refs. [69, 73, 75, 77], the morphological and kinematic parameter of the hoverfly is given in Table 1.2.

c. *Tipula obsoleta*: The crane fly possesses a larger aspect ratio and lower Reynolds number [69, 79] compared to other dipteran insects. The lateral disturbance motion of a model crane fly in hover consists of three natural modes, and the flight in lateral dynamics is nearly neutral, which is different from most other insects. In order to see the actual shape of the crane fly and its wing morphology, one can go through Ref. [80]. A detailed literature survey [69, 75, 78, 81], provides the morphological and kinematic parameters of the crane fly which is tabulated in Table 1.3.

Table 1.2: Kinematic and morphological parameters of the hoverfly [69, 73, 75, 77]

Span length (L_w) (mm)	Mass (mg)	Aspect ratio (r_a)	Dimensionless radius of second-moment area (r_2)	Stroke angle (°) (Φ)	Flapping frequency (f) (Hz)
7.7–10.2	14.0–51.5	7.92–8.73	0.56–0.57	69–90	144–166

Table 1.3: Kinematic and morphological parameters of the crane fly [69, 73, 78, 81]

Span length (L_w) (mm)	Mass (mg)	Aspect ratio (r_a)	Dimensionless radius of second-moment area (r_2)	Stroke angle (°) (Φ)	Flapping frequency (f) (Hz)
12.7–13.7	11.4–19.0	10.45–10.93	0.60	123	45.5

d. *Drosophila Melongster*: A fruit fly usually hovers with an inclined stroke plane i.e., about 60° with the horizontal plane [82]. This can be a very interesting insect because of its small wingspan size which can be utilized for the design of very small FWNAVs. The flight performance of the fruit flies has attracted considerably because the conventional aerodynamics predicts a reduction of flight efficiency when the wingspan size is very small [83, 84]. The shape of the fruit fly can be seen in Ref. [85] while its wing morphology can be visuals in Ref. [86]. Based on the detailed literature survey [69,70, 73, 83, 84, 87, 88] about the fruit fly its morphological and kinematic parameters are presented in Table 1.4.

These morphological and kinematic parameters are very important data for the design of FWNAV and to evaluate the flight performance such as lift and power requirements using various aerodynamic models [89–91].

1.3 State of the art of flapping wing nano air vehicle

Nowadays many scientist and researcher across the world are trying their best to develop FWNAV because of its application in wide areas such as rescue, entertainment, etc and it became possible due to rapid development in science and technology.

There are mainly two difficulties in developing FWNAV, the first is the design difficulty due to multisystem and Multiphysics coupled analysis and also insufficient lift force due to fluid mechanics of wing motion at low Reynolds number (Re < 2000) and the second is the manufacturing difficulty at the few mm-size scales [92] along with the assembly of various components.

One engineering concern in the development of FWNAVs is the reduction of their size, potentially down to the scale of the minimum insect size, which is approximately 1 mm considering the evolution of insects; this is our goal for FWNAV development [9]. Fluid mechanics of wing motion is very complex in FWNAV because of the low Reynolds number (Re < 2000) [93] as shown in Fig. 1.5, so lift to drag ratio is reduced and this makes the FWNAV difficult to fly [9].

Currently, various FWNAVs have been developed [94–112] using various transmission mechanisms and power source systems. Here, I have discussed mainly three FWNAV developed by three different groups which are a milestone in this research field.

Table 1.4: Kinematic and morphological parameters of the fruit fly [70]

Span length (L_w) (mm)	Mass (mg)	Aspect ratio (r_a)	Dimensionless radius of second-moment area (r_2)	Stroke angle (°) (Φ)	Flapping frequency (f) (Hz)
2.02	0.72	6.37	0.55	136–162	254–229

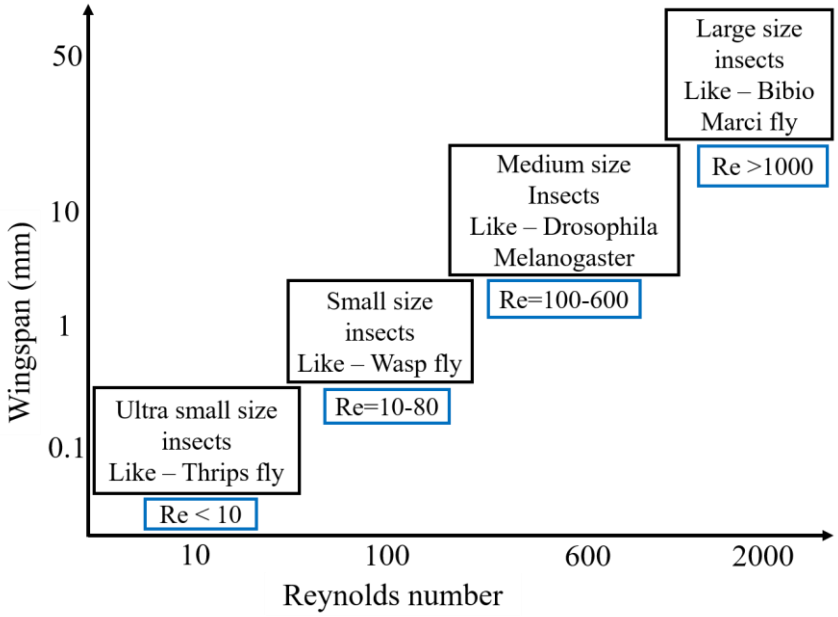

Figure 1.5: Wingspan plotted against Reynolds number, adapted from Ref. [93]

The first is the *RoboBee* first prototype of FWNAV with a wingspan of 3.5 cm which can lift off, developed by the Wood Group (Harvard University) [20]. This FWNAV can't be further miniaturized because it required the assembly of various components at different stages [20]. The Wood Group has developed a series of 'RoboBee' with different wingspan sizes varying from 3–6 cm but in these cases, they have used complex mechanical transmission mechanisms so their further miniaturization is difficult.

The second is the *SU-8 FWNAV* with a wingspan of 3 cm developed by the Canttan Group (University of Valenciennes) [111]. Although this FWNAV is developed using MEMS technology, it is based on a thoracic transmission mechanism that is actuated by an electromagnetic actuator, hence its further

miniaturization is difficult. This group has also developed a series of *SU-8 FWNAV* using the same technology and mechanism hence their FWNAV can't be further miniaturized. Sometimes they have used resonance mechanism to improve the performance which complicates its fluid-structure interaction design [55]. The concept of the thoracic transmission mechanism has been discussed in Chapter 2.

The third and final is the *Flapping-wing Actuator* with a wingspan size of 3-5 cm developed by Ozaki Group (Toyota Central R&D Labs) using MEMS technology, resonance mechanism, and a unimorph piezoelectric actuator power source [112]. Its flight performance is very low. Since it is based on the resonance mechanism which complicates its fluid-structure interaction design [55]. Note that most of the current developed FWNAVs are tethered flights except one FWNAV, developed by Wood Group which is an example of an untethered flight [95].

1.4 Objective

As per the study of the literature survey in the previous sections, inset-inspired FWNAVs have various advantages and they can be developed using MEMS technology so the ultimate goal of this thesis is to design and develop insect-inspired FWNAVs using MEMS technology and polymer material [20, 55, 56, 115].

The conceptual design of our FWNAV is shown in Fig. 1.6 which indicates that FWNAV is a complete 2.5-dimensional structure that can be easily fabricated using standard microfabrication steps like the deposition, the lithography, the etching, and the curing without any post-assembly [56]. The main components of our FWNAV are a micro transmission (to enhance and convert the displacement from the biomorph actuator), a piezoelectric bimorph actuator (a power source), a pair of micro wings, and a support frame (to support the overall structure) [56].

In order to develop FWNAV, its main components: micro transmission with support frame and micro wings are designed and developed following an individual research flow which is shown in Fig. 1.7, and according to that the development of FWNAV is divided into different sub-objective. Hence, the sub-objective of this thesis is given below;

1. Design of a 2.5-dimensional micro transmission with a support frame to convert the translational displacement from the bimorph actuator into rotation displacement using nonlinear static structural analysis such that micro

transmission should not break during fabrication and actual working. Evaluate the flapping performance for quasi-static actuation of the proposed transmission, demonstrated in Chapter 2.

2. An iterative design window (DW) search method should be proposed for accompanying the change in design problems which is the essential characteristic of 2.5-dimensional FWNAV. In order to obtain the DW for FWNAVs that satisfy all the necessary design requirements (DRs) like large stroke angle, and safely flap, using the above-mentioned method, sub-design windows should be searched. Firstly, DW should be searched for the mass of the micro wing which can be supported by micro transmission considering an inertial effect, and secondly, DW should be searched for miniaturizing the FWNAV (micro wing + micro transmission) using nonlinear structural dynamic analysis, as discussed in Chapter 3.

3. Computation flight performance of the FWNAVs should be evaluated using nonlinear structural dynamic and fluid-structure interaction (FSI) analyses. Flight performance should be further optimized by designing the wing membrane thickness for large stroke angle and high flapping frequency using FSI analyses, as described in Chapter 4.

4. In order to fabricate the designed FWNAVs, the feasibility of polymer micromachining should be demonstrated. Micro transmission can be fabricated using polymer micromachining as a demonstration since transmission is a key and central component of FWNAV, discussed in Chapter 5.

Thus, in order to develop FWNAVs, we have designed a micro transmission in Chapter 2 which is the base for Chapter 3 where we have designed FWNAVs using an iterative design window search methodology. Further flight performance of the designed FWNAV is evaluated numerically in Chapter 4. Finally, FWNAV has been developed using polymer micromachining in Chapter 5 where the micro transmission has been developed as a demonstration of the polymer micromachining. Thus, flyable FWNAV has been developed.

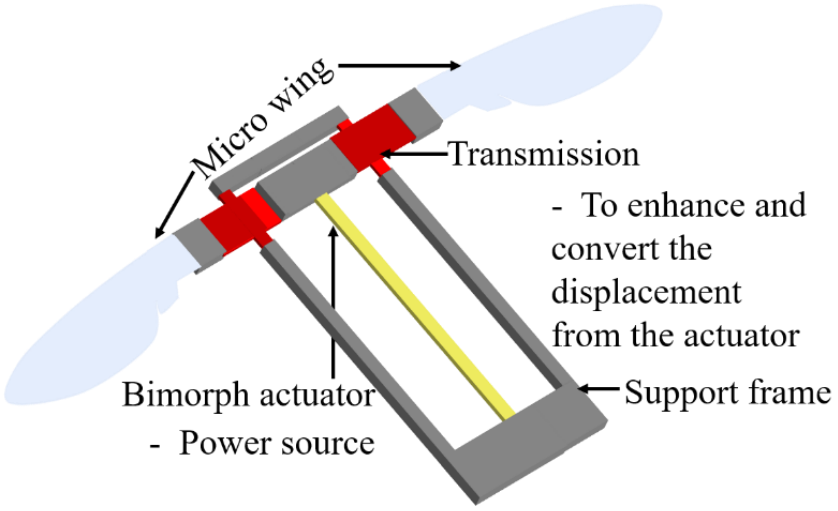

Figure 1.6: Concept of polymer micromachined FWNAV [56]

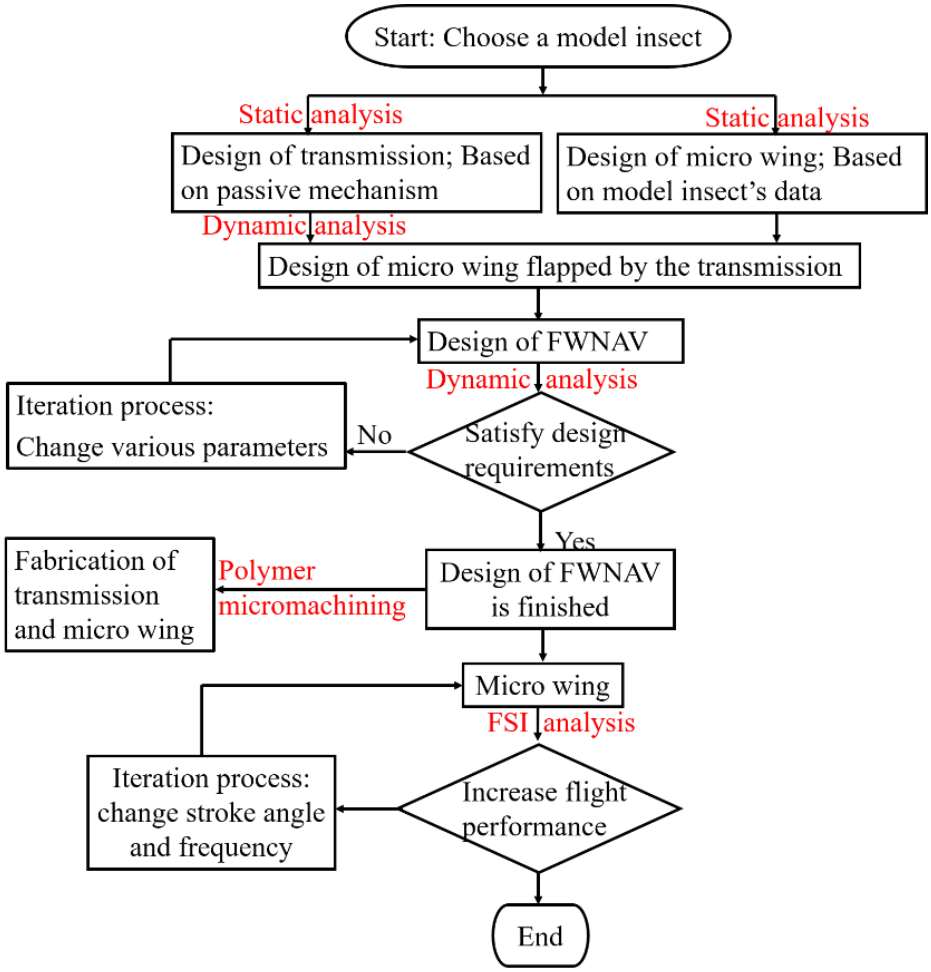

Figure 1.7: Research flow for the development of polymer micromachined FWNAV

1.5 Outline

In the study, FWNAVs have been designed and developed using nonlinear structural analysis, design window search technology, and polymer micromachining, respectively. Flight performance of the FWNAVs has been evaluated using computational methods such as nonlinear structural dynamics and FSI analyses. As per the research flow shown in Fig. 1.7 discussed in the previous section, an outline of this thesis is organized as follows;

In Chapter 2, A one-wing transmission has been proposed that should not break during microfabrication and actual working. The proposed transmission mechanism has been compared with other transmission mechanisms to show its advantage. Firstly, the proposed transmission has been designed using nonlinear static structural analysis, and later its flapping performance for quasi-static actuation has been evaluated.

In Chapter 3, an iterative design window (DW) search methodology has been proposed using nonlinear dynamic analysis to design the FWNAVs. Following the methodology, firstly a DW has been searched for the transmission using nonlinear dynamic analysis, and then the mass of the micro wing which can be supported by this transmission has been formulated as a DW search result. Secondly, the basic design of the micro wing has been obtained using the model insect morphological and kinematic parameters data, this basic design has been further extended to formulate the DW for the detailed design of the micro wing using the linear static analysis and mass limit supported by the transmission. Finally, the initial design of FWNAV has been obtained by combining the design solution of micro transmission and micro wing which has been further elaborated and reduced into FWNAV without membrane for reducing the computational cost during parametric studies and to obtain a DW for the miniaturization of FWNAV. In the end, the design of a piezoelectric bimorph actuator has been discussed as per the miniaturization of FWNAV and the fatigue life has been estimated for the final miniaturized FWNAV design solution.

In Chapter 4, the FSI design has been proposed to evaluate the flight performance of FWNAVs. In view of this, firstly FSI methodology has been discussed. Secondly, flight performance from nonlinear structural dynamic and FSI analyses have been compared to show the sufficiency of FSI with a micro

wing over FSI with FWNAV for evaluation of flight performance and to avoid the computational complexity associated with the latter one. Finally, the wing membrane thickness has been designed to optimize the flight performance for large stroke angles and high flapping frequency.

In Chapter 5, the development of FWNAVs has been demonstrated by the fabrication of micro transmission using polymer micromachining. The performance of fabricated transmission has been evaluated using finite element analysis which is validated using an experimental static driving test. The precision of the fabricated transmission has also been measured using a micrometer. The effect of the precision of the fabricated transmission on its performance has been finally studied.

Finally, some general conclusions are drawn based on the results and discussions and summarized in Chapter 6.

CHAPTER 2

PROPOSAL OF 2.5-DIMENSIONAL ONE WING TRANSMISSION FOR FLAPPING-WING NANO AIR VEHICLE

2.1 Introduction

In Chapter 1, we have discussed the importance of the development of insect-inspired flapping-wing nano air vehicles (FWNAV). However, a slight description of insect-inspired FWNAVs has been made here considering the comparative study between previous research and the novel approach used in this study. During the flapping flight, insects rotate their wings at a specific time during the flapping cycle to generate a sufficient lift force [39, 43, 67, 113]. To emulate these wing movements, a flexible hinge that enables passive wing rotation is adopted in artificial insects because of its simple structure and ease of fabrication [20, 107–109, 114–117]. Many artificial insects have been developed with the passive wing rotation mechanism for flapping flight, and the most notable example is the 'RoboBee' [20]. However, in these state-of-the-art artificial flapping-wing insect demonstrations, post-assembly is required, which limits further miniaturization. To overcome this issue, a flexible hinge transmission system is employed in our research without the need for post-assembly.

The development of FWNAV required its conceptual, basic, and detailed design before proceeding with its fabrication, and generally, FWNAVs consist of a power source, actuators, transmission mechanisms, wings, and a supporting structure [20, 29, 51–53, 105–109, 118, 119]. In order to produce sufficient lift force to support the weight of FWNAV, requires a large stroke angle and high flapping frequency in a region of low Reynolds Number otherwise it will be difficult to fly [36, 70, 78, 93, 120, 121].

In order to produce a large stroke angle, the design of the transmission mechanism structure is the most important factor [122] because the role of the transmission mechanism in actuator-driven FWNAVs includes the conversion of

rotational or translational motion of actuators into desired flapping motion as well as enhancement of motion. Hence, the transmission mechanism must be designed in such a way that it should possess higher strength and reliability to absorb high impact and friction [123] because the transmission mechanism needs to operate on a high flapping frequency to produce sufficient aerodynamic forces and ensure the reliability and efficiency of FWNAVs. Therefore, the life and performance of FWNAVs directly depend upon the design of the transmission mechanism and its performance.

Nowadays, different kinds of transmission mechanisms are used for insect-inspired FWNAVs/FWMAVs in which some of them are very complicated mechanical transmission systems such as dual series four-bar linkage and string-based designs [124], the six-bar linkage design [125], the rack-pinion mechanism [126] and the Watt straight-line linkage system [127] whereas some of them are very simple such as compliant mechanism which contains flexural joints, segments or other elastic components [12, 128, 129]. Compared to the mechanical transmission system, a compliant transmission system has various advantages like no wear and tear, no friction and backlash, and is compatible with the fabrication using micro-electro-mechanical system (MEMS) technology [130, 131]. These advantages make compliant mechanisms using elastic hinges with MEMS technology suitable for developing FWNAVs and a similar phenomenon has been adopted in this thesis.

The theme of this chapter is based on a proposal of a transmission mechanism structure for insect-inspired FWNAVs. In order to achieve that target firstly, various transmission mechanism has been compared with our transmission mechanism which is based on a parallel elastic hinge and large nonlinear bending deformation [56]. Later an improved version [62] of the previous transmission mechanism [56] has been proposed to increase the fabrication stability which leads to an increase in yield ratio and also accurate prediction of flapping performance.

This transmission mechanism will be used in developing insect-inspired FWNAVs where the proposed transmission and bimorph actuator drive each wing of the FWNAVs separately. A piezoelectric bimorph actuator with a metal shim was used to accurately evaluate the forced displacement applied by the actuator to the transmission and to further produce a large flapping motion by the transmission mechanism in the development of FWNAVs because other motions, such as the feathering motion, can be produced by the fluid-structure interaction (FSI) [55, 57, 58, 132–135]. Since our FWNAVs is based on dipteran insect which operates their wing strokes at the natural frequency of the thorax-wing assembly

including the surrounding air [136–139], which aspect can be used to increase the stroke angle further [20, 140] in the proposed transmission in our future work.

2.1.1 State of the art of transmission mechanism

As discussed above that various kinds of transmission mechanisms have been employed for FWNAVs to obtain the desired flapping motion of the wings. Here, I have been discussing three different transmission mechanism which is widely used by the various researcher in developing insect-inspired and actuator-driven FWNAVs and finally compared them with our transmission mechanism. The reason for selection for discussion of these transmission mechanisms is based on the fact that the developed FWNAVs using these transmission mechanisms are insect-inspired and actuator driven which is similar to our objective i.e., development of insect-inspired and actuator-driven FWNAV.

a. Four-bar transmission mechanism

This transmission mechanism is based on four-bar linkage or simply known as four-bar closed-chain movable linkage. In this linkage, four bars or four links are connected in a loop by four pairs of hinges or turning joints. Fig. 2.1 shows the four-bar mechanism, as shown in this figure one link would be completely fixed while other links can easily rotate. This is used to convert rotary motion to reciprocating motion and vice versa. There are various insect-inspired and actuator-driven FWNAVs have been developed using this transmission mechanism [25, 26, 28, 97, 105, 106, 119, 122, 141]. However, further miniaturization of the developed FWNAVs using this transmission mechanism would be difficult because of fabrication difficulty as well as assembly of its components.

b. Slider crank transmission mechanism

This is also similar to a four-bar kinematic chain or linkage which has four links but they are connected using three pairs of hinges or turning joints and one pair of sliding joints. Fig. 2.2 shows the crank slider kinematic mechanism which is used to convert the rotary motion to reciprocating motion and vice versa. Various insect-inspired and actuator-driven FWNAVs/FWMAVs have been developed using crank-slider transmission mechanisms [94, 98, 99, 119, 122, 142] but their further miniaturization would be difficult because of the difficulty in fabrication as well as assembly of components.

Note that it may be possible that some FWNAVs/FWNAVs may fall into a four-

bar transmission mechanism or slider-crank mechanism because the mechanism employed in developing FWNAVs/FWMAVs was not categorized.

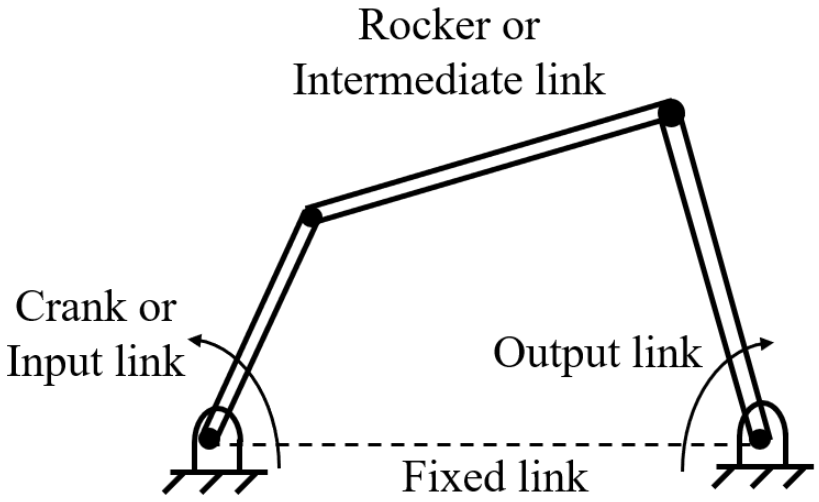

Figure 2.1: Schematic diagram of the four-bar transmission mechanism

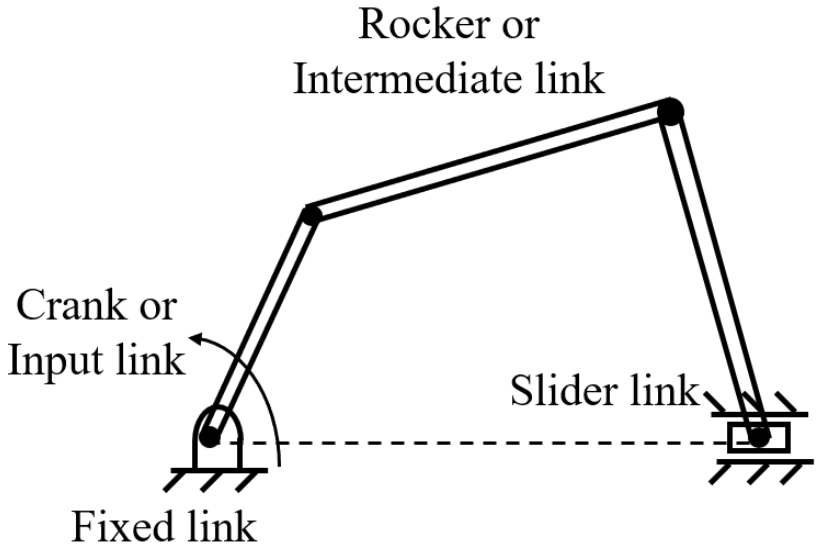

Figure 2.2: Schematic diagram of the slider-crank transmission mechanism

c. Thoracic mechanism

This is based on the actual insect's thorax structure which consists of light and thin composite shells and plates or simply muscles in a closed box [143–145] as shown in Fig. 2.3. Muscles can be two types; direct muscle or indirect muscles and wing flight has been achieved due to the contract and expansion of these muscles. There are some FWNAVs/FWMAVs have been developed using this phenomenon (contraction and expansion of component, especially coupled with the electromagnetic actuator) [20, 52, 103, 119, 122, 146–148]. However, their further miniaturization is difficult because of the fabrication difficulty.

d. A parallel elastic hinge transmission mechanism

Fig. 2.4 shows the basic design of the parallel elastic hinge transmission mechanism which is based on the geometrically nonlinear bending deformation [56]. As shown in Fig. 2.4, this transmission consists of (1) the paralleled elastic hinges, (2) the beams supporting the elastic hinges, (3) the wing attachments, and (4) the actuator attachment. From this figure, one can understand that a small translational displacement from the actuator produces a large rotational motion. Due to the symmetricity of the two sets of the parallel elastic hinges about the actuator attachment cancels their reaction moments acting on it. Since this transmission is a 2.5-dimensional structure, it can be easily fabricated using the standard microfabrication technique and can be easily miniaturized.

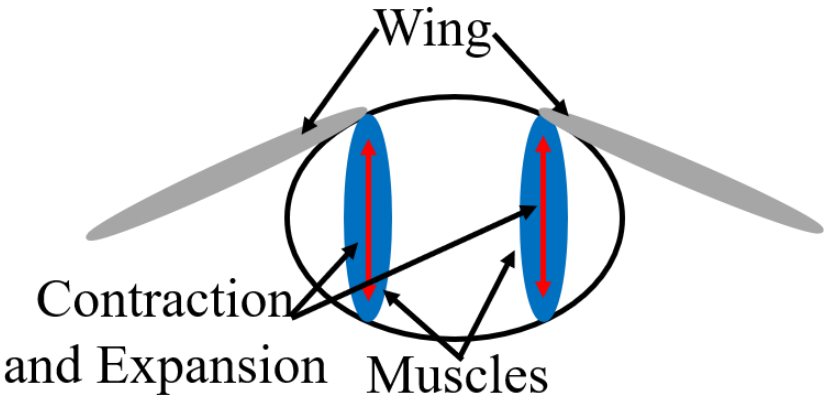

Figure 2.3: Schematic diagram of the thoracic transmission mechanism

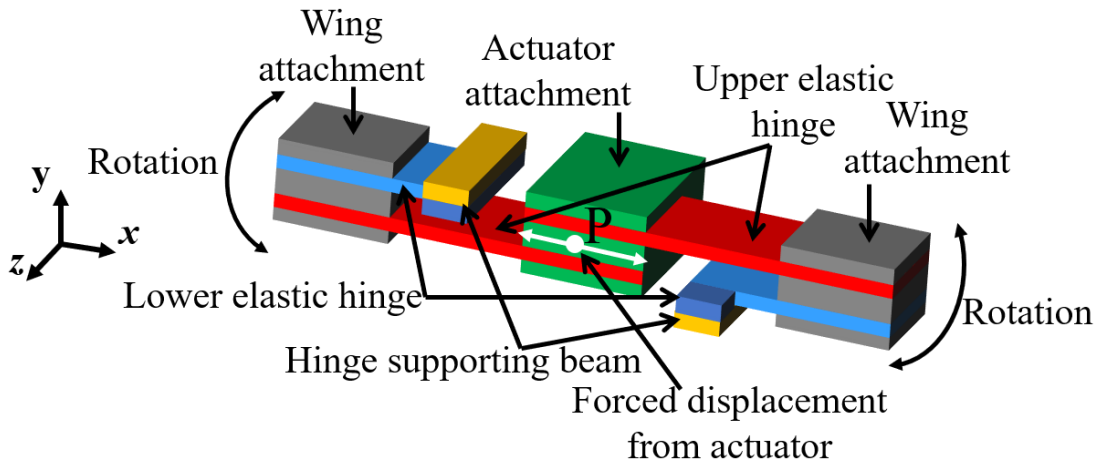

Figure 2.4: Basic design of parallel elastic hinge transmission mechanism adopted from Ref. [56]

2.1.2 Proposal for 2.5-dimensional one wing transmission

Fig. 2.5 shows the plain and cross-section views of two-wing type polymer micromachined transmission. A series of two-wing type transmissions have been fabricated using the polymer micromachining method and polyimide adhesive sheet as shown in Fig. 2.6 [56] by changing the position of the elastic hinge and reducing the hollow structure. Fig. 2.7 shows the hinge part of the fabricated transmission where most cracks occur and a corresponding cross-sectional view of the transmission to understand the position of the elastic hinge. A summary of the fabrication result and reason for the crack is given in Table 2.1. In the microfabrication process, the various types of stresses are caused in the polyimide sheets and lead to fracture of the elastic hinges. The out-of-plane stress in the lamination steps causes the cracks in the parts of the polyimide sheets forming the hollow structures. The fluid traction force in the development causes cracks in the elastic hinges. The shrink of the supporting frame due to the curing causes the tension of the beam supporting the elastic hinge, and the tensile stress concentrates in the corner of the boundary between the elastic hinge and the supporting beam to fracture them [56].

Since cracks mainly occur in the upper T-shaped elastic hinge layer (sensitive layer), see Fig. 2.5, due to stress generation caused by the presence of the hollow structure and acting fluid traction forces during the development process so the position of the sensitive layer can be modified to avoid the hollow structure.

Thus two-wing type transmission has been improved and one wing type

transmission has been proposed as shown in Fig. 2.8. In this figure, the sensitive layer (T-hinge layer) has been kept adjacent to the base layer for avoiding the gap which will increase the fabrication stability and that lead to an increase in yield ratio. Thus, the proposed transmission or one wing transmission can be easily fabricated because of the 2.5-dimensional structure without any post assembly, and also the occurrence of cracks will reduce.

In the next section conceptual design of FWNAV using the proposed one wing transmission and the basic mechanism of the proposed transmission have been discussed. In the subsequent section, detailed design and static structural analysis for a quasi-static actuation of the proposed transmission have been discussed.

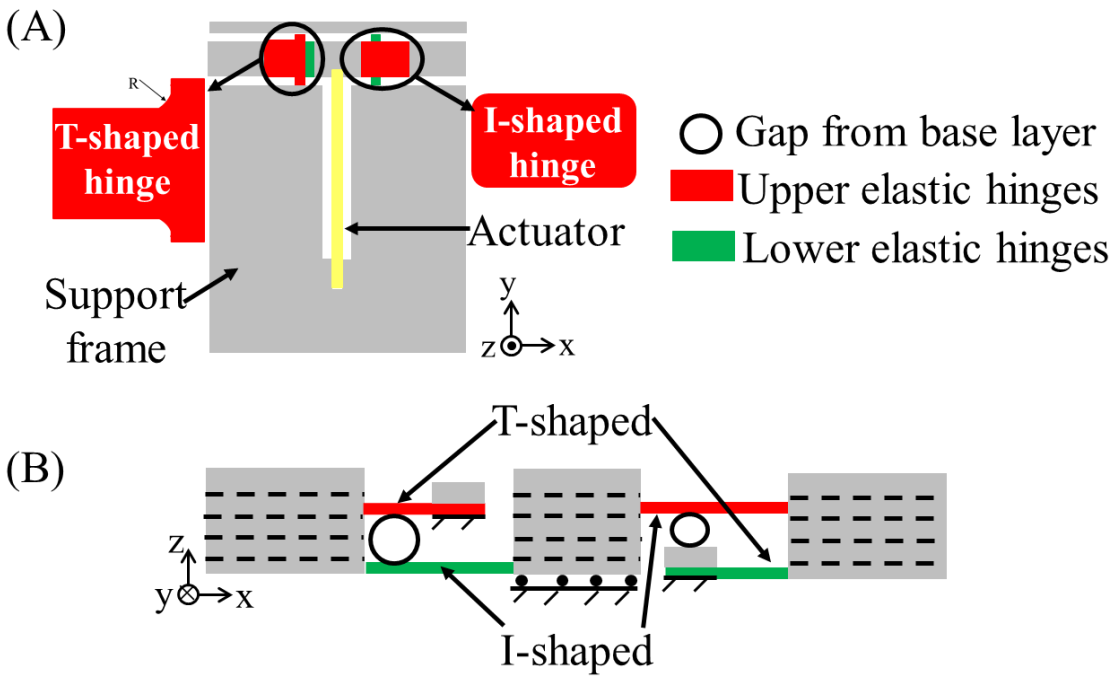

Figure 2.5: Two-wing type transmission in plain view (A) cross-sectional view (B)

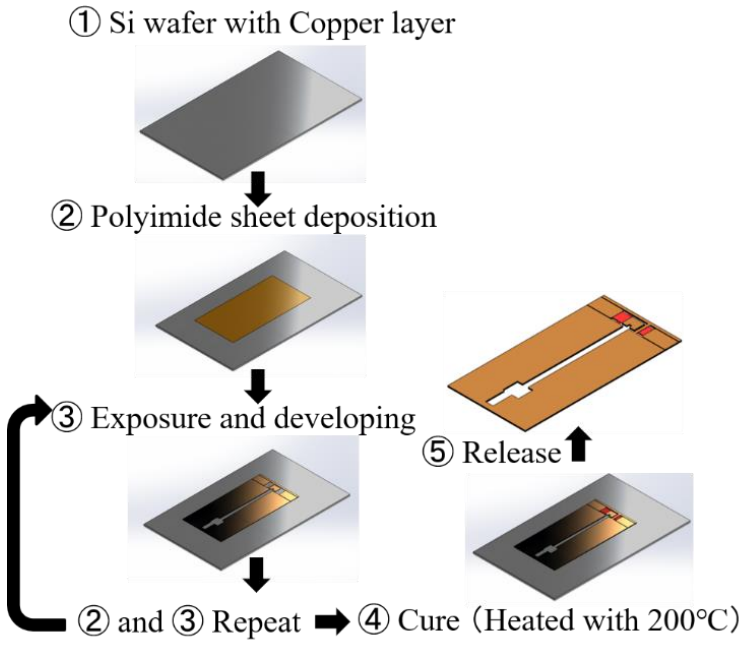

Figure 2.6: Polymer micromachining process for two-wing type transmission adopted from Ref. [56]

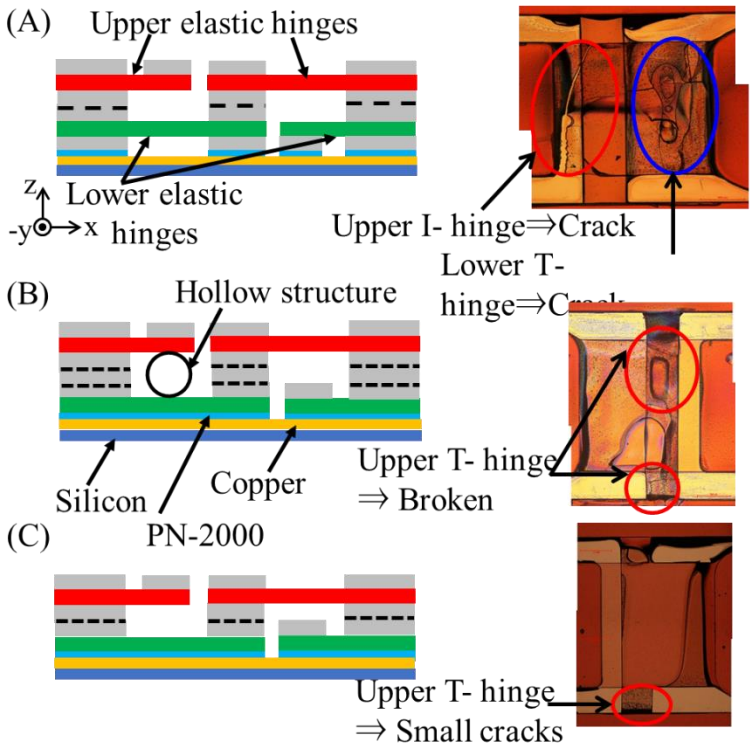

Figure 2.7: Fabrication result of two-wing type transmission with its cross-section to show the position of the elastic hinge and hollow structure, a large hollow structure (A) medium hollow structure (B) small hollow structure (C). Note hollow structure is defined as the gap between layers

Table 2.1: Summary of the fabrication of two-wing type transmission and cause of the cracks

Condition	Lower hinge crack	Upper hinge crack	Cause of crack
A	Yes	Yes	Large hollow structure
B	No	Yes	Less hollow structure
C	No	Very small	Small hollow structure

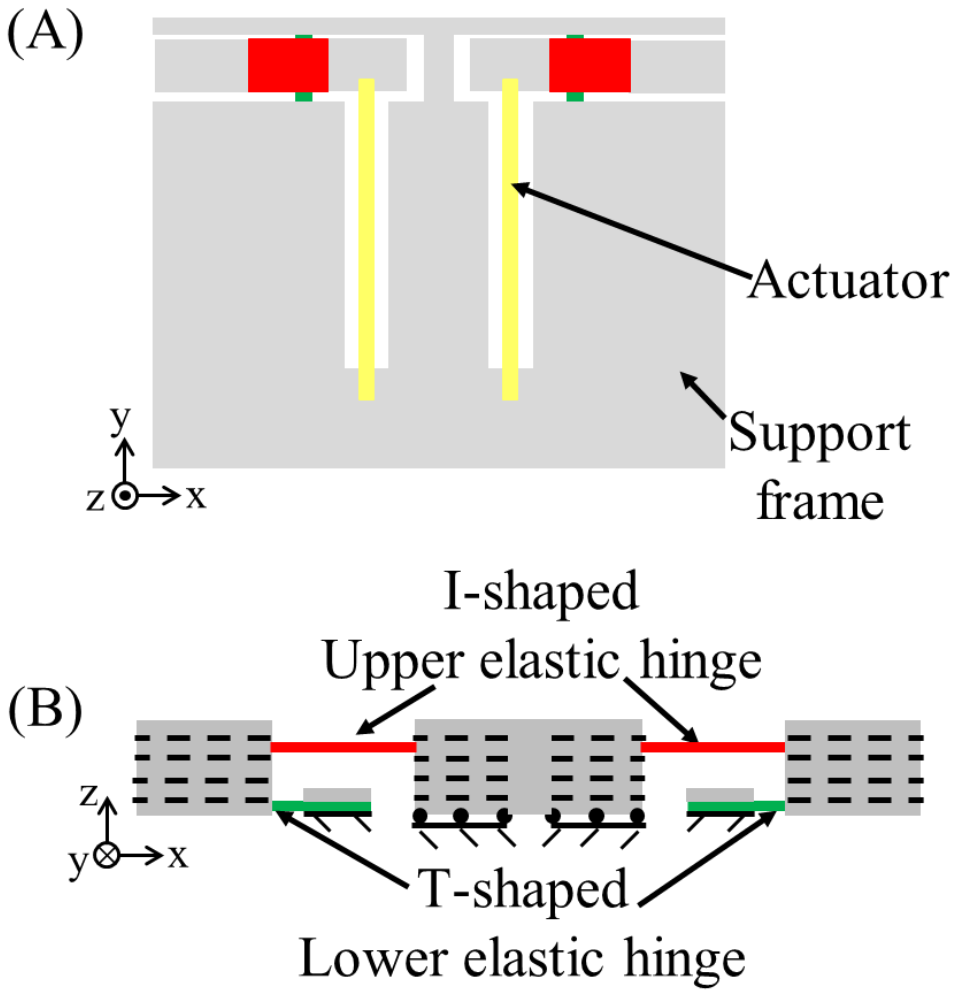

Figure 2.8: Proposed 2.5-dimensional one wing type transmission in plain view (A) cross-sectional view (B)

2.2 2.5-Dimensional transmission for small translational to large rotational motion conversion

2.2.1 Conceptual design of the polymer micromachined flapping-wing nano air vehicle

The polymer micromachined FWNAV proposed here consists of a micro transmission, a supporting frame, a piezoelectric bimorph actuator, and wings, as shown in Fig. 2.9; these are the main components of FWNAVs [119]. The feature that sets the proposed FWNAV apart from previous designs is that it has a complete 2.5-dimensional structure that can be fabricated using standard microfabrication techniques [56].

The production of a large stroke angle of the wing during the flapping motion is the main consideration in the design and fabrication of FWNAVs. The other fundamental motion of the wing required to produce the lift force is the feathering motion, which can be evaluated by the FSI [55, 57, 58, 132–135]. The FSI design of the FWNAV wing reduces the electromechanical complexity [55].

2.2.2 Basic mechanism of the transmission

The proposed transmission is based on a geometrically nonlinear bending deformation [56]. Fig. 2.10 shows the transmission mechanism using the nonlinear bending of the cantilever plate. According to geometrically nonlinear bending deformation theory, a small translational displacement u_x along the longitudinal axis of the cantilever plate produces a large deflection angle φ at the tip of the cantilever plate. Unlike in previous studies [51–53], small inputs can be directly transmitted as large outputs using this mechanism. The ratio of the rotational output φ to the translational input u_x is called the transmission ratio [20].

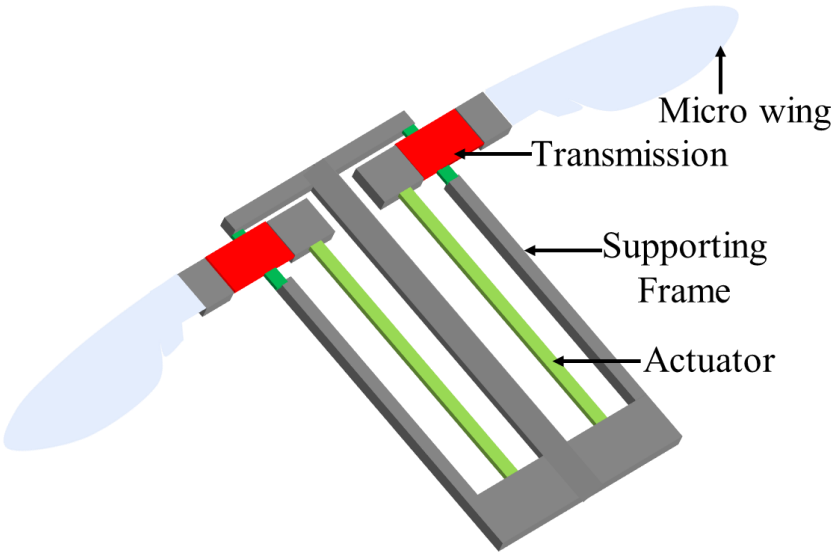

Figure 2.9: Conceptual view of the proposed polymer micromachined insect-inspired FWNAV. It consists of a transmission, a supporting frame, a piezoelectric bimorph actuator, and a micro wing

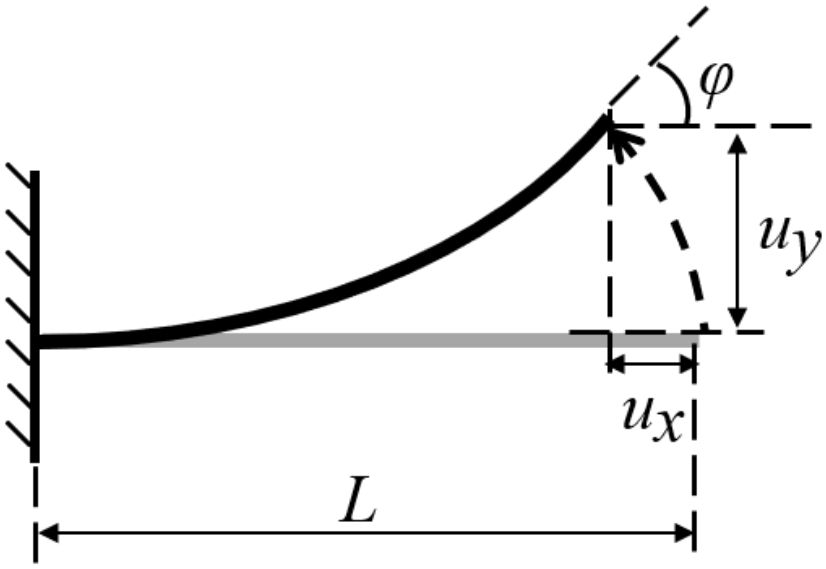

Figure 2.10: Geometric nonlinear bending of the cantilever plate for the transmission mechanism

2.3 Transmission design and analysis

2.3.1 Basic transmission design

Fig. 2.11 shows the basic design of the transmission using the mechanism presented in the previous section. As shown in this figure, the transmission

consists of (1) a parallel elastic hinge, (2) a hinge-supporting beam, (3) a wing attachment part, and (4) an actuator attachment part. Fig. 2.12(A) shows the *xz* plane view of the transmission with the detailed dimensions which is decided based on the rigorous parametric study of the dimension using static structural analysis. Fig. 2.12(B) shows the same view in the case where a small translational displacement u_x given by the actuator at point P causes the bending of the elastic hinges along with the large rotation φ of the wing attachment part based on the mechanism discussed in the previous section. The gap between the parallel elastic hinges in Fig. 2.12(A) is determined by the number of polymer sheets because of the proposed fabrication method using polymer micromachining [9]. Four or more polymer sheets should be used because of fabrication restrictions, to avoid the sticking of hinges [9]. Hence, we set the gap length in the design to 160 μm, which is equal to the thickness of four polymer sheets.

Furthermore, as the gap length decreases, the transmission ratio is almost constant, as shown in Table 2.2; this is demonstrated by finite element analysis as discussed in the next sub-section.

2.3.2 Static structural analysis of the transmission with the supporting frame using the nonlinear finite element method

This section presents the static analysis of the transmission with the supporting frame using the nonlinear finite element method [149]. Fig. 2.13 shows the problem setup for the geometrically nonlinear static analysis of the transmission. A forced displacement u_x was applied to the transmission at the area where the free end of the piezoelectric bimorph actuator is attached (the actuator attachment part in Fig. 2.13), and the fixed boundary condition was applied to the supporting frame where the fixed end of the piezoelectric bimorph actuator is attached.

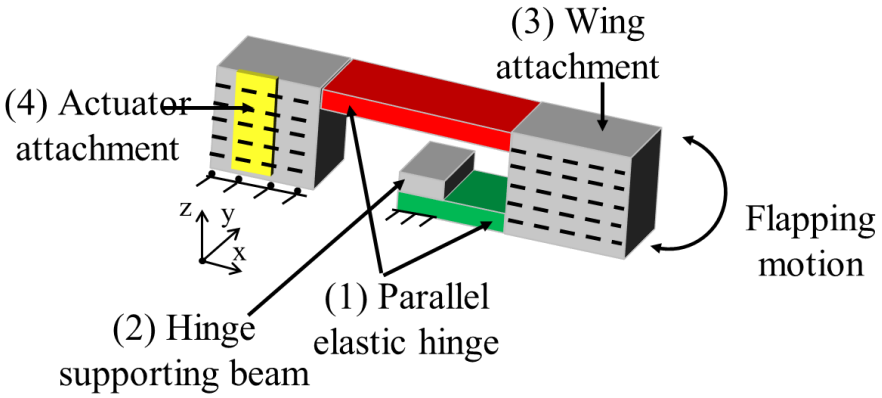

Figure 2.11: Basic design of the transmission in 3-D view

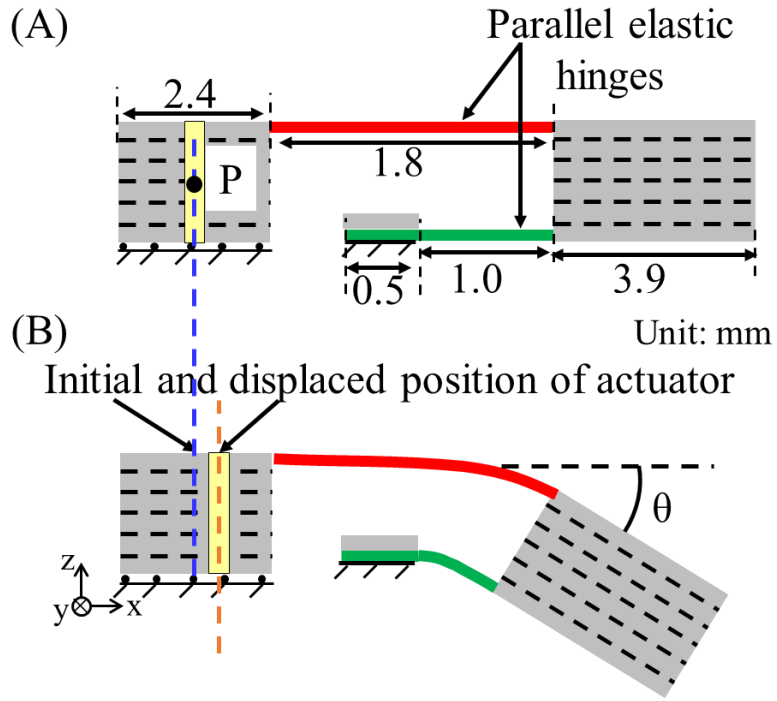

Figure 2.12: *xz* plane views of (A) the reference transmission with dimensions (initially undeformed) and (B) the deformed transmission

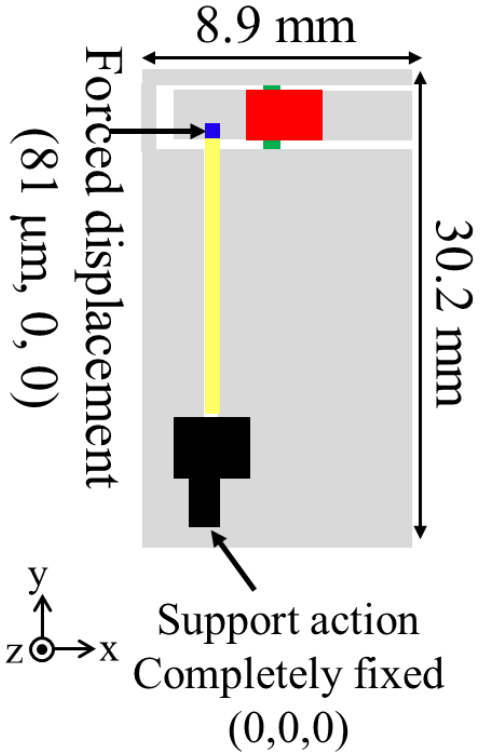

Figure 2.13: Problem setup: load and boundary conditions for the finite element analysis of the transmission

The forced displacement u_x was set to 81 μm, which is the point of equilibrium between the reaction forces of the transmission and the actuator, as shown in Fig. 2.14. The transmission reaction force as a function of u_x was obtained by geometrically nonlinear finite element analysis using the Marc software solver.

The finite elements used here are 20-node solid hexahedral elements as shown in Fig. 2.15 which shows the mesh division of the transmission in plain view. The total no. of elements in the mesh is 14632 whereas the total no. of nodes in the mesh is 75016.

The maximum reaction force for $u_x = 0$ and the maximum u_x when no mechanical load is applied by the piezoelectric bimorph actuator in Fig. 2.16 can be obtained theoretically using the following equations [150]:

$$F = \frac{3E_p w\delta}{2L^3}\left[\frac{t_p^3}{3} + t_p\left(t_m + t_p\right)^2 + \frac{E_m t_m^3}{6E_p}\right], \tag{2.1}$$

$$\delta = \frac{6E_p d_{31} V(t_m + t_p)L^2}{2E_p\left(3t_m^2 t_p + 6t_m t_p^2 + 4t_p^3\right) + E_m t_m^3}, \tag{2.2}$$

where $d_{31} = 1.98 \times 10^{-10}$ m/V is the piezoelectric constant, $L = 20$ mm is the length of the actuator, $E_p = 61$ GPa is the Young's modulus of the piezoelectric material, $E_m = 140$ GPa is the Young's modulus of the metal shim, $t_p = 0.2$ mm is the thickness of the piezoelectric material, $t_m = 0.1$ mm is the thickness of the metal shim, $w = 3$ mm is the width of the actuator, and $V = 200$ V is the applied voltage.

It should be noted that to maximize the translational displacement from the biomorph actuator, it should be connected in parallel as shown in Fig. 2.16, because this maximizes the biomorph actuator deflection [151].

Figs. 2.17 and 2.18 show the finite element analysis results. As shown in Fig. 2.17, the stroke angle was approximately 30°, which is comparable with that of an actual insect during flapping motion [70, 78, 152]. Figs. 2.18 shows the von Mises stress distribution during the flapping motion.

The maximum von Mises stress was approximately 19 MPa at the lower elastic hinge, which is approximately 18% of the polyimide (PI) sheet breaking strength of 109 MPa [153]. Therefore, the chance of the transmission breaking or failing during operation will be very low.

Similarly, the effect of elastic hinge gap on flapping performance has been

evaluated, see Table 2.2 which indicates that the effect is trivial.

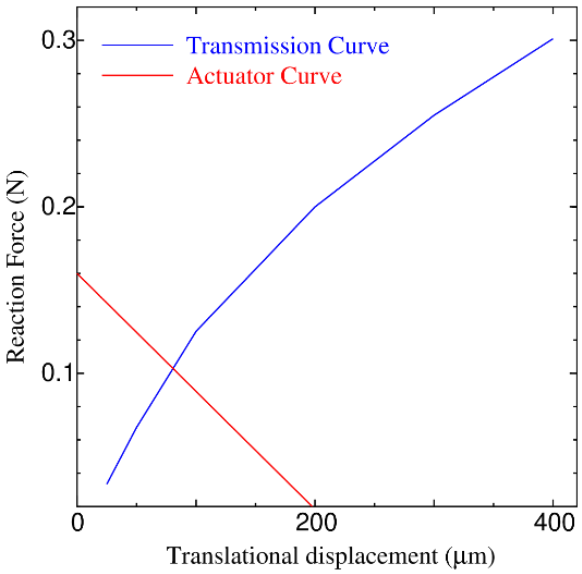

Figure 2.14: Reaction force plotted against the forced displacement. The blue line shows the results for the transmission, which were obtained using the geometrically nonlinear finite element analysis. The red line shows the results for the actuator, which were obtained using the theoretical formula

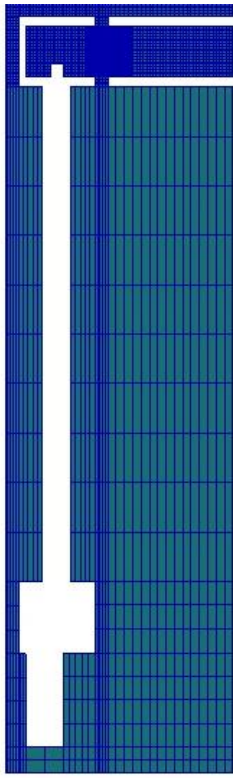

Figure 2.15: Mesh division of the transmission for static analysis

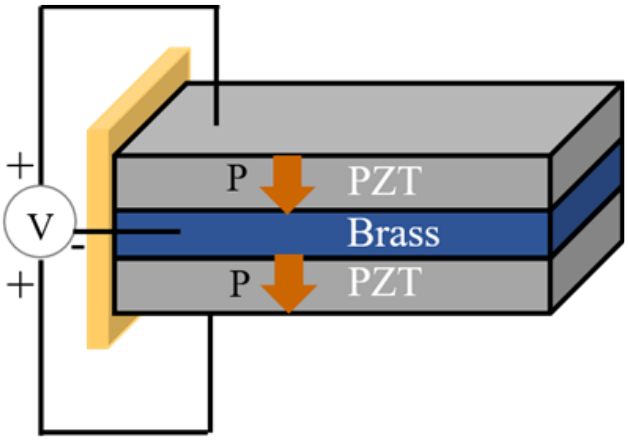

Figure 2.16: Actuator problem setup for polarization

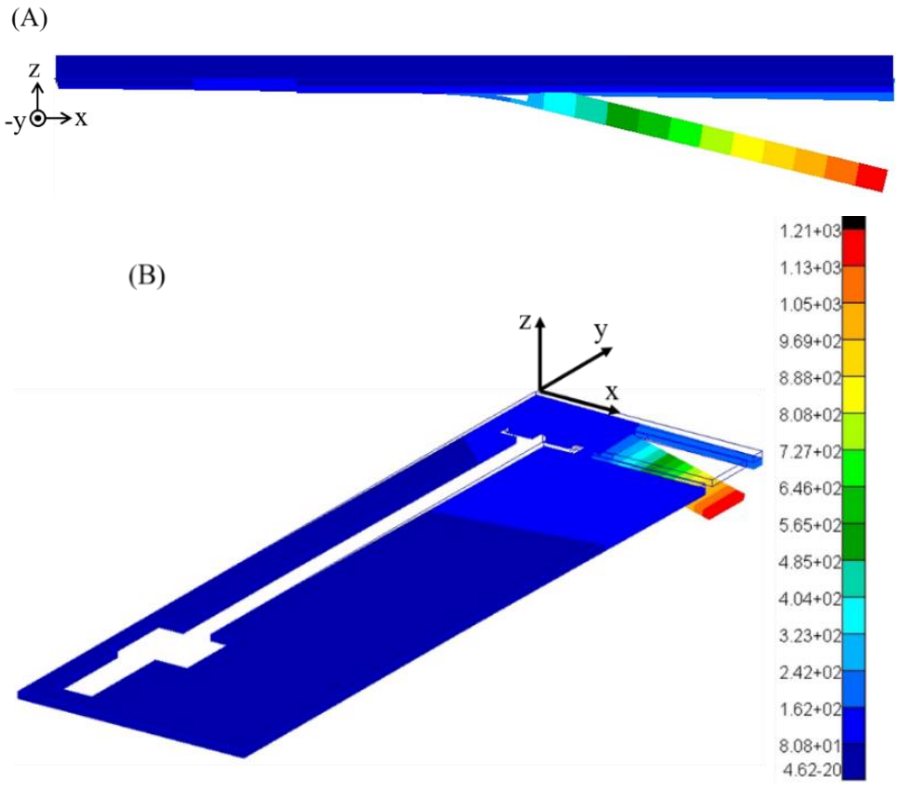

Figure 2.17: Geometrically nonlinear finite element analysis of the transmission and the supporting frame. The color indicates the magnitude of the actual displacement deformation with a unit of μm. (A) *xz* plane view and (B) 3D view. Here, the flapping motion is downward, or the deflection of the hinge is negative in the *z*-direction

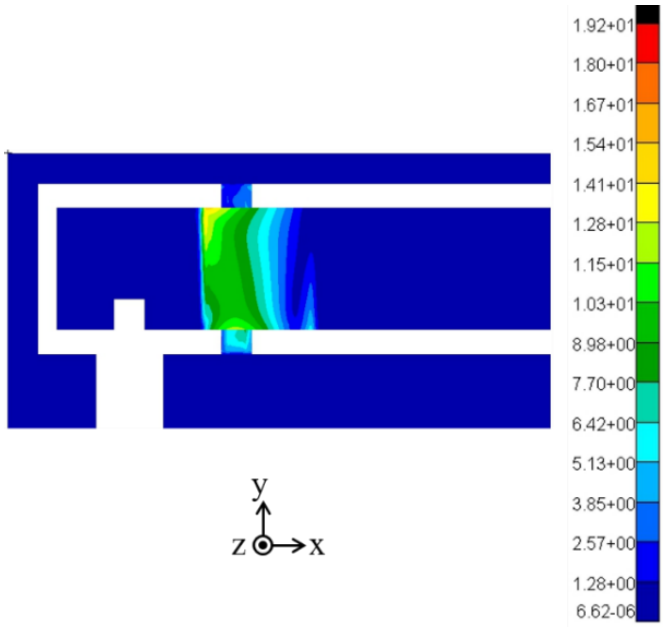

Figure 2.18: Detailed view of Mises stress distribution in the transmission and the frame. The color shows the magnitude of the Mises stress in MPa

Table 2.2: Variation of characteristic quantities with the number of polymer sheets used to set the gap between the two elastic hinges, with the translational displacement u_x fixed at 81 μm

Number of polymer sheets for the gap between two elastic hinges	Stoke angle (°)	von Misses stress (MPa)
2	26.74	18.7
3	27.38	19.2
4	27.17	19.2

2.4 Conclusion

A one wing transmission, whose functionality is based on geometrically nonlinear bending, was proposed in this study, and its design allows further miniaturization for use in FWNAVs. The novelty of this research is (1) the introduction of an elastic hinge in the design; (2) a transmission mechanism based on geometrically nonlinear bending deformation, in which a small translational displacement produces large rotational displacement; and (3) the ability to fabricate the complete 2.5-dimensional structure using standard microfabrication techniques including etching, photolithography, deposition, and curing without

any post-assembly. The proposed transmission will increase the fabrication stability during polymer micromachining because of the absence of a hollow structure for sensitive layers.

The stroke angle of the proposed transmission is approximately 30° without any assistance from the resonance and the mass inertial effect. This stroke angle is comparable with that of actual insects during flapping flight. In this design, the maximum von Mises stress during the flapping motion was only 18% of the breaking strength of the PI sheet. Therefore, there is little chance of failure during transmission operation.

It follows from these results that the proposed transmission can enable the further miniaturization of FWNAVs because no post-assembly is required.

CHAPTER 3

ITERATIVE DESIGN WINDOW SEARCH FOR POLYMER MICROMACHINED FLAPPING-WING NANO AIR VEHICLE

3.1 Introduction

In Chapter 1, we have studied the importance of flapping wing nano air vehicles (FWNAV), and we know that the various groups have developed FWNAVs [17, 20, 29, 94–103]. However, these FWNAVs are based on complicated transmission mechanisms [94–99], and some of them have complexities in the fabrication [17, 20, 29, 100–103]. Hence, their further miniaturization will be difficult. Much effort in these researches is paid to the reduction of their size and weight [117], similar to the evolution of insect flapping flight. Still, it can't be miniaturized because of various challenges during their development

We know that various challenges have been given to the FWNAVs development such as feasibility in terms of a fatigue life due to random cyclic stress, interaction with the fluid, sufficient lift, and drag forces to hover, and thrust forces for the forward flight. These challenges can be overcome by finding out a design solution that sufficiently satisfies all the design requirements (DRs) of the design window (DW) search using computational methods and fabrication using micro-electro-mechanical system (MEMS) technology. The DW is defined as an existing area of satisfactory solutions in the design parameters space [154–157]. The same phenomenon has been implemented in this thesis to develop insect-inspired FWNAV and its further miniaturization.

In order to develop FWNAV which can be easily miniaturized, I have proposed polymer micromachined transmission which has a 2.5-dimensional (2.5-D) structure in Chapter 2 [9, 62] and it has produced a large stroke angle of about 40° transmitted from the small amplitude of the piezoelectric bimorph actuator using the large deformation of the elastic hinges without any inertial effect. Hence, it will contribute to the further miniaturization of FWNAVs.

Fig. 3.1 shows the concept of the proposed polymer micromachined FWNAV based on one-wing transmission. This FWNAV consists of a pair of micro wings with the 2.5-D structure, a micro actuator of the piezoelectric bimorph, and our transmission. These components can be fabricated using the polymer micromachining technique because of their 2.5-D structure.

In this FWNAV, the stroke angle will further increase due to the inertial effects of both the transmission and the wing. The large stroke angle similar to the small flies will lead to the further miniaturized FWNAV or the insect-inspired FWNAV, which is the engineering interpretation of time-tested nature's solutions such as the fluid-structure interaction cause of characteristic motions of insect's wings [55, 57–59, 127, 130]. However, the dynamic large deformation causes stress issues such as the fatigue failure of materials. The restrictions related to these issues conflict with other design requirements (DRs) such as the DR for the large stroke angle.

In general, the conceptual, basic, and detailed design processes of the insect-inspired FWNAVs are indistinguishable from each other, and the formulation as a single design problem is difficult in each design process [46]. Hence, an iterative design method for changes to the design problem will be effective for the development of the insect-inspired FWNAVs. However, as long as I know, there is no study focusing on this topic.

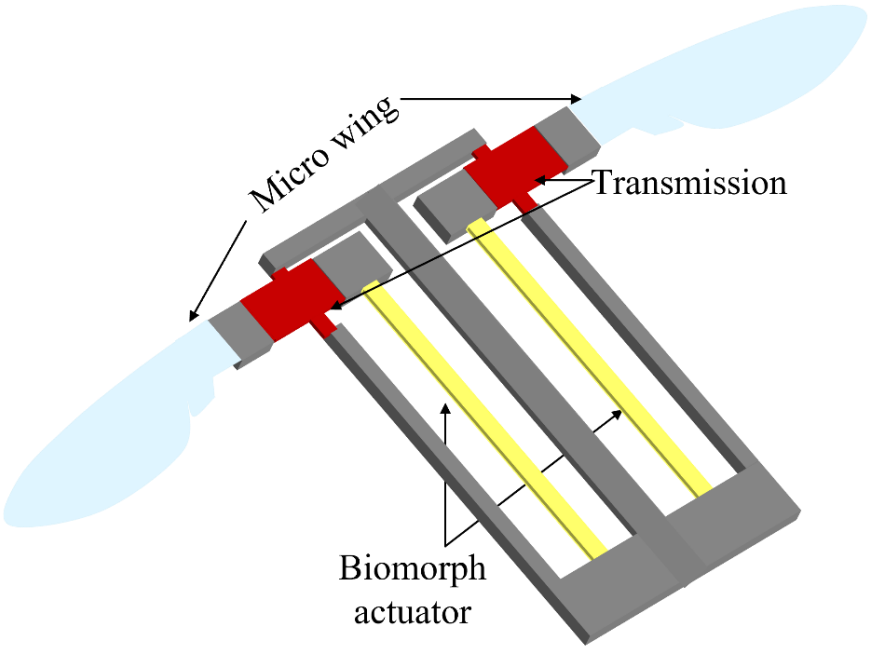

Figure 3.1: Conceptual view of the polymer micromachined FWNAV

In this chapter, I have proposed an iterative design window (DW) search method for the design of the insect-inspired FWNAVs. The DW is defined as an existing area of satisfactory solutions in a design parameter space [154]. Hence, this method is adaptive for the design problem changes. Along with the context of the iterative algorithm, the proposed method searches the DW iteratively following the change of the design problem. The proposed DW search using the nonlinear dynamic analysis is applied for firstly the transmission without the micro wing, and secondly the transmission with the micro wing. I find the DWs that satisfies the nonlinear and unsteady DRs conflicting with each other simultaneously. In future work, I will fabricate the FWNAV based on the proposed DWs using polymer micromachining [9].

In the next section, the proposed DW search methodology has been discussed and in the later subsequent sections, the application of the proposed DW search method for the design of the transmission, micro wing, and FWNAV has been discussed.

3.2 Design methodology and design problem

3.2.1 Iterative design window search approach

In order to design the flyable FWNAV, I have adopted an individual research flow as shown in Fig. 3.2. The micro transmission has been designed using this type of research flow in Chapter 2 [9, 62]. This research flow indicates that design should continuously evolve until it is completed. This is because the conceptual, basic, and detailed design processes for the development of the insect-inspired FWNAVs are indistinguishable from each other, and the formulation as a single design problem is difficult in each design process.

Hence, in this study, an iterative design method for changes to the design problem has been proposed. Fig. 3.3 shows the concept of the proposed DW search. As shown in this figure, the DW is searched for the design problem, and following the change of the design problem, the new DW is searched from the previous DW. This process is repeated until no further change is given to the design problem. The numerical analysis method is applied for the design candidate defined by the design parameter set to evaluate the design characteristics. Here, the parametric study is used instead of using a specific search algorithm to change the design parameters.

In the parametric study, the nonlinear dynamic simulation is conducted using nonlinear finite element transient analysis of MARC solver with 20-node solid hexahedral elements, where the following transient finite element discrete equation considering the geometrical nonlinearity is solved [149]:

$$\mathbf{Ma} + \mathbf{Cv} + \mathbf{Q(u)} = \mathbf{F}, \qquad (3.1)$$

where **M** and **C** are the mass and diffusive matrices, respectively; **Q** is the interior force vector; **a**, **v**, and **u** are the acceleration, velocity, and displacement vectors, respectively; **F** is the external force vector.

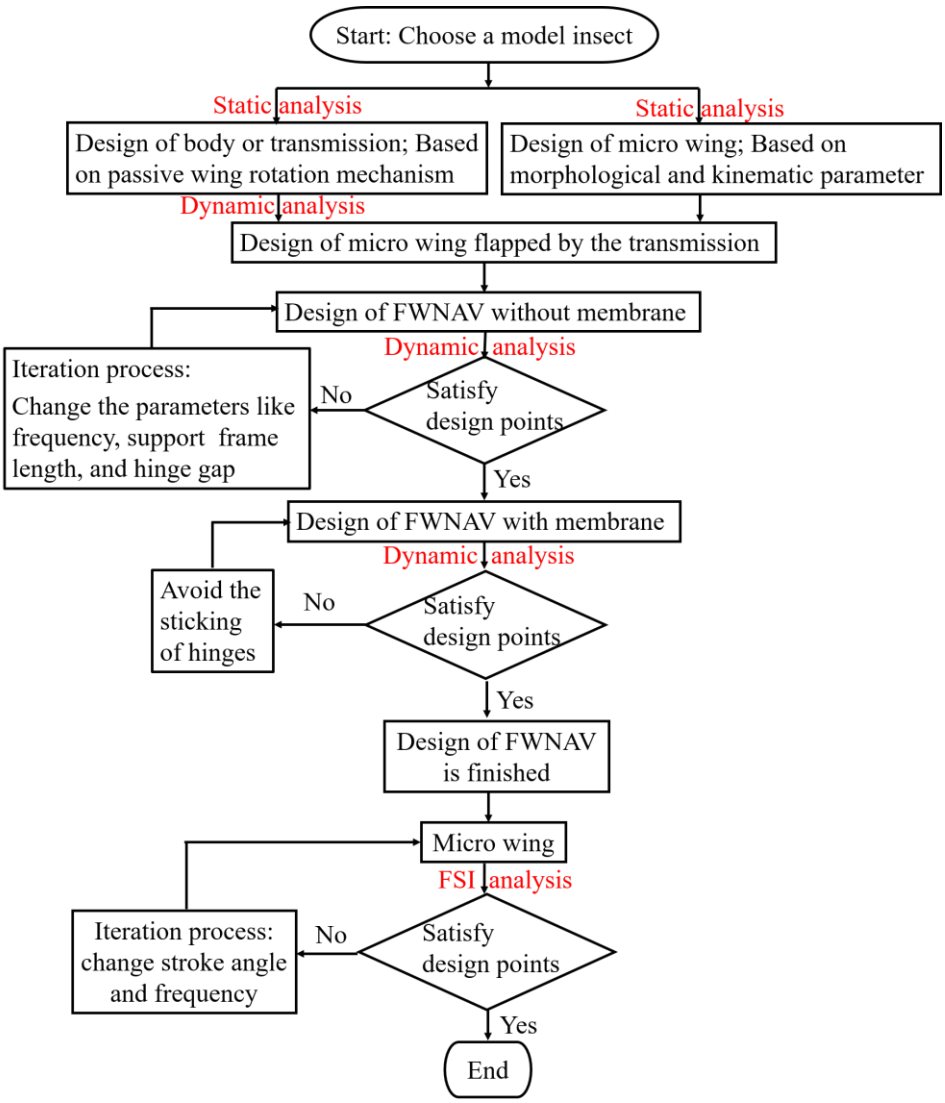

Figure 3.2: Individual research flow to design the flyable polymer micromachined FWNAV. Note structural analysis is used for design and FSI analysis is used to evaluate the flight performance of FWNAV

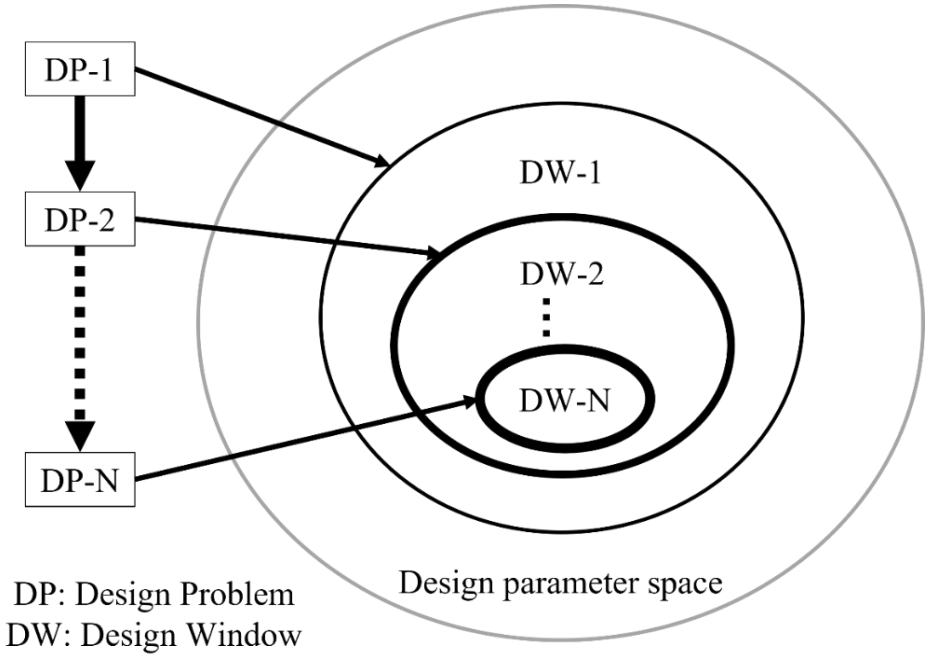

Figure 3.3: An iterative design window search methodology

3.2.2 Design requirements and parameters of the polymer micromachined flapping-wing nano air vehicle

Figs. 3.4(A) and (B) show the basic design of the FWNAV in the plain and cross-sectional views, respectively. As shown in these figures, the FWNAV has a 2.5-D structure, and it consists of the micro transmission, the supporting frame, the bimorph actuator, and the micro wing (flexible wing membrane supported by the rigid leading-edge beam). Table 3.1 describes the material properties of polyimide (PI). The material property distribution in the FWNAV is shown in Fig. 3.5.

In the research flow diagram, the design points refer to the design requirements (DRs), or all necessary DRs for this study are listed as follows:

(A) Strength of the material.

(B) Production of enough stroke angle similar to small flies.

(C) Production of enough flapping velocity to support the weight of FWNAV.

(D) No sticking between elastic hinges to avoid their damage.

(E) Fabricability

(F) Fatigue failure of the material.

In order to design the FWNAV, firstly, the micro transmission was designed, secondary, the micro wing was designed, and, finally, the FWNAV was designed

such that it satisfied all the DRs. Since the present problem has been formulated and solved using nonlinear dynamic analysis, the design parameter space should include the mechanical parameters like mass and frequency as well as the geometrical parameters. That is, all the design parameters used in this study are following,

- The flapping frequency f
- The mass density ratio r
- The leading-edge width w_{LE}, t_{LE}, and its extended L_e,
- the length of the support frame L_s
- The elastic hinge gap h.

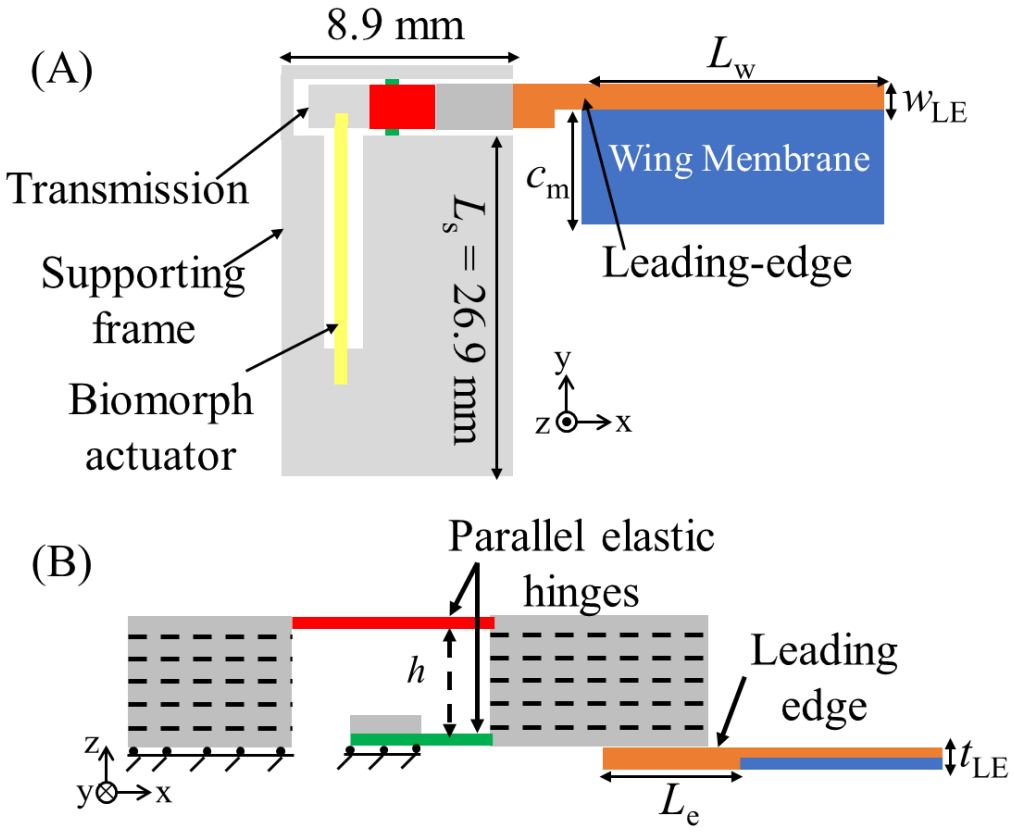

Figure 3.4: Actual design (design problems for this study) of polymer micromachined FWNAV in plain view (A), and cross-sectional view (B). Note L_w and c_m are the spanwise and chordwise lengths of the micro wing, respectively

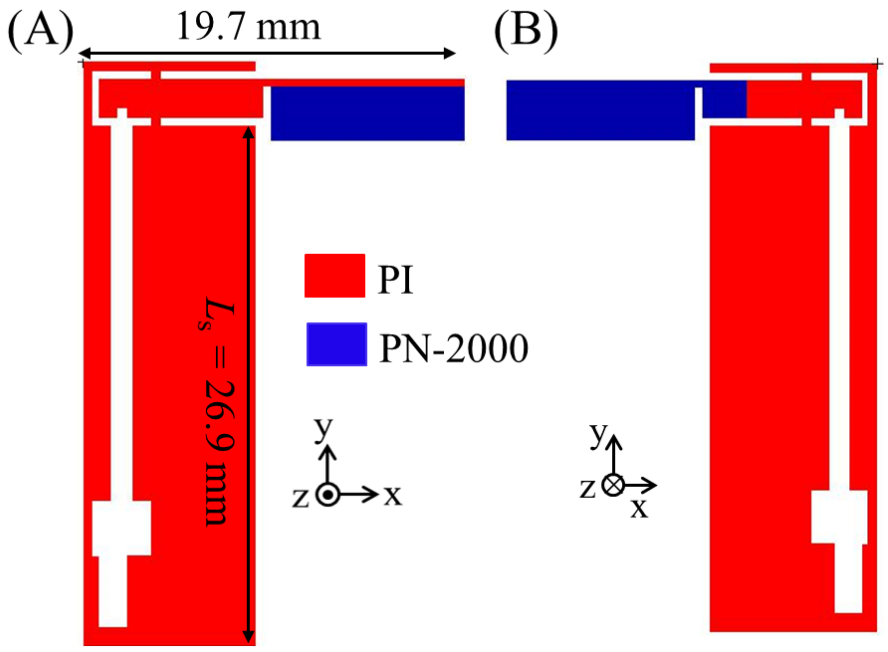

Figure 3.5: Material property distribution in the polymer micromachined FWNAV

Table 3.1: Properties of polyimide (PI) material

Material	Young's modulus	Mass density	Poisson's ratio	Breaking strength
PI*	2.5 GPa	1420 kg/m^3	0.289	109 MPa
PN-2000**	3.5 GPa	1420 kg/m^3	0.30	109 MPa

* Photosensitive polyimide adhesive sheet,** Photosensitive polyimide solution [153]

3.2.3 Summary of the design process

In this sub-section, the design process using the proposed method in the following sections has been summarized as follows:

In the first process, the micro transmission was designed, where transmission designed using the nonlinear static analysis in Chapter 2 [9, 62] was taken as the initial solution. In this process, initially, a DW was searched for the flapping frequency *f* to satisfy the DRs (A) and (D), and then, using this DW search result, a new DW was searched for a mass of micro wings flapped by this transmission,

which was simulated using the mass density ratio r, to satisfy the DRs (A) and (B). Note that the mass density ratio is defined as $r = \rho'/\rho$, where ρ and ρ' are the original and increased mass densities of the wing attachment, respectively.

In the second process, the micro wing was designed. Using the previous DW search result along with morphological parameters of dipteran insects, a new DW was searched for the dimensions w_{LE}, t_{LE}, and L_e of the micro wing to satisfy the DRs (A) and (E).

In the final process, the FWNAV was designed, where the design solutions of the micro transmission and the micro wing from the previous DW search were used. In this process, initially, a DW was searched for f to satisfy the DRs (A) and (B), and then, using this DW search result, a new DW was searched for the length of support frame L_s to satisfy the DRs (A), (B), and (C). Finally, this DW search result was examined for safely working of the FWNAV. That is, the elastic hinge gap during the dynamic response was examined to satisfy the DR (D).

After the complete design of FWNAV, its fatigue life i.e. DR (F) is estimated for an individual load and boundary condition. In this way, a design solution for FWNAV is finally obtained that fulfills all the DRs.

The summary of the DW search process along with the DRs has been shown in Fig. 3.6.

3.3 Design window search for the micro transmission with the inertial effect

I consider here the micro transmission designed using the nonlinear static analysis in Chapter 2 [9, 62] as the base. The dynamic performance is newly designed here by studying the flapping frequency f and the mass density ratio r of the wing's attachment part. Note that r expresses the concentrated wing's mass at the wing's attachment part instead of its direct modeling for the purpose of reducing the computational cost. Hence, in this section, we consider the design parameter space (f, r), while the other design parameters are fixed as follows: L_s and h are set as 26.9 mm and 160 μm, respectively, following Chapter 2 or Refs. [9, 62]. w_{LE}, t_{LE}, and L_e are set as 0 because of no wing.

(A)

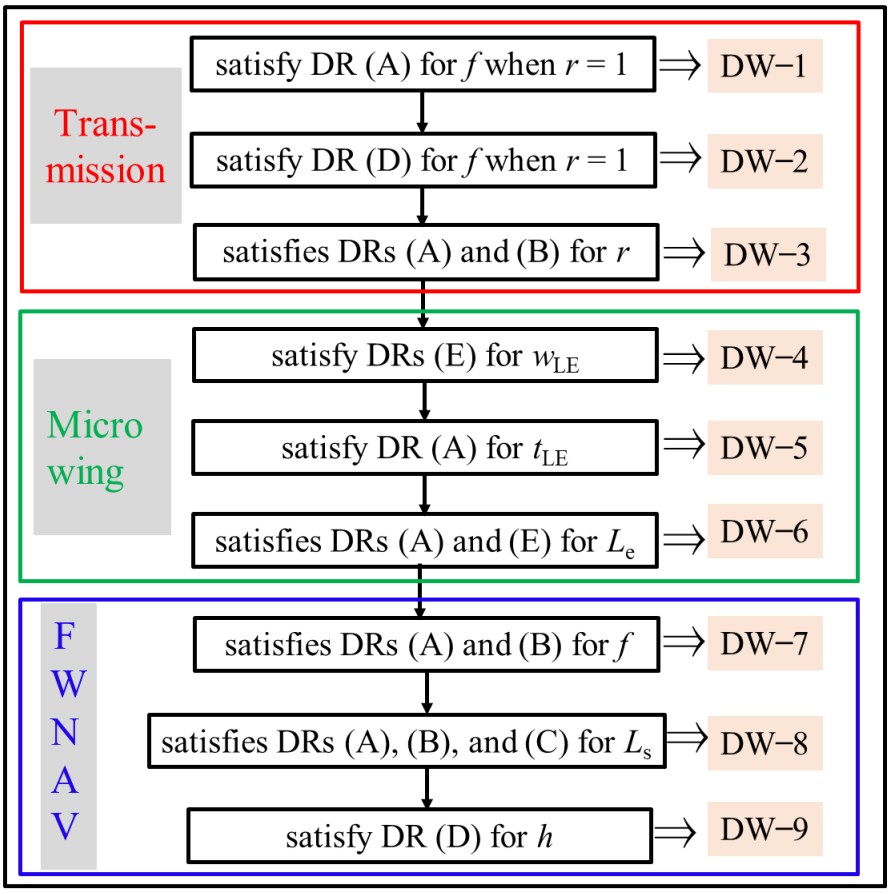

(B)

Design Requirements (DRs):

(A) Strength of the material
(B) Enough Stroke angle
(C) Enough flapping velocity
(D) No sticking between elastic hinges
(E) Fabricability
(F) Fatigue life of the material

Design parameters:

① Flapping frequency f
② Mass density ratio r
③ Leading-edge cross-section ($t_{LE} \times w_{LE}$) and its extended length L
④ Length of support frame L_s
⑤ Elastic hinge gap h

Figure 3.6: DW search process summary (A) design problems (B)

3.3.1 Design window search for the transmission

Fig. 3.7 shows the basic problem setup of the transmission without the wing. The harmonic forced displacement $u_x = U_x \times \sin 2\pi ft$ (U_x is the vibration amplitude, and f is the flapping frequency, which is the design parameter) is applied to the area of the transmission, where the tip of the actuator is attached. The evaluation of U_x is discussed in Chapter 2 [9]. The fixed boundary condition is applied to the area of the supporting frame, where the fixed end of the actuator is attached. For this setup, the finite element mesh with 19,582 elements and 98,451 nodes. The time increment is $\Delta t = T/500$, and T is the flapping period and is equal to the inverse of f.

First, the DW for the design problem of the DR (A) in the design parameter space (f, r) (DW-1) is searched using the parametric study on f, where r is set as 1 (no wing). The DR (A) is formulated as

$$\sigma_{\mathrm{M}} < 50\% \text{ of the breaking stress}, \tag{3.2}$$

where σ_{m} is defined as the maximum Misses stress in space, and its maximum in time is σ_{M} i.e., σ_{M} is the maximum Misses stress in the transmission in space and time. Here, Eq.(3.2) is reduced to $\sigma_{\mathrm{M}} < 54.5$ MPa based on Table 3.1. U_x is set as 81μm based on the force balance between transmission and actuator discussed in Chapter 2 [9] and f is varied from 50 Hz to 250 Hz with an interval of 25 Hz. Note that this value of U_x is used throughout this study. The design characteristics: stroke angle Φ and σ_{M} are evaluated from the dynamic simulation.

The results are plotted for f as shown in Fig. 3.8. From this figure, the DW is determined as follows: The lower limit for f is given as 100Hz, which is based on that in actual small flies, whereas the upper limit for f is given as 190 Hz approximately because of the DR (A) as $\sigma_{\mathrm{M}} < 50$ MPa. Hence, DW-1 is given as

$$\text{DW-1} = \{(f, r) \mid 100 \text{ Hz} \leq f \leq 190 \text{ Hz}, r = 1\}. \tag{3.3}$$

Φ decreases monotonically as f decreases, and it converges to 30° approximately. This means that the inertial effect for $f \sim 50$ Hz is ignorable. This stroke angle is smaller than that given from the quasi-static test in Chapter 2 [9]. This is because the actual deformation of the supporting frame is exactly taken into account in this study. Hence, the increase of Φ larger than 30° is given by the

inertial effect. For the purpose of better understanding, the inertial effect has been discussed in detail at the end of this section.

Next, the DW for the DR (D) (DW-2) is searched. The sticking of the hinges in Fig. 3.9 is evaluated for f = 100, 125, and 150 Hz. As shown in Fig. 3.9, sections A and B belong to the upper and lower hinges, respectively, and they have the same in-plane position. The sticking of the hinges evaluated for f = 100, 125, and 150 Hz are summarized in Table 3.2. This table shows the maximum out-of-plane positions at sections A and B of the transmission and the gap between these sections during the upward flapping motion. As shown in Table 3.2, the gaps for f = 100 and 125 Hz are positive, and the DR (D) is satisfied for the current initial gap of 160 μm.

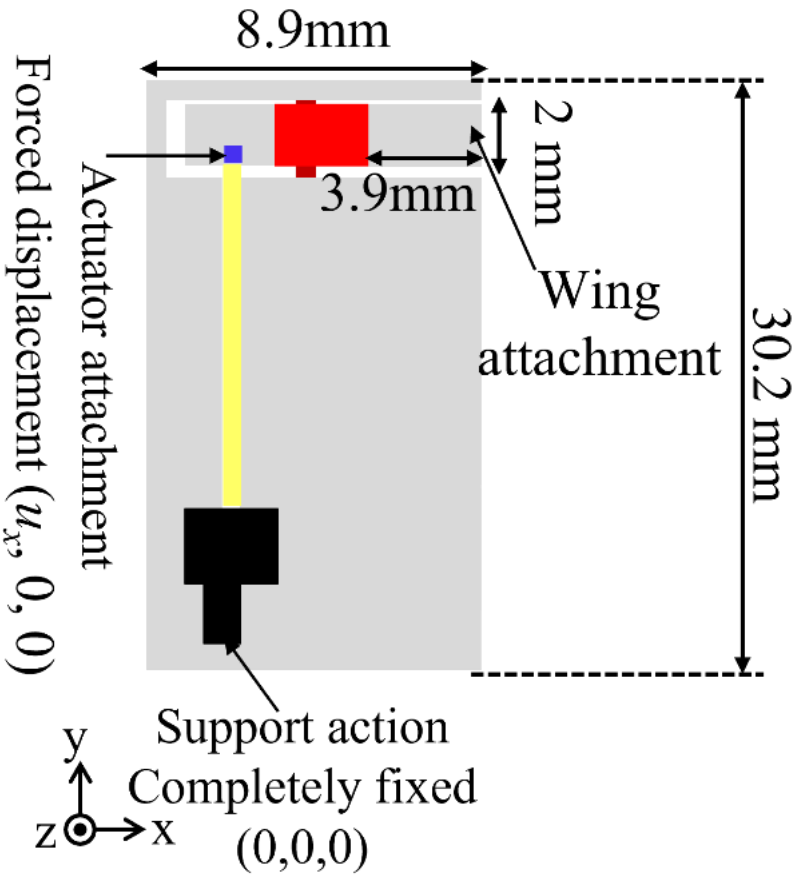

Figure 3.7: Problem setup for the nonlinear dynamic simulation of micro transmission

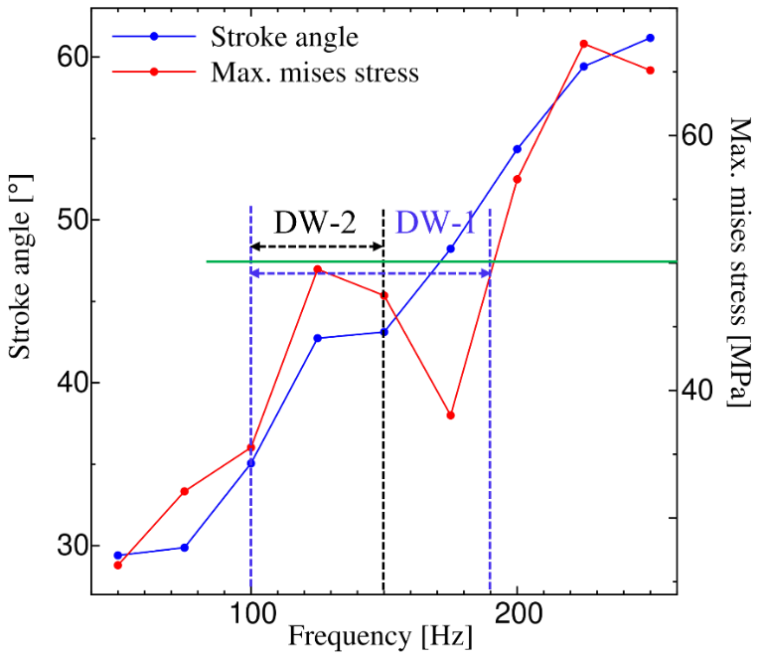

Figure 3.8: DW search results using the parametric study on f for micro transmission. The design problem consists of the DR (A), and the design parameter space is (f, r), where r is set as 1. The horizontal green line denotes the DR (A) given by Eq.(3.2)

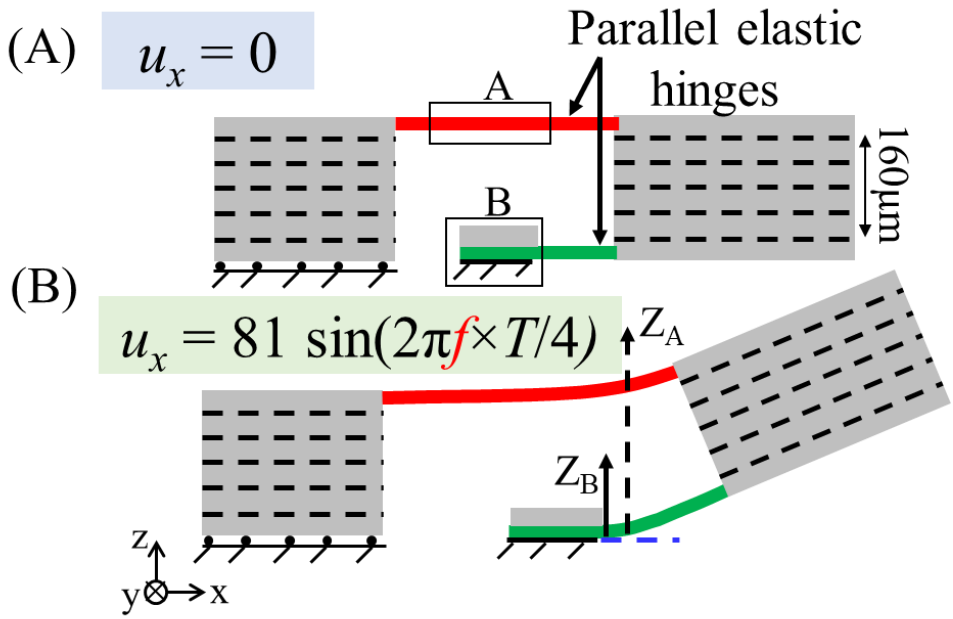

Figure 3.9: A sectional view of the transmission in undeformed condition (A) and deformed condition (B). Z_A and Z_B denote the out-of-plane positions of sections A and B, respectively

Table 3.2: Out-of-plane positions of sections A and B, and their gap

f (Hz)	Z_A	Z_B	Z_A - Z_B	*Sticking*
100 Hz	206.47 μm	187.77 μm	18.70 μm	No
125 Hz	238.07 μm	212.65 μm	25.42 μm	No
150 Hz	244.25 μm	271.10 μm	-26.85 μm	Yes

On the contrary, the gap for f = 150 Hz is negative, and the DR (D) is not satisfied for the current initial gap of 160 μm. Note that this violation can be avoided by increasing the gap [9]. However, the idea of increasing the hinge gap is not used in the early stage of the DW search rather than it is used in the final DW search as discussed in Section 3.5.3. As shown in Fig. 3.8, σ_m suddenly drops at f = 150 Hz as f increases. This might be caused by the sticking. Hence, DW-2 is given as

$$\text{DW-2} = \{(f, r) \mid 100 \text{ Hz} \leq f < 150 \text{ Hz}, r = 1\}. \quad (3.4)$$

The deformation of the transmission during the upward flapping motion and the von Mises stress distribution for f = 125 Hz are shown in Figs. 3.10 and 3.11 to understand the flapping motion. In Fig. 3.11, σ_m occurs in the lower elastic hinge. The correlation between deformation and Mises stress is discussed using the time histories of the flapping angular displacement φ and σ_m for f = 125 Hz, which are shown in Figs. 3.12(A) and (B), respectively. As shown in Fig. 3.12, the clear correlation between these values can be observed at the time instants of about 0.002 sec and 0.006 sec, since the significant peaks of these values occur at these time instants. The extra small peaks in the time history of σ_m, which don't have the corresponding peaks in the time history of φ, occur due to the change of the location where σ_m occurs. This change occurs due to a slight twisting of the wing attachment.

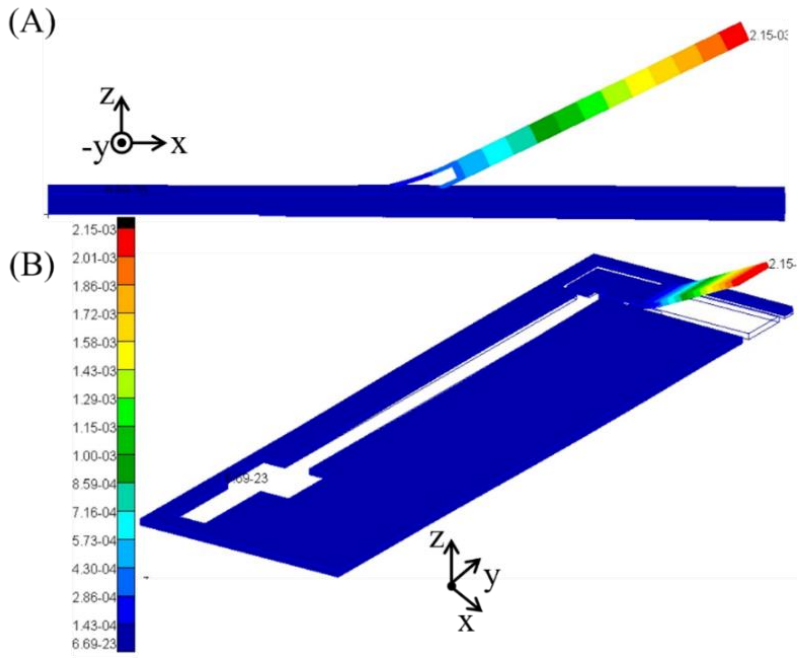

Figure 3.10: Deformation of the transmission during an upward flapping motion for f = 125 Hz. The color contours indicated the magnitude of the actual deformation in unit of m. (A) *xz* plane view. (B) bird's-eye view

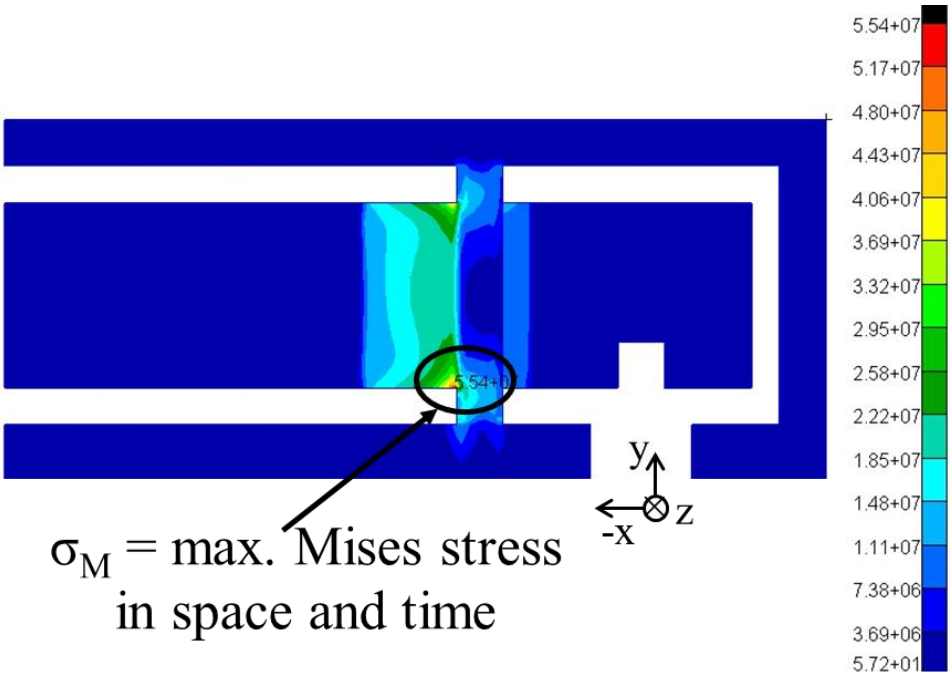

Figure 3.11: Distribution of von Mises stress during the upward flapping motion for f = 125 Hz. The color contour shows the magnitude of von Misses stress in MPa

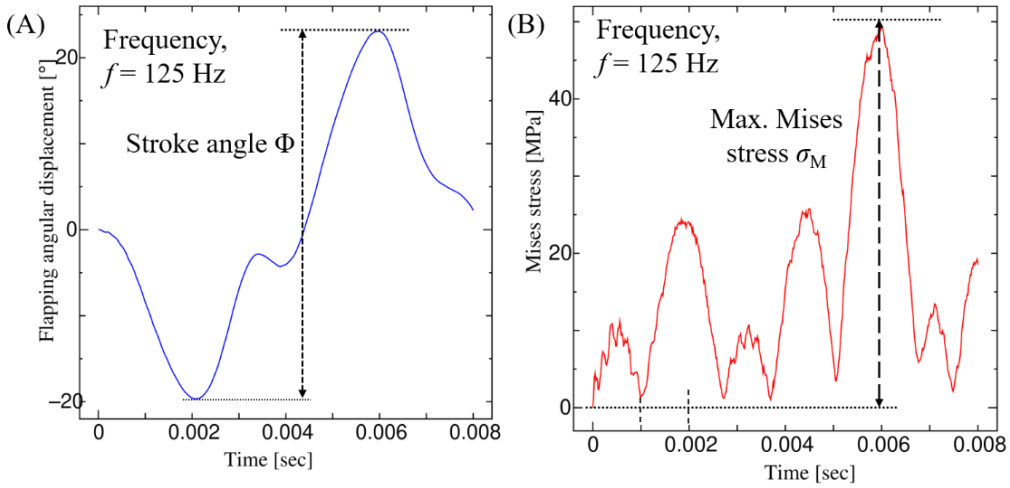

Figure 3.12: Time history of the flapping angular displacement (A) and the von Mises stress (B) for f = 125 Hz

The inertial effect of the transmission on the performance has also been studied for a fixed frequency f = 125 Hz (intermediate frequency of DW-2). For the purpose of evaluating the inertial effect, the mass density of the transmission has decreased from its initial value of 1420 kg/m^3 (PI material) to 0 kg/m^3. As shown in Fig. 3.13, the inertial effect of the transmission on the performance is continuously decreasing as mass density decreases. In the same figure, it can also be observed that the stroke angle without inertial effect (mass density of PI material = 0 kg/m^3) is about 30° while due to inertial effect (mass density of PI material = 1420 kg/m^3) it is about 43° i.e., stroke angle is increased about 1.5 times due to inertial effect.

3.3.2 Mass of the micro wing flapped by the transmission

The DW for the design problem that consists of the DRs (A) and (B) in the design parameter space (f, r) (DW-3) is searched using the parametric study on r, where f is chosen as 100, 125, or 150 Hz from the frequency range of the previous DW-2. The formulation of the DR (A) is already given as Eq.(3.2). The DR (B) can be formulated as

$$\Phi \geq 50°, \tag{3.5}$$

since Φ satisfying Eq.(3.5) and f in the frequency range of DW-2 can produce the mean lift force F_L sufficient to support the weight of small flies [74]. F_L can be estimated based on the quasi-steady evaluation [74] as

$$F_L = 0.5\,\rho^f\,C_L\,S\,U_m^2, \tag{3.6}$$

where ρ^f is the fluid mass density, C_L is the lift coefficient, S is the wing's area, which is defined as $S = L_w\, c_m$, where L_w is the wingspan length, c_m is the mean chord length, and U_m is the mean flapping velocity, which is defined as

$$U_m = 2\, r_2\, \Phi\, L_w f, \tag{3.7}$$

where r_2 is the dimensionless radius of the second moment of the wing area. The morphological parameters $r_2 = 0.54$, L_w = 10–11 mm, and c_m = 3 mm are given from the data of small flies [74], and the kinematical parameters $\rho^f = 1.205$ kg/m^3, $C_L = 2$, $\Phi = 50°$, and $f = 100$ Hz are given. Then, Eqs.(3.6) and (3.7) give F_L = 37 μN, which is larger than the gravity force acting on the weight of small insects m_w g = 30 μN approximately.

The results are plotted for r in Fig. 3.14. From this figure, the DW is determined as follows: r ranges from 2.6 to 3.0 for $f = 100$ Hz, from 1.8 to 2.0 for $f = 125$ Hz, and from 1.2 to 1.6 for $f = 150$ Hz. Hence, DW-3 is given as

$$\begin{aligned} \text{DW-3} = &\{(f, r)\,|\, f = 100 \text{ Hz}, 2.6 \le r < 3.0\}, \\ &\{(f, r)\,|\, f = 125 \text{ Hz}, 1.8 \le r < 2.0\}, \\ \text{or } &\{(f, r)\,|\, f = 150 \text{ Hz}, 1.2 \le r < 1.6\}, \end{aligned} \tag{8}$$

where the mass of the micro wing m_w ranges from 20% to 200% of the wing attachment, of which weight is 2.65 mg in this study. Hence, m_w ranges from 0.53 to 5.3 mg.

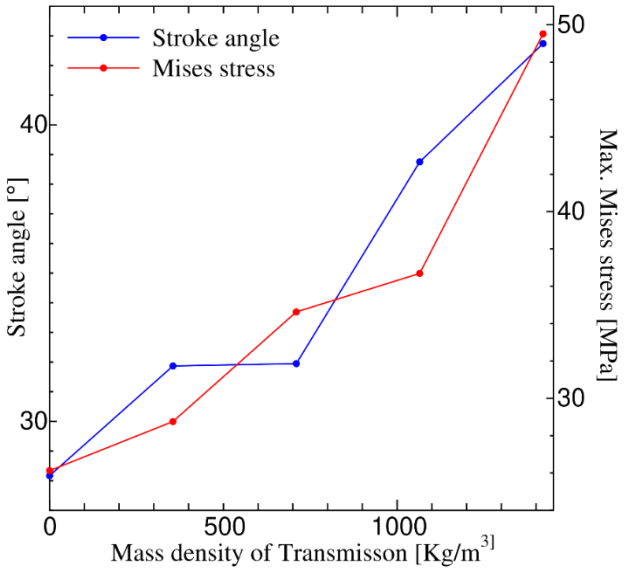

Figure 3.13: Inertial effect on the performance of the transmission for the flapping frequency $f = 125$Hz

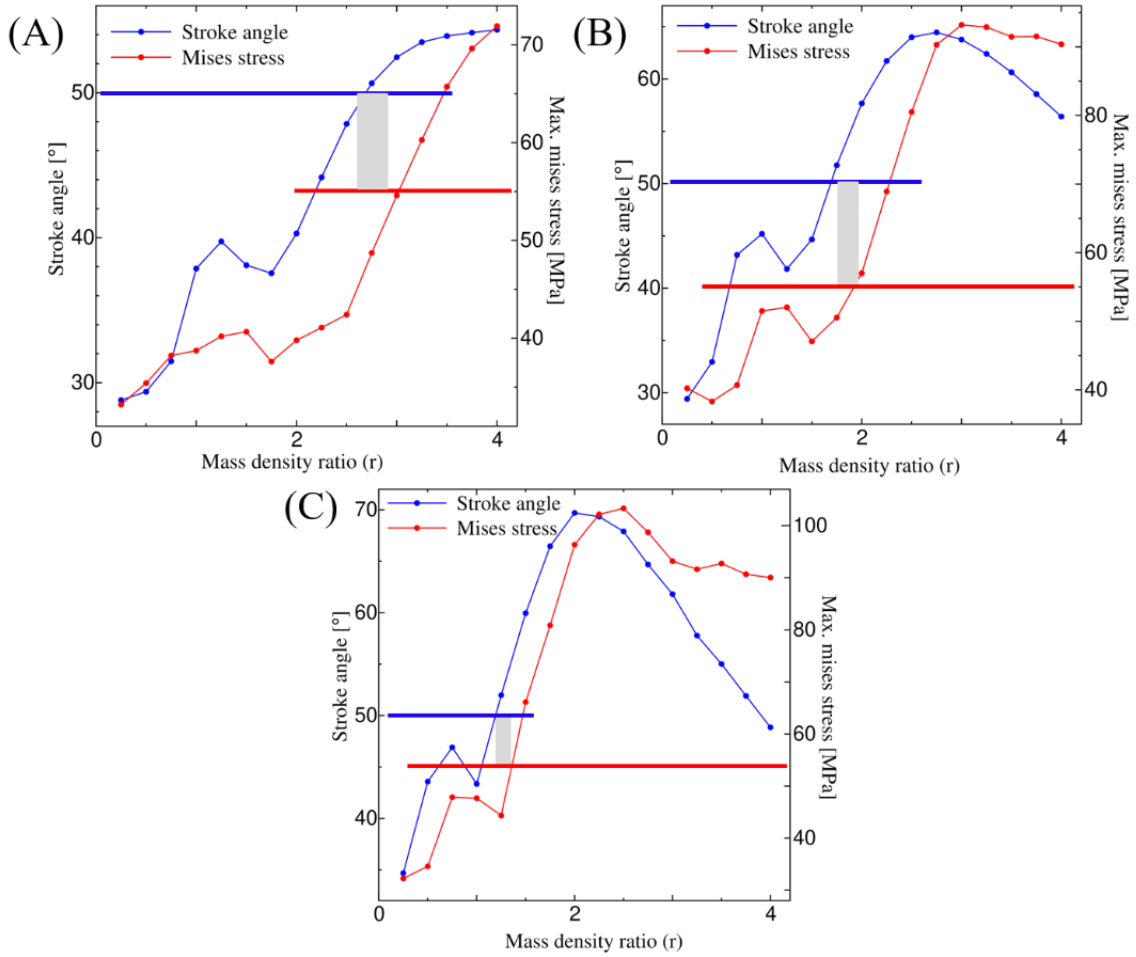

Figure 3.14: DW search results using the parametric study on r for f = 100 Hz (A), 125 Hz (B), and 150 Hz (C). The horizontal red and blue line indicates the DRs (A) and (B) given by Eqs.(3.2) and (3.5), respectively

3.4 Design window search for the micro wing

In this section, initially the dimensions of the micro wing are given using morphological and kinematic parameters of dipteran insects [158]. The DW is searched for the leading-edge cross-section or the leading-edge width w_{LE} and thickness t_{LE}, and the extended length of the leading-edge L_e using linear static stress analysis, where the mass of the micro wing m_w is restricted to satisfy the DW-3 sufficiently.

3.4.1 Basic micro wing design based on actual dipteran insects

The micro wing has been initially designed using the morphological and kinematic parameters of a model dipteran insect, Eristalis Tenax, as shown in Table 3.3 [70]. Depending upon the actuator size, the spanwise length of the micro wing has been considered as 10 mm. Using the spanwise length and the aspect ratio from Table 3.3, the chordwise length of the micro wing has been evaluated as

$$r_a = 2\, L_w / c_m, \tag{3.9}$$

where r_a is the aspect ratio, L_w is spanwise length, and c_m is the chordwise length of the micro wing, respectively.

The wing membrane thickness t_w has been evaluated using the dynamic pressure force and the torsional stiffness, which can be observed in the wing motion as shown in Fig. 3.15. The wing's feathering motion is being simplified as the deflection of the cantilever beam due to dynamic pressure force [46, 55, 57], which is schematically shown in Fig. 3.16 [59]. The deflection of the cantilever beam is given as follows-

$$\theta = \frac{F_L c_m^2}{6 E I_w}, \tag{3.10}$$

where θ is the feathering angle, E is the modulus of elasticity of PN-2000 see Table 3.1, and I_w is the moment of inertia of the wing membrane, which is defined as $L_w t_w^3/12$.

To maximize the lift force, the feathering angle should be about 45° [59]. Using the Eqs.(3.6), (3.7), and (3.10), the membrane thickness is calculated, and its value is 6.1 μm.

Table 3.3: Kinematic and morphological parameter of Eristalis Tenax [70]

Span length (L_w) (mm)	Mass (mg)	Aspect ratio (r_a)	Dimensionless radius of second moment area (r_2)	Stroke angle (°) (Φ)	Flapping frequency (f) (Hz)
11.4	90.2	7.23	0.54	107.5	160.5

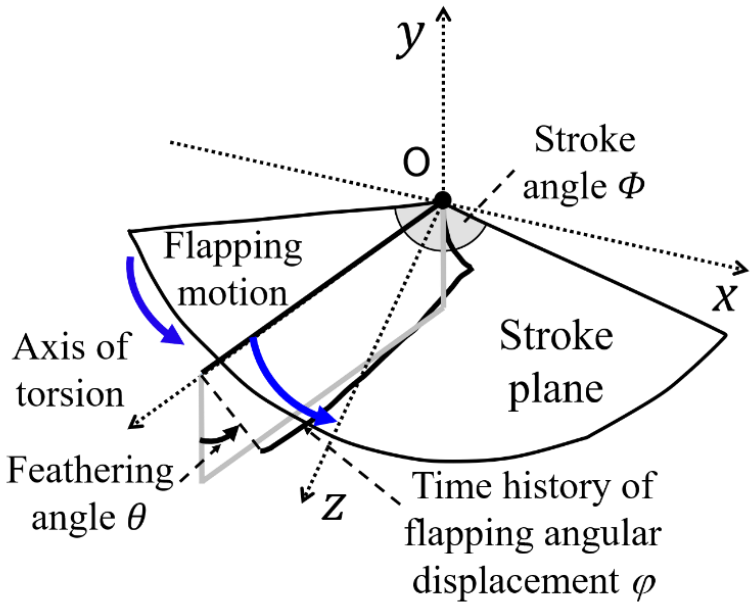

Figure 3.15: Schematic view of insect's wing motion

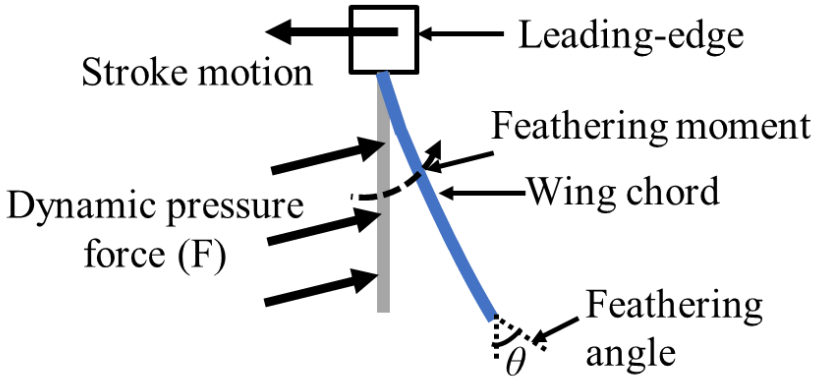

Figure 3.16: Insect's wing feathering motion in a simplified view

3.4.2 Leading-edge design as a support structure using stress analysis

Using the basic micro wing design from the previous section, the detailed design of the micro wing was done. That is, the leading-edge has been designed as a support structure based on the static stress produced due to the dynamic pressure as shown in the problem setup for linear static stress analysis, see Fig. 3.17. In this problem setup, the material distribution is given as follows: The two different PI materials are used for the leading-edge and the wing membrane as shown in Table 3.1. The load and boundary conditions are given as follows: The right end of the leading-edge beam is completely fixed, whereas the fluid drag

pressure force evaluated using a quasi-steady assumption is applied all over surfaces. This setup is used in the NASTRAN solver for linear static finite element analysis with quadrilateral shell elements. To search the DW for w_{LE} and t_{LE}, L_e is fixed as 50μm initially. The drag pressure force P_D can be evaluated using the following equation [159]:

$$P_D = 0.5\,\rho^f\,C_D\,V_{max}^2, \tag{3.11}$$

where V_{max} is the maximum flapping velocity, which is defined as

$$V_{max} = (8/3)\,\Phi f\,r, \tag{3.12}$$

where r is the distance from the wing base to its tip i.e., $r = L_w + L_e$, the stroke angle Φ is set as 107.5º, the flapping frequency f is set as 160.5 Hz, the drag coefficient C_D is set as 2 [59], and ρ^f air density is set as 1.205 kg/m^3.

Fig. 3.18 shows the maximum Mises stress σ_M against the leading-edge width and thickness. Using this figure, firstly the DW is searched for w_{LE} as follows: The lower limit for w_{LE} is given as 200 μm, in order to support the wing membrane, whereas the upper limit for w_{LE} is given as 900 μm in order to satisfy the limit of m_w from DW-3 sufficiently. Hence, DW-4 is given as

$$\text{DW-4} = \{(w_{LE}, t_{LE}, L_e) \mid 200\ \mu\text{m} \le w_{LE} \le 900\ \mu\text{m}, L_e = 50\mu\text{m}\}. \tag{3.13}$$

Using Fig. 3.18 and DW-4, a new DW is searched for t_{LE} to satisfy the DR (A) as formulated in Eq.(3.2). The DW for t_{LE} is obtained as follows: As shown in Fig. 3.18, the DR (A) as $\sigma_M < 54.5$ MPa (see Eq.(3.2)) is satisfied for t_{LE} larger than about 100μm. Hence, the lower limit for t_{LE} is given as 100 μm. Whereas, the upper limit is given as 125 μm because the further increase in t_{LE} does not affect σ_M. Hence, DW-4 is given as

$$\text{DW-5} = \{(w_{LE}, t_{LE}, L_e) \mid 100\ \mu\text{m} \le t_{LE} \le 125\ \mu\text{m}, 200\ \mu\text{m} \le w_{LE} \le 900\ \mu\text{m}, L_e = 50\mu\text{m}\}. \tag{3.14}$$

Using DW-5, an extended length of the micro wing has been designed. In the problem setup in Fig. 3.17, the leading-edge cross-section w_{LE} and t_{LE} are chosen as 400 μm and 120 μm, respectively, from DW-4 and DW-5 because of the fabricability issues such as the thickness of PI material is 40μm [9]. The load and boundary conditions are set as described in the above.

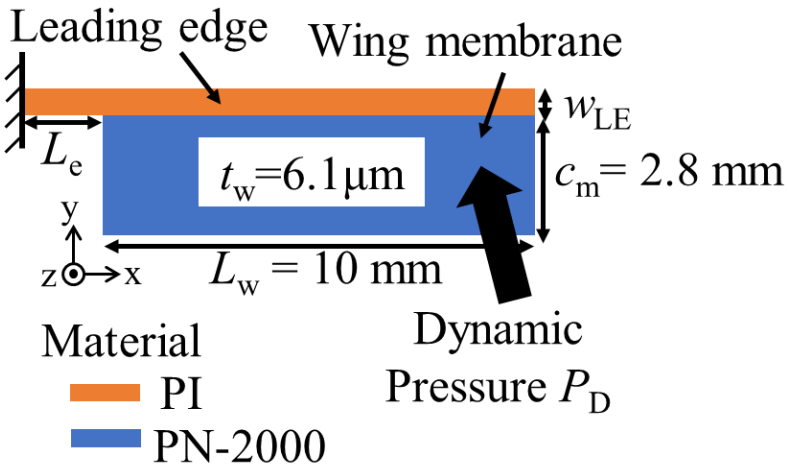

Figure 3.17: Problem setup for the design of leading-edge and extended part length of the micro wing

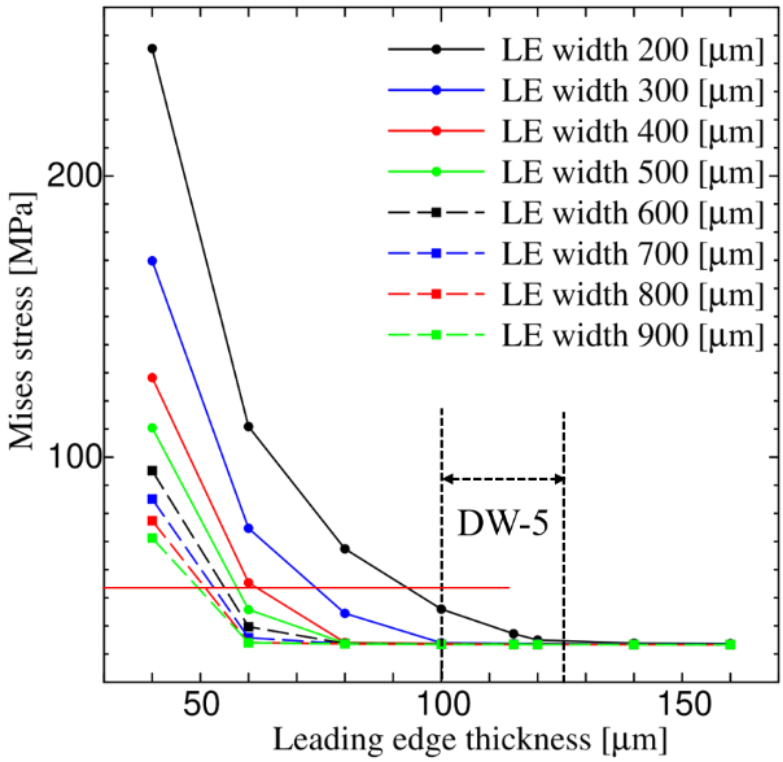

Figure 3.18: DW search results for the leading-edge cross-section. The horizontal red line indicates the DR (A) given by Eq.(3.2)

Fig. 3.19 shows the relationship between σ_M and L_e. Using this figure, the DW for L_e is obtained as follows: The lower limit for L_e is given as about 2.0 mm, which is about 50% of the wing attachment length (3.9 mm) because of the fabricability, whereas the upper limit for L_e is given as about 2.8 mm to satisfy the DR (A) as $\sigma_M < 54.5$ MPa (see Eq.(3.2)). Hence, DW-6 is given as

$$\text{DW-6} = \{(w_{LE}, t_{LE}, L_e) \mid 2\ \text{mm} \le L_e \le 2.8\ \text{mm},\ w_{LE} = 400\ \mu\text{m},\ t_{LE} = 120\ \mu\text{m}\}. \tag{3.15}$$

Finally, we determined a design solution for the micro wing as shown in Fig. 3.20 using DW search over it. This solution will be fabricated using polymer micromachining as fabricated earlier [54].

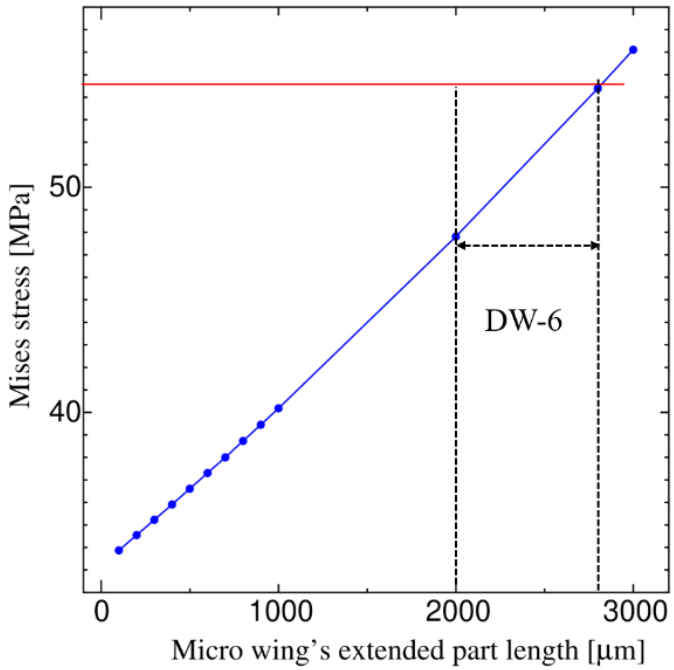

Figure 3.19: DW search results for the extended part length of the micro wing. The horizontal red line denotes the DR (A) given by Eq.(3.2)

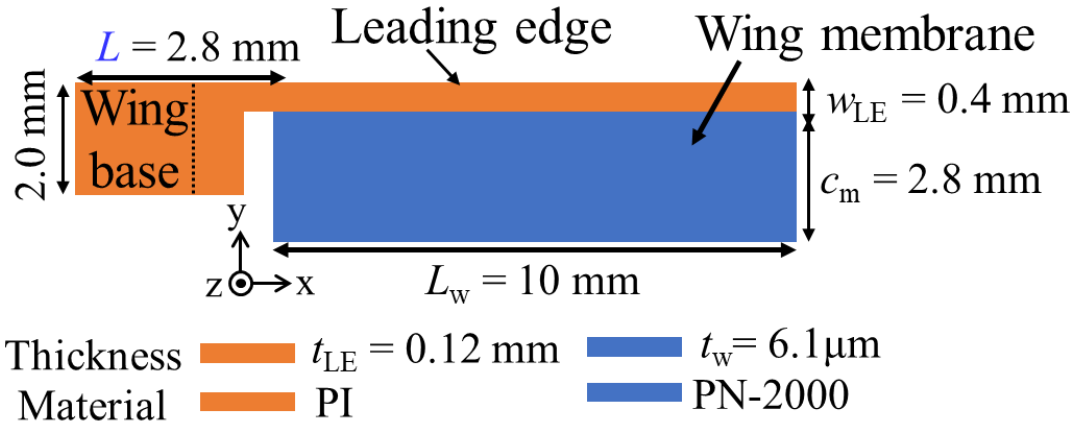

Figure 3.20: A design solution for the micro wing

3.5 Design window search for miniaturizing the flapping wing nano air vehicle

The design solutions of the micro transmission and the wing from the previous DWs are combined and lead to the initial design solution for further miniaturizing FWNAVs using the design window search for the design parameter space (f, h, L_s), where f, h, and L_s are the flapping frequency, the elastic hinge gap, and the length of the support frame, respectively, whereas the other design parameters w_{LE}, t_{LE}, and L_e are set as 400 μm, 121.1 μm, and 2.8 mm, respectively, along with the piezoelectric bimorph design for maintaining the forced vibration's amplitude U_x as 81 μm.

3.5.1 Model selection for the flapping wing nano air vehicle design

The computational models for FWNAVs with and without membrane are shown in Figs. 3.21(A) and (B), respectively. Firstly, their results are compared to select the model in the following DW search. In the problem setups shown in Figs. 3.21(A) and (B), the harmonic forced displacement $u_x = U_x \times \sin 2\pi ft$ (the vibration amplitude U_x, and f = 125 Hz, which is the intermediate frequency in DW-2) is applied to the area of the supporting frame, where the free end of the piezoelectric bimorph is attached. The evaluation of U_x from the piezoelectric bimorph actuator was discussed in Chapter 2 [9]. The fixed boundary condition is applied to the area of the supporting frame, where the fixed end of the piezoelectric bimorph is attached. The finite element mesh with 21,292 elements and 107,185 nodes is used for the model with the wing membrane, whereas the finite element mesh with 20,792 elements and 103,585 nodes is used for the model without the wing membrane. The time increments $\Delta t = T/4000$ and $T/500$ are used for the models with and without the membrane, respectively, where T is the flapping period, which is equal to the inverse of f. The far smaller time increment is necessary for the model with the membrane to avoid the convergence issue of the nonlinear iteration coming from the thin membrane.

Table 3.4 shows the performance comparison between the models with and without the wing membrane. As shown in this table, considering the membrane for the present dynamic simulation don't change the major characteristics quantities significantly, while it increases the computational cost drastically.

Hence, in this study, we selected the model without the wing membrane for further parametric study on the FWNAV.

3.5.2 Flapping frequency selection

The DW-7 was searched to satisfy the DRs (A) and (B) using the parametric study on f, where f is selected from the range of 50 to 150 Hz with an interval of 25 Hz, while L_s and h are fixed as 26.9 mm and 160 μm, respectively, following our previous study in Chapter 2 [9]. Here, the DRs (A) and (B) are reformulated, respectively, as

$$\sigma_M < 75\% \text{ of the breaking stress}, \tag{3.16}$$

$$\Phi > 90°, \tag{3.17}$$

The stroke angle limit in Eq.(3.17) is selected since most dipteran insects (hoverfly or drone fly) [70, 73–75] fall in this range.

The stroke angle and the maximum Mises stress for the change of f are shown in Fig. 3.22. From this figure, the lower limit for f is given as 100 Hz because of Eq.(3.17), whereas the upper limit for f is given as 125 Hz because of Eq.(3.18) or $\sigma_M < 82$ MPa, of which value is obtained from Table 3.1. Hence, DW-7 is given as

$$\text{DW-7} = \{(f, L_s, h) \mid 100 \text{ Hz} \leq f \leq 125 \text{ Hz}, L_s = 26.9 \text{ mm}, h = 160 \text{ μm}\} \tag{3.18}$$

The flapping frequency chosen for FWNAV from DW-7 will be further studied to enhance the performance via strengthening the hinge supporting beam (see Fig. 3.9), which can be possible either by increasing the thickness of the support frame or shortening the support frame. In the following section, the latter way has been chosen because of the miniaturization objective.

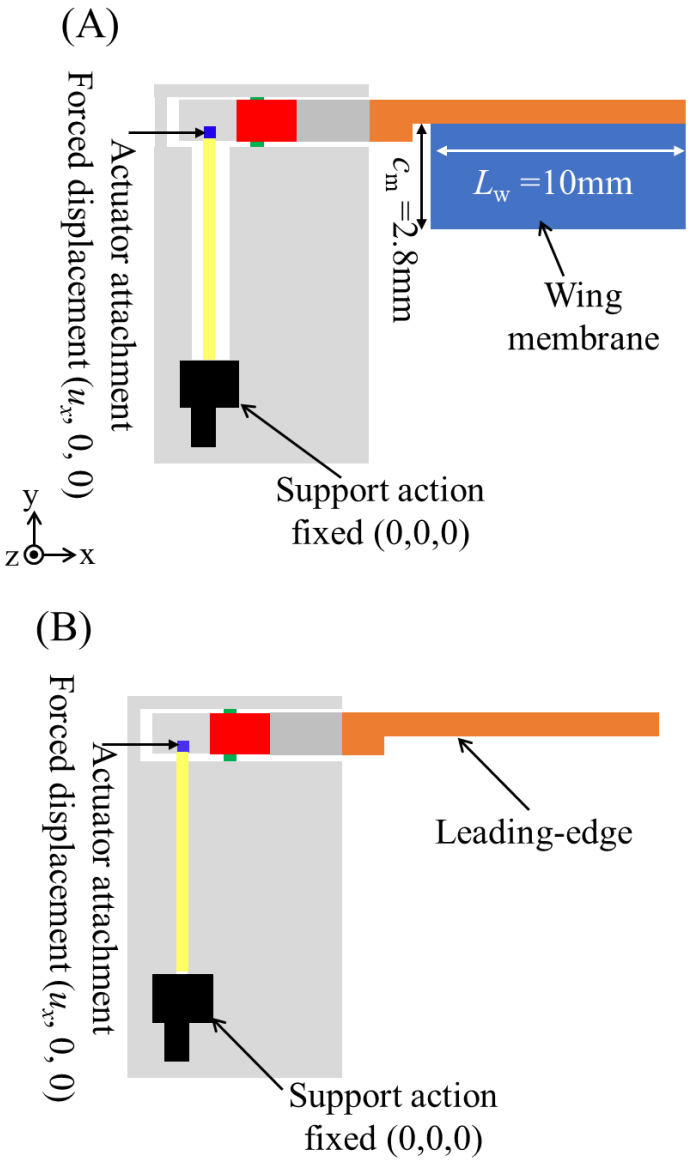

Figure 3.21: The initial design of FWNAV with a membrane (A), without membrane (B)

Table 3.4: Performance and computation cost comparison in FWNAV with and without membrane

FWNAV	Max. Flapping velocity (m/sec) % Change	Stroke angle (º) % Change	Max. Mises stress (MPa) % Change	Computational cost % Change
Without membrane	9.40 (Base)	100.69 (Base)	79.25 (Base)	12 (Base)
With membrane	8.75 (-6.92%)	81.26 (-19.30%)	88.31 (+11.43%)	144 (+91.67%)

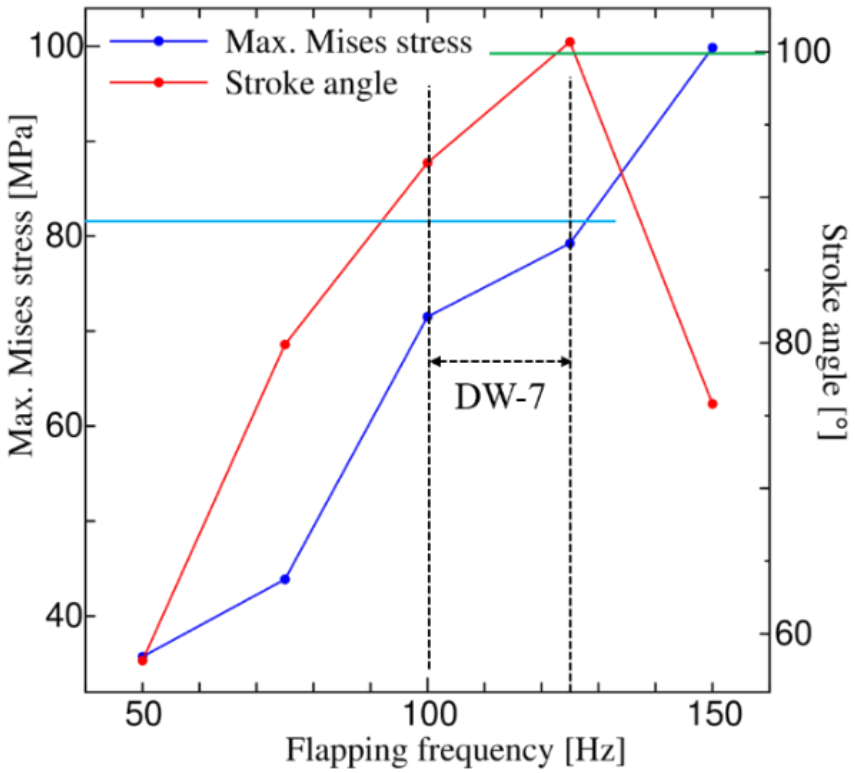

Figure 3.22: DW search result for flapping frequency selection for FWNAV. Horizontal light blue and the green line indicates the DRs (A) and (B) given by Eqs.(3.16) and (3.17), respectively

3.5.3 Miniaturization of the flapping wing nano air vehicle in the design window

This sub-section describes the miniaturization of FWNAV along with the aerodynamic lift force estimation for the frequency range selected in the previous section. Hence, the DW-8 for the DRs (A), (B), and (C) is searched using the parametric study on L_s, where f is chosen as 100 and 125 Hz from DW-7, and h is fixed as 160 μm from the previous study in Chapter 2 [9]. The DR (B) is already formulated as Eq.(3.17), while the DRs (A) and (C) can be formulated as

$$\sigma_M < 100\% \text{ of the breaking stress}, \tag{3.19}$$

$$U_{max} \geq 10 \text{ m/sec}, \tag{3.20}$$

where U_{max} is the maximum flapping velocity and its value is obtained using Eq.(3.6) such that the FWNAV would produce enough lift force to support the

weight of the initial design in Table 3.5. In this evaluation, the area of the micro wing S = 32 mm^2 as shown in Fig. 3.19, and the fluid mass density ρ^f = 1.205 kg/m^3 are used in Eq.(3.6).

Figs. 3.23(A) and (B) show the stroke angle, the maximum Mises stress, and the maximum flapping velocity for the various L_s with the chosen frequencies f = 100 and 125 Hz. Using these results, the DWs were searched as follows: The lower limit is selected to satisfy the DR (A) as $\sigma_M < 109$ MPa whereas the upper limit is set for DR (C) as $U_{max} \geq 10$ m/sec. Hence, DW-8 is given as

$$\begin{aligned} \text{DW-8} = \{(f, h, L_s) \,|\, & f = 100 \text{ Hz}, 2 \text{ mm} \leq L_s \leq 13 \text{ mm}, h = 160 \text{ μm}\}, \\ \text{or, } \{(f, h, L_s) \,|\, & f = 125 \text{ Hz}, 8 \text{ mm} \leq L_s \leq 15 \text{ mm}, h = 160 \text{ μm}\}. \end{aligned} \quad (3.21)$$

DW-8 indicates that L_s can be 2 to 15 mm for the selected frequency from the previous section.

Finally, the DW-9 for the DR (D) is searched using the parametric study on h. h is selected from the range of 160 to 280 μm with an interval of 40 μm because of the employed polymer micromachining manufacturability [9]. That is, the interval corresponds to a PI sheet thickness, and the maximum bound is due to the lamination difficulty [9].

Table 3.5: Components of FWNAV and their weight in the initial design to the miniaturized design

Components of FWNAV	Mass (mg) Initial design (L_s = 26.9 mm)	Mass (mg) Miniaturized design (L_s = 10 mm)
Transmission with support frame	76.30	33.26
Micro wing	1.88	1.88
Bimorph Actuator	289	120
Total mass	367.18	155.14

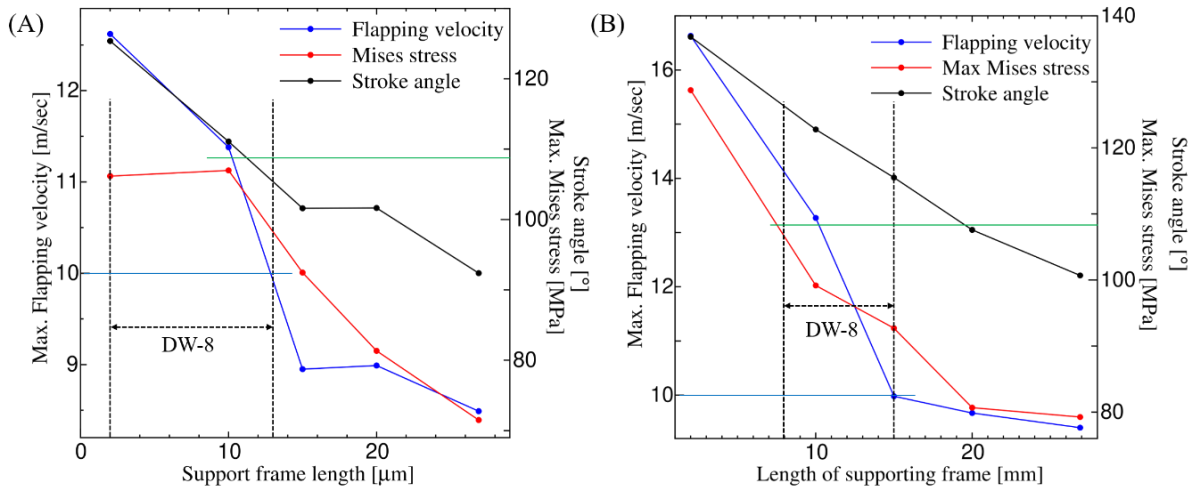

Figure 3.23: Miniaturization in FWNAV without membrane with f =100 Hz (A), and 125 Hz (B). Horizontal green and light blue lines indicate the DRs (A) and (C) given in Eqs.(3.19) and (3.20), respectively

The other parameters are chosen from the DW-8 as follows: f is fixed as 100 Hz, and L_s is chosen as 10 mm. Hence, we can draw our design window search process for miniaturizing the FWNAV in conceptual and actual views, respectively, in Figs. 3.24(A) and (B) show. Note that the reason why L_s = 10mm is selected as our final solution in miniaturization is because of the limitation of the available piezoelectric bimorph actuator as described in Section 3.5.4.

Tables 3.6 show the gap between sections A and B in Fig. 3.9 for h with L_s= 10mm. Note that a negative gap means sections A and B contact each other. Using these tables, the DW is obtained for DR (D) as

$$\text{DW-9} = \{(f, h, L_s) \,|\, f = 100 \text{ Hz}, L_s = 10 \text{ mm}, 240 \text{ μm} \leq h < 280 \text{ μm}\}. \quad (3.22)$$

Fig. 3.24 shows the stroke angle, the maximum von Mises stress, and the maximum flapping velocity for DW-9. As shown in this figure, the performance characteristics are decreasing with the increase of the hinge gap. As shown in this figure, the DW-9 satisfies DR (A) given by Eq.(3.19). On the contrary, Eq.(3.20) corresponding to DR (C) should be revised because of miniaturizing the FWNAV as follows: As per Table 3.5, which shows the revised weights as well as the initial one, DR (C) for L_s = 10 mm are reformulated as

$$U_{\max} \geq 7 \text{ m/sec}, \quad (3.23)$$

Hence, DW-9 satisfies the DRs (A) and (C) completely. On the contrary, the DR (B) given by Eq.(3.17) is partially satisfied as shown in Fig. 3.25. However,

the minimum stroke angle in DW-9 is 80°, and it is close to the bound of Eq.(3.17). Hence, we can evaluate the DW-9 sufficiently satisfies the DRs (A)–(D).

The deformation of the computational model of the FWNAV during the upward flapping motion and the von Mises stress distribution in the transmission for f = 100 Hz, L_s = 10mm, and h = 280μm are shown in Figs. 3.26 and 3.27. As shown in these figures, these quantities have a correlation. As the magnitude of the upward or downward flapping motion increases, the stress concentrated at the corners of the hinge end fixed by the supporting beam is also increased. Fig. 3.26 indicates that the σ_M occurs in the lower elastic hinge.

In order to show this relationship more quantitatively, the time histories of the flapping angular displacement φ and the maximum von Mises stress σ_m are shown in Figs. 3.28(A) and (B), respectively. Note that σ_m usually occurs at the lower corner of the T-shaped hinge fixed by the supporting beam except for the specific time instants, which are discussed in detail below.

(A)

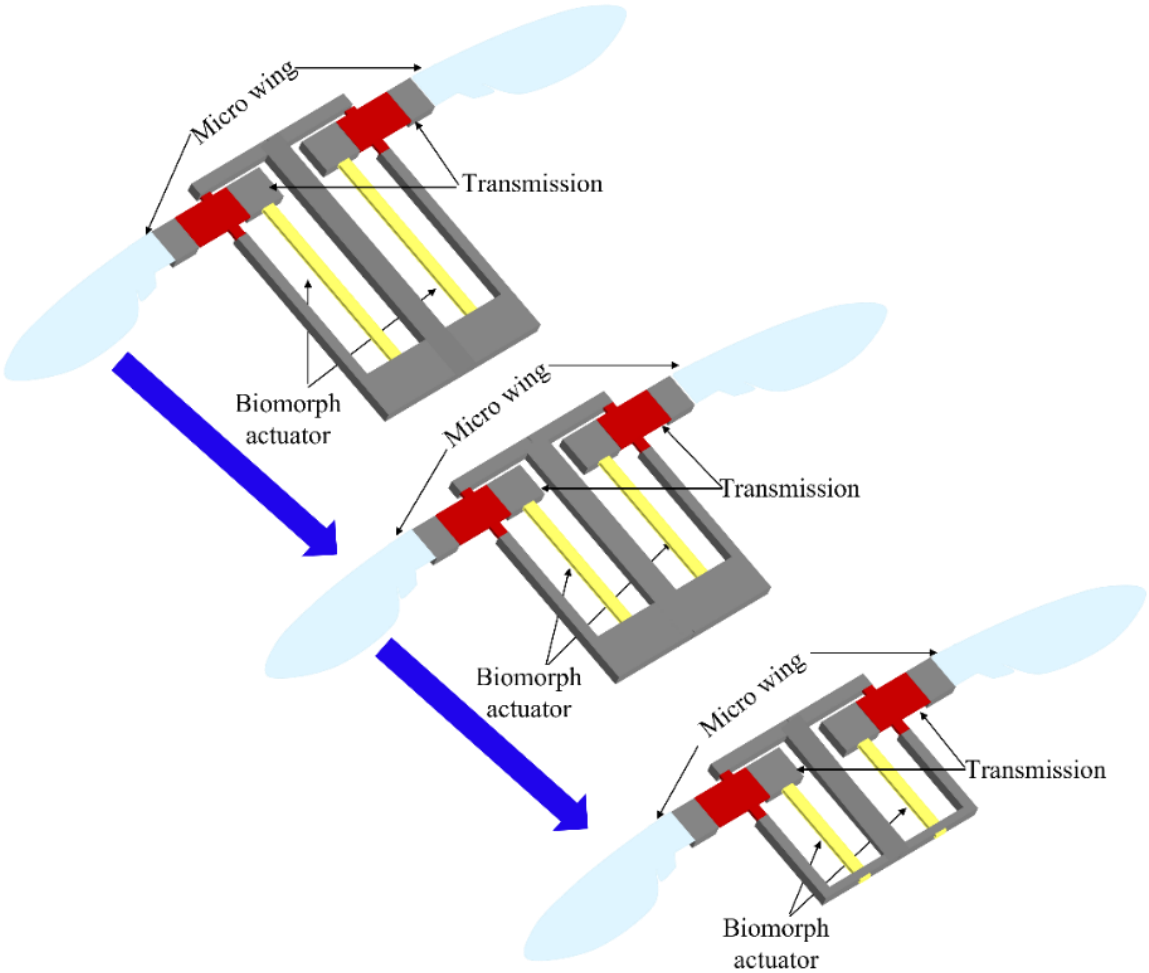

(B)

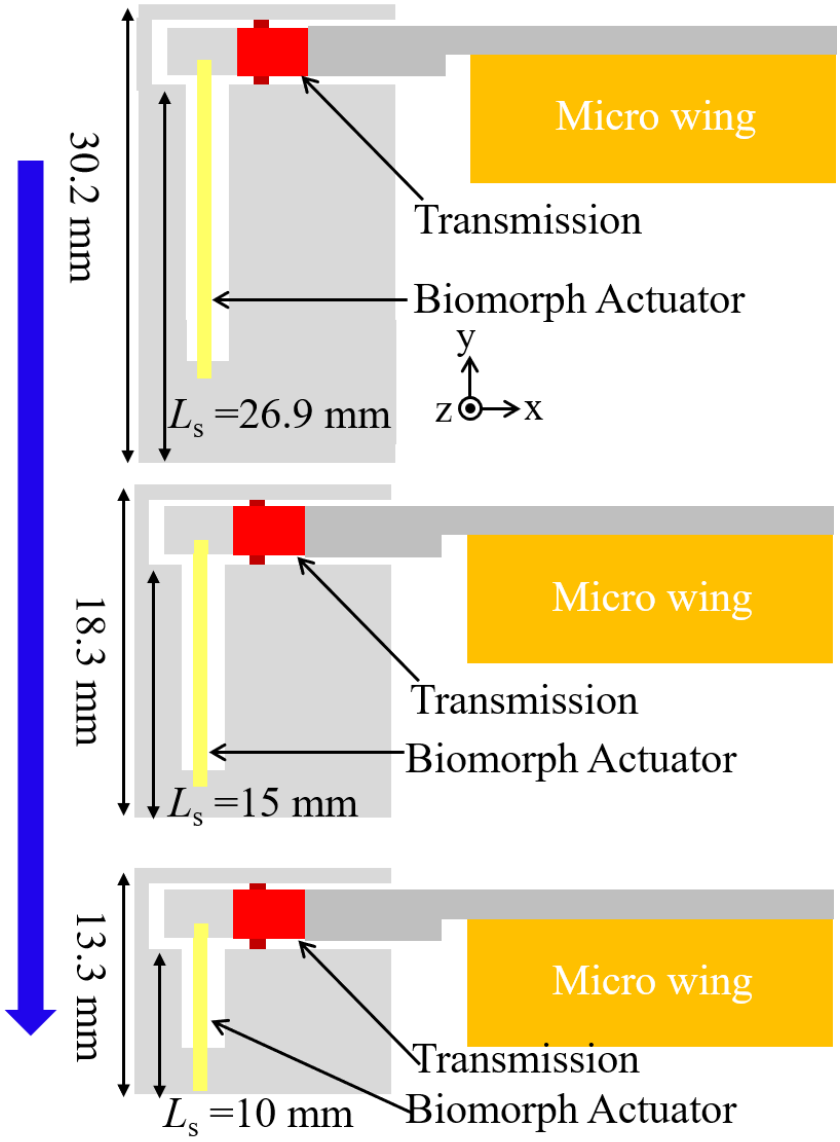

Figure 3.24: Miniaturization of the FWNAV in both the conceptual view (A) and the actual view (B)

Table 3.6: Out-of-plane positions of sections A and B, and their gap for *Ls* = 10 mm and *f* = 100 Hz

Hinge gap, *h* (μm)	Z_A (μm)	Z_B (μm)	Z_A - Z_B (μm)	Sticking
160	402.92	534.63	-131.71	Yes
200	401.21	468.81	-67.60	Yes
240	369.22	338.94	30.28	No
280	331.02	220.88	110.14	No

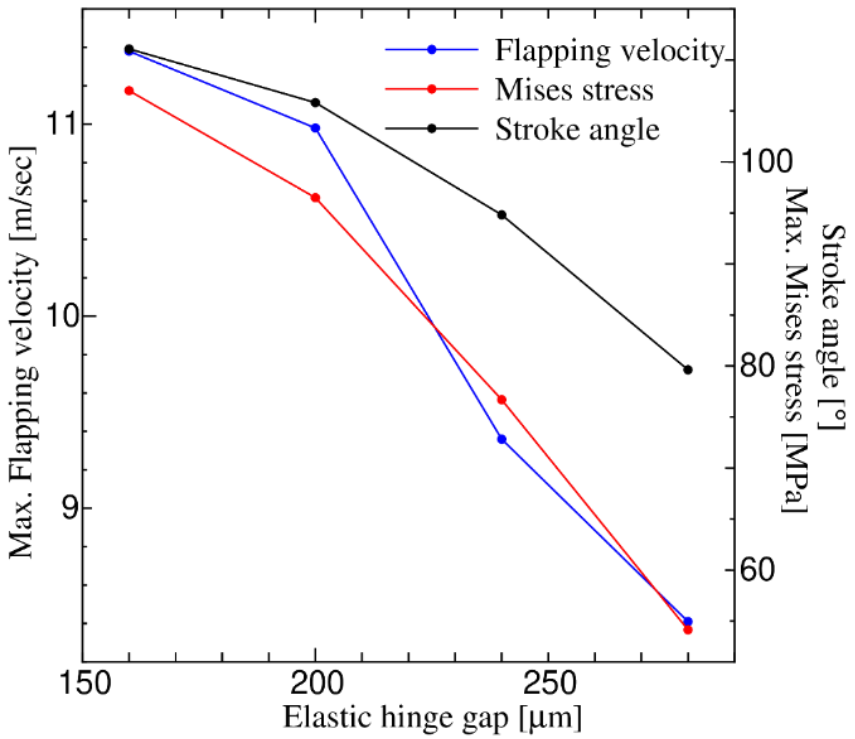

Figure 3.25: Elastic hinge gap study in the DW search result of miniaturization for f =100 Hz with L_s = 10mm

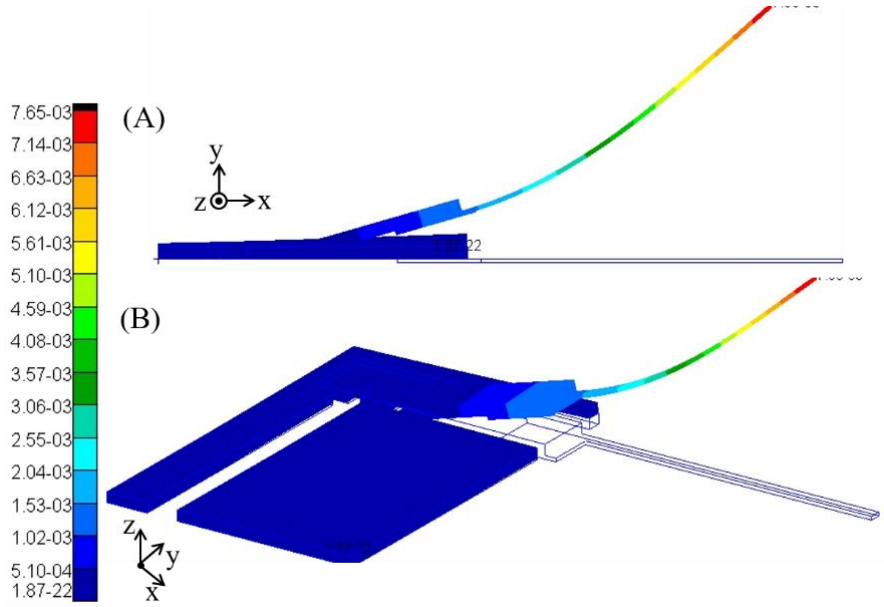

Figure 3.26: Deformation of the computational model of the FWNAV with h= 280 μm and L_s = 10 mm during the upward flapping motion for f = 100 Hz. The color contours indicated the magnitude of the deformation in unit of m. (A) *xz* plane view. (B) bird's-eye view

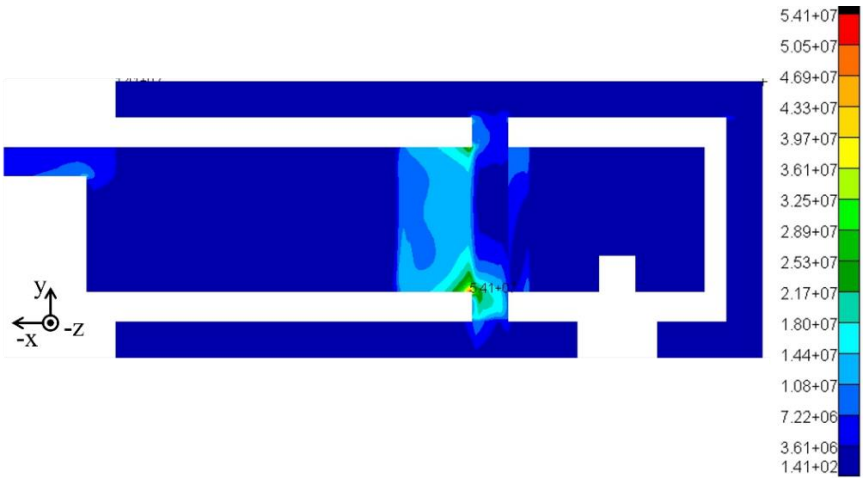

Figure 3.27: Distribution of the von Mises stress in the transmission of the computational model of the FWNAV with h= 280 μm and L_s = 10 mm during the upward flapping motion for f = 100 Hz. The color contour shows the magnitude of von Misses stress in unit of Pa

As shown in Fig. 3.28, the clear correlation between these values can be observed at the time instants of about 0.003 sec and 0.007 sec, since the significant peaks of these values occur at these time instants. The extra small peaks in the time history of σ_m, which don't have the corresponding peaks in the time history of φ, occur due to the change of the location where σ_m occurs. This change occurs due to a slight twisting of the wing attachment.

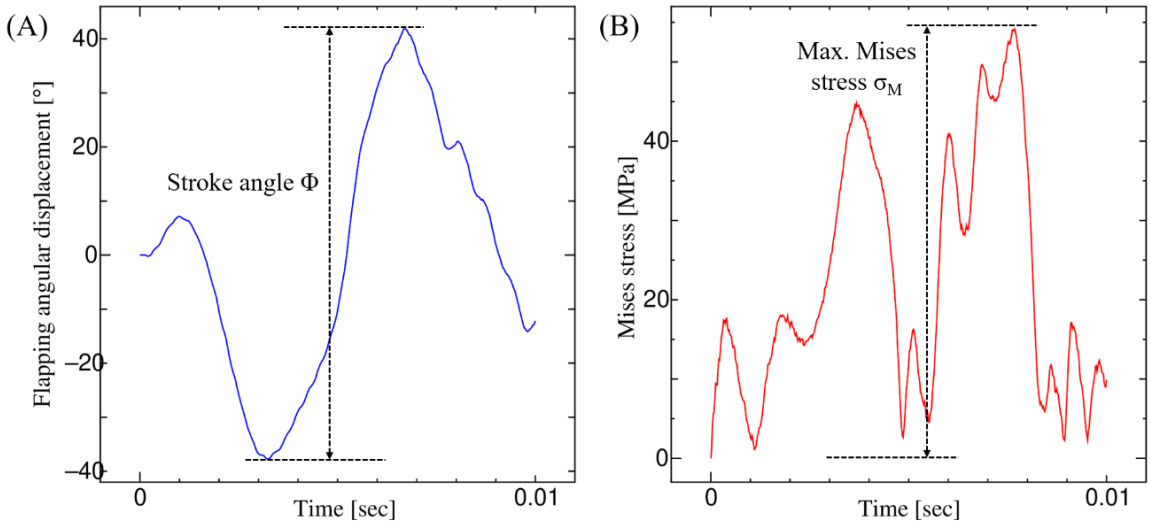

Figure 3.28: Time histories of flapping angular displacement (A) and Mises's stress (B) for FWNAV without membrane with h= 280 μm and Ls = 10 mm

3.5.4 Piezoelectric bimorph actuator design

During the DW search process, a vibration amplitude U_x was considered as the constant value of 81μm [9], which was evaluated using the equilibrium between the reaction forces of the actuator and the transmission with the actuator's length L_a = 20 mm in Chapter 2. However, U_x will change according to the change of L_s from 20mm to 10mm following the minimization in Section 3.5.3. Hence, in this section, the bimorph actuator is designed for the DW-9, which is the final DW, to generate the constant vibration amplitude.

The actuator and transmission reaction forces against the displacement are presented in Fig. 3.29. U_x can be evaluated as their equilibrium point. The transmission reaction force was obtained by a nonlinear static analysis using the Marc solver for the 2-D model of the transmission [56], whereas the actuator reaction force is theoretically evaluated [150] for the problem setup shown in Fig. 3.30 as follows:

The free displacement δ without any load and the blocking force F are given as

$$F = \frac{3E_p w\delta}{2L_a^3}\left[\frac{t_p^3}{3}+t_p\left(t_m+t_p\right)^2+\frac{E_m t_m^3}{6E_p}\right], \tag{3.24}$$

$$\delta = \frac{6E_p d_{31} V(t_m+ t_p)L_a^2}{2E_p\left(3t_m^2 t_p+6t_m t_p^2+4t_p^3\right)+E_m t_m^3}, \tag{3.25}$$

where d_{31} = 1.98 × 10^{-10} m/V is the piezoelectric constant, L_a = 10 mm is the length of the actuator, E_p = 61 GPa is the Young's modulus of the piezoelectric material, E_m = 140 GPa is the Young's modulus of the metal shim, t_p = 0.2 mm is the thickness of the piezoelectric material, t_m = 0.1 mm is the thickness of the metal shim, w = 3 mm is the width of the actuator, and V is the applied voltage, where the maximum applied voltage is chosen 500 V to investigate the minimum possible length of the actuator. Note that, for the purpose of maximizing the translational displacement from the biomorph actuator, the parallel connection is used here as shown in Fig. 3.30 [151].

In Fig. 3.29, the values of h = 240 and 280 μm have been selected as par the DW-9 discussed in Section 3.5.3, and V = 200 V has been chosen to demonstrate the evaluation of U_x. Note that L_a = 5 mm as well as L_a = 10 mm, which corresponds to the DW-9, has been presented to examine the limitation of L_a. As shown in Fig. 3.29, it is difficult to find the equilibrium point for L_a smaller than 5 mm because of larger actuator stiffness. Hence, in this study, we have selected L_a = 10 mm.

As shown in Fig. 3.29, the equilibrium point is shifted towards the right as the hinge gap h increases, and, consequently, U_x increases. In addition to this effect, of course, U_x will be further increase as the voltage V increases. Hence, the effect of h and V on U_x has been studied for the DW-9 in Fig. 3.31. As shown in this figure, the effect of h on U_x is not so significant for the case of L_a = 10 mm and V = 200V, that is, only a 2.52% increase of U_x for a 16.67% increase of h. Using the same figure, the required voltage to produce U_x = 81 μm for the DW-9 can be estimated as the range from 310 to 325 V.

Further, the effect of actuator width w on voltage requirement for constant vibration amplitude U_x has been studied to reduce the stiffness of the actuator which directly depends upon the width w following Eq.(3.23). In this study, actuator width w has been reduced 1/3rd and 1/6th of the original values to reduce the actuator stiffness.

Fig. 3.32 shows the relationship between the actuator width w and actuator voltage V. As shown in this figure, voltage requirement for the constant vibration amplitude U_x is increasing to 460V with decrease of width . However, the increase in voltage V can be justified by the decrease in total weight of FWNAV, equivalent to model insect's weight, drone fly or Eristalis Tenax. This weight of FWNAV based on optimization of actuator dimension has been used in next chapter.

In this way, the DW search process was completed. Finally, the fatigue life or the DR (E) was estimated for the final design solution given from the DW-9 in the next section.

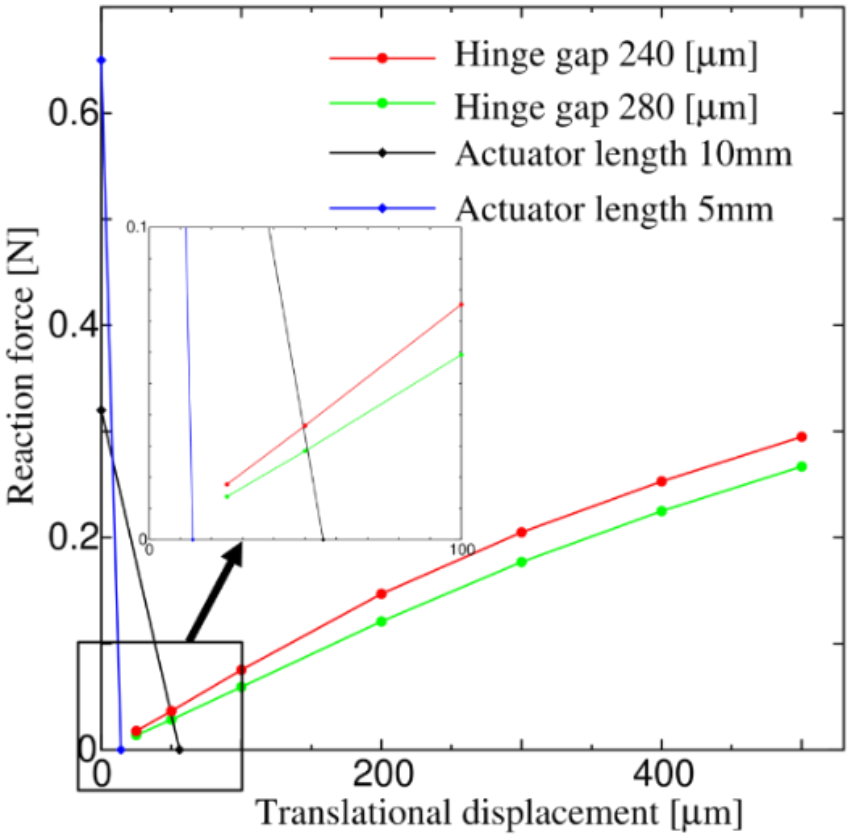

Figure 3.29: Evaluation of translational forced displacement (vibration amplitude U_x) for actuator design as per DW-9 with applied voltage 200 V. Note actuator length 5 mm is used to show limitation of this actuator

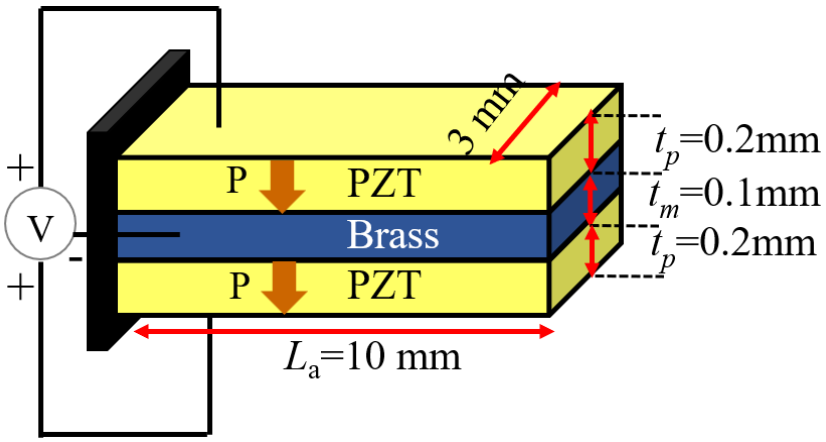

Figure 3.30: Bimorph actuator problem setup

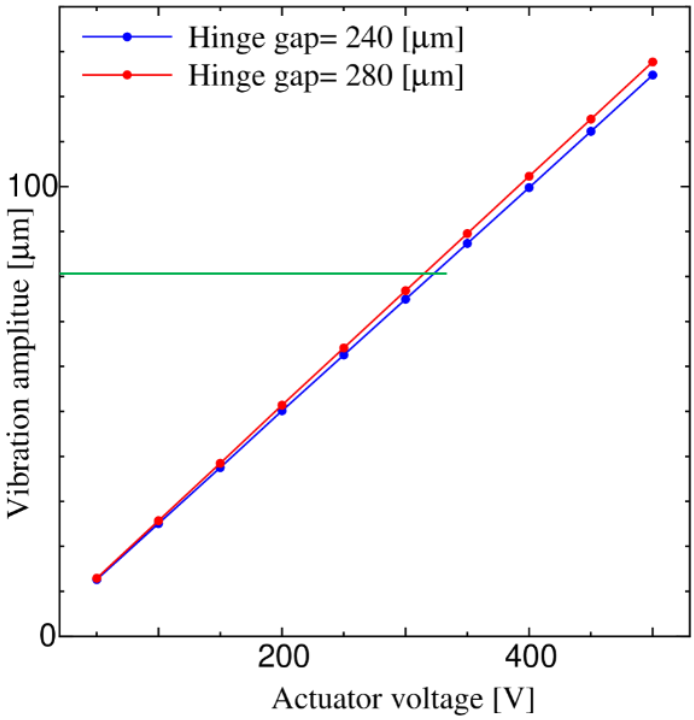

Figure 3.31: Effect of the elastic hinge gap h and voltage V on the vibration amplitude U_x for the actuator's length L_a = 10 mm. The horizontal green line indicates the U_x = 81 µm

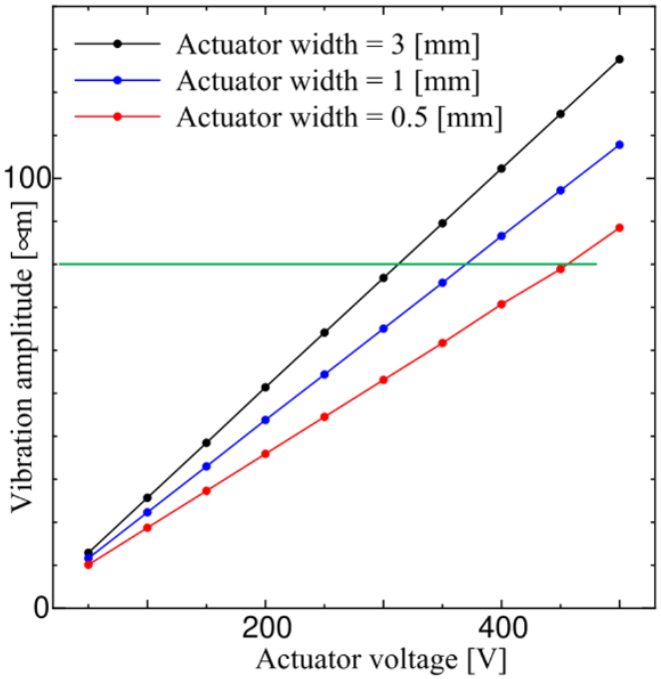

Figure 3.32: Effect of actuator width w on voltage requirement for constant vibration amplitude U_x. The horizontal green line indicates the U_x = 81 µm

3.5.5 Fatigue life estimation for the miniaturized flapping-wing nano air vehicle

As shown in Fig. 3.28(B), the maximum von Mises stress in space σ_m oscillates following the flapping motion of the FWNAV. Since the maximum von Mises stress in space and time σ_M is in the range of 54.15–76.70 MPa approximately for the DW-9 as shown in Fig. 3.25, the amplitude of the stress oscillation σ_A can be estimated as 54.15 MPa $\leq \sigma_A \leq$ 76.70 MPa.

From the detailed observation of the stress distribution in the FWNAV, σ_M occurs at the sharp corners of the lower elastic hinge because of the stress concentration as shown in Fig. 3.27. However, different from the numerical model as shown in Fig. 3.33(A), σ_A as well as σ_M will be further reduced in the actual fabrication due to the presence of fillet radius as shown in Fig. 3.33(B).

Based on the lower elastic hinge dimensions and the loading condition (bending), the stress reduction factor is about 1.9 [160]. Hence, σ_A can be finally estimated as 28.42 MPa $\leq \sigma_A \leq$ 40.37 MPa.

Under the assumption of similar material behavior among polyimides, the fatigue life of the transmission will be about 10^3– 10^4 cycles for this stress condition based on the S-N curve of a polyimide resin [161]. The DW-9 given by Eq.(3.22) satisfies the DR (F) sufficiently. Hence, the final design solution from the DW-9 satisfies all the DRs.

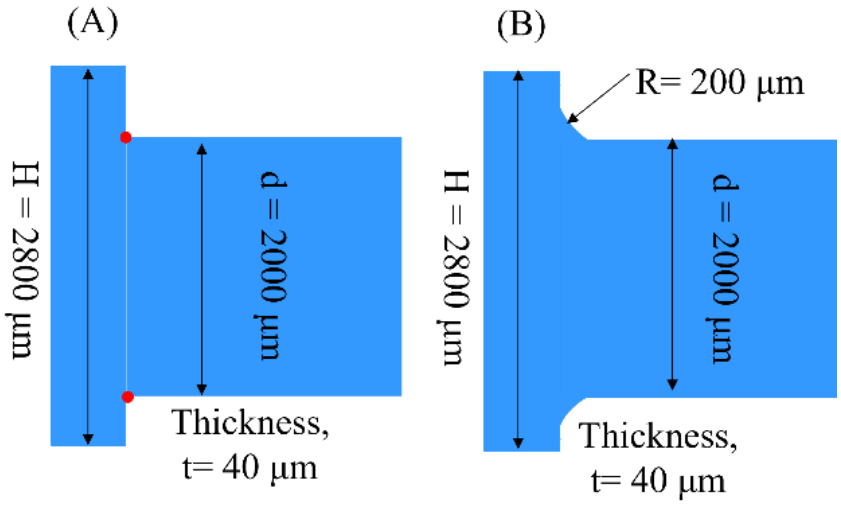

Figure 3.33: Lower elastic hinges in the numerical analysis (A) and the actual fabrication (B). The red circles show the points where the maximum von Mises stress occurs

3.6 Conclusion

In this chapter, I have proposed an iterative DW search using the nonlinear dynamic simulation and found the DW of the micro transmission as well as the FWNAV that satisfies the nonlinear and unsteady DRs conflicting with each other simultaneously. Each design solution in the DW shows a large stroke angle, which is comparable to that of the small flies, and it has a sufficient fatigue life. DW search of transmission shows that it produces a stroke angle of about 50° with fatigue life of about 10^3–10^7 cycles for the flapping frequency 100–150 Hz whereas the DW search on FWNAV indicates that it produces a stroke angle of about 90° with a fatigue life of about 10^3–10^4 cycles for the flapping frequency 100–125 Hz. The micro wing with the mass up to 5.3 mg can be supported by this transmission at the flapping frequency equivalent to the small flies. The proposed DW search results can miniaturize the FWNAV down to 10 mm. The DW search on available piezoelectric bimorph actuator and length of 10 mm indicates that a voltage of range 300–325V is required to produce a constant vibration amplitude. In future work I will fabricate the FWNAV based on the proposed DW using the polymer micromachining. This is highly possible because of a 2.5-dimensional structure can be easily fabricated by polymer micromachining. Hence, this study will contribute to the further miniaturization of FWNAVs.

CHAPTER 4

COMPUTATIONAL FLIGHT PERFORMANCE OF FLAPPING WING NANO AIR VEHICLES USING FLUID-STRUCTURE INTERACTION ANALYSIS

4.1 Introduction

In Chapter 3, I have designed the flapping wing nano air vehicles (FWNAVs), hence its flight simulation and performances should be evaluated [162] to estimate their net lift capacity which is the combination of aerodynamic lift force and inertial force that determines whether the developed FWNAV would produce enough lift to levitate the structure or not and also FWNAVs must produce enough lift and drag forces for hovering.

There are two approaches to predicting the flight performance of the developed FWNAVs; experimental and computational approaches. A computational approach would be better for the prediction of flight performance of the designed FWNAV because of Multiphysics and multisystem coupled analysis i.e., coupled physics between air and FWNAV structure. A large number of numerical simulations have been already conducted to investigate the relevant Multiphysics between the flexible wing structures and incompressible fluid [163–177], simply known as fluid-structure interaction analysis (FSI). FSI with a flexible micro wing becomes an essential tool to predict the flight performance of FWMAV/FWNAVs [55, 178–184] and at the same time, FSI analysis with micro wing replicates the insect flight through the surrounding airflow and provides sufficient passive wing deformation [185] as well as improvement in the aerodynamic performance [186].

The conceptual and detailed design of polymer micromachined FWNAVs has been already discussed in the previous chapters of this thesis. In this chapter, the flight performance of the polymer micromachined FWNAVs has been evaluated. using two computational methods: the first is the nonlinear dynamic analysis where only inertial and elastic forces are considered and the second is the FSI analysis where along with the inertial, and elastic forces, aerodynamic forces have also been considered. Therefore, the interaction between the micro wing and

surrounding air was simulated by simultaneously solving the incompressible fluid Navier-Stokes equation, the equation of motion for an elastic body, and the fluid-structure interface conditions using the three-dimensional finite element method [130, 187, 188].

Fig. 4.1 shows the research flow diagram to evaluate the flight simulation and performance of FWNAVs and further optimization of flight performance. According to the flow diagram, the input parameter (stroke angle and flapping frequency) for FSI analysis with a micro wing is given by the nonlinear dynamic analysis of FWNAV. FSI analysis with micro wing provides the lift coefficient which is used to calculate the lift force for nonlinear dynamic analysis of FWNAV. Finally, flight simulation and performance are compared between nonlinear dynamic analysis of FWNAV and FSI analysis with a micro wing to determine the flight performance of FWNAV and that provides the sufficiency of FSI analysis with a micro wing design over FSI analysis with FWNAV design for avoiding the computational complexity associated with the latter. In the end, flight performance has been optimized using the FSI analysis to support the weight of FWNAV.

4.2 Fluid-structure interaction analysis

FSI design is a key method for accurately predicting the 3-D strong coupling of the micro wing and the surrounding airflow. FSI design and simulation have been carried out using a computer program that has been already validated [46, 59, 187, 188]. Based on a detailed literature survey [46, 55, 58, 59, 64, 128, 130, 185–230], its important mathematical equations and other aspects are discussed here which are as follows.

4.2.1 Governing equation for fluid-structure interaction

The motion of the micro wing can be expressed by an equilibrium equation,

$$\rho^w \frac{dv_i^w}{dt} = \frac{\partial \sigma_{ij}^w}{\partial x_j} \tag{4.1}$$

where superscript w is denoted for the micro wing, d/dt = Lagrangian time derivative, ρ^w = Mass density of the material of micro wing, $v^w{}_i$ = i^{th} component of the micro wing velocity vector, and $\sigma^w{}_{\text{ij}}$ = ij^{th} component of the Cauchy stress tensor of the micro wing. Note that i and j denote the cartesian coordinate systems x, y, or z-direction, respectively.

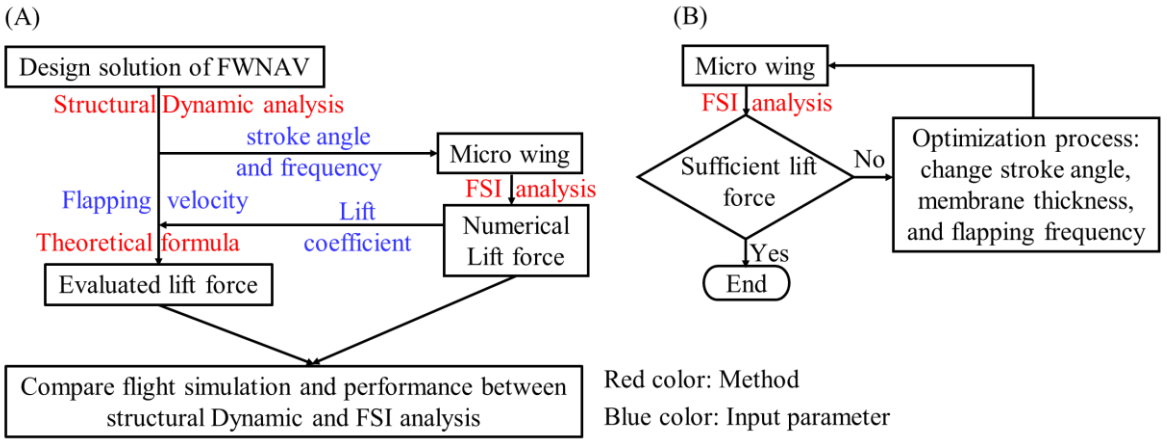

Figure 4.1: Research flow diagram for computational flight performance of FWNAVs (A) Optimization of flight performance (B)

The motion of the incompressible fluid can be programmed by the arbitrary Lagrangian-Eulerian (ALE) method and its motion can be given by Navier–Stokes (NS) equations which can be expressed as

$$\rho^a \frac{\partial v_i^a}{\partial t} + \rho^a (v_j^a - v_j^m) \frac{\partial v_i^a}{\partial x_j} = \frac{\partial \sigma_{ij}^a}{\partial x_j} \tag{4.2}$$

$$\frac{\partial v_i^a}{\partial x_i} = 0 \tag{4.3}$$

where, $\partial/\partial t$ =ALE time derivative, the superscript a denotes the respective quantity for air, ρ^a = mass density of the air, $v^a{}_i = i^{th}$ component of the air velocity vector, $v^m{}_i = i^{th}$ component of the velocity vector of the ALE coordinate, and $\sigma^a{}_{ij} = ij^{th}$ component of the Cauchy stress tensor of the air.

The interface conditions describing the interaction between the wing and the surrounding fluid can be expressed as

$$\sigma_{ij}^a n_j^a + \sigma_{ij}^w n_j^w = 0 \tag{4.4}$$

$$v_i^a = v_i^w \tag{4.5}$$

where $n^a{}_i$ and $n^w{}_i$ are the i^{th} components of the outward unit normal vectors on the air–micro wing interface corresponding to the air and the micro wing, respectively.

4.2.2 Monolithic equation system for fluid-structure interaction

A monolithic equation system for FSI can be formulated by applying finite element discretization to the nonlinear equilibrium equation of motion of micro wing, airflow, and interface condition as given by Eqs.(4.1)–(4.5) to obtain these equations in matrix form. Thus, a monolithic equation system can be written as

$$_{L}\mathbf{Ma} + \mathbf{Cv} + \mathbf{N} + \mathbf{q(u)} - \mathbf{Gp} = \mathbf{g} \tag{4.6}$$

$$_{\tau}\mathbf{Gv} = \mathbf{0} \tag{4.7}$$

where **M**, **C**, and **G** denote the mass, diffusive, and divergence operator matrices, respectively, and **N**, **q**, **g**, **a**, **v**, **u**, and **p** represents the convective term, elastic internal force, external force, acceleration, velocity, displacement, and pressure vectors, respectively, and finally the subscripts L and τ indicate the lumping of the matrix and the transpose of the matrix, respectively.

By applying state variable increment to the Eqs.(4.6) and (4.7) to obtain its linearized form,

$$\mathbf{M}^{*}\Delta\mathbf{a} - \mathbf{G}\Delta\mathbf{p} = \Delta\mathbf{g} \tag{4.8}$$

$$\gamma\Delta t_{\tau}\,\mathbf{G}\Delta\mathbf{a} + \mathbf{G}_{\varepsilon}\Delta\mathbf{p} = \Delta\mathbf{h} \tag{4.9}$$

where $\mathbf{M}^{*}$ = generalized mass matrix, **Δ** denotes the increment, *t* denotes the current time, and **Δg** and **Δh** are the residual vectors of Eqs.(4.6) and (4.7), respectively. **G**ε comes from the pressure stabilization [227], and using Newmark's method, the displacement and velocity increment can be written as **Δu** = βΔt2**Δa** and **Δv** = γΔtΔa. The pressure and elastic interior force terms are evaluated implicitly and the predictor–multicorrector algorithm is used for the time integration.

4.2.3 Projection method using algebraic splitting

If Eqs.(4.8) and (4.9) are solved using the monolithic method to satisfy the interface conditions, numerical instability occurs and formulation leads to an ill-conditioned equation system. In order to avoid this difficulty, a projection method using the algebraic splitting becomes necessary to use and it is as follows.

Eq.(4.6) can be linearized for the known pressure to predict the state variables as intermediate state variables, so

$$\mathbf{M}^{*}\Delta\hat{\mathbf{a}} = \Delta\mathbf{g} \tag{4.10}$$

where $\hat{\mathbf{a}}$ = intermediate acceleration. From Eqs.(4.10) and (4.8),

$$\gamma\Delta t\,\mathbf{G}\Delta\mathbf{p} = \mathbf{M}^{*}(\mathbf{v} - \hat{\mathbf{v}}) \tag{4.11}$$

where $\hat{\mathbf{v}}$ = intermediate velocity. In Eq. (4.11) multiplying both sides by ${}_{\tau}\mathbf{G}_{\mathrm{L}}\mathbf{M}^{-1}$,

$$\gamma\Delta t\,{}_{\tau}\mathbf{G}_{\mathrm{L}}\mathbf{M}^{-1}\mathbf{G}\Delta\mathbf{p} = {}_{\tau}\mathbf{G}\mathbf{v} - {}_{\tau}\mathbf{G}\hat{\mathbf{v}} + {}_{\tau}\mathbf{G}_{\mathrm{L}}\mathbf{M}^{-1}\bar{\mathbf{M}}^{*}(\mathbf{v} - \hat{\mathbf{v}}) \tag{4.12}$$

where $\bar{\mathbf{M}}^{*} = \mathbf{M}^{*} - {}_{\mathrm{L}}\mathbf{M}$. Eq.(4.12) can be written as

$$\gamma\Delta t\,{}_{\tau}\mathbf{G}_{\mathrm{L}}\mathbf{M}^{-1}\mathbf{G}\Delta\mathbf{p} = -{}_{\tau}\mathbf{G}\hat{\mathbf{v}} \tag{4.13}$$

if

$${}_{\tau}\mathbf{G}\mathbf{v} + {}_{\tau}\mathbf{G}_{\mathrm{L}}\mathbf{M}^{-1}\bar{\mathbf{M}}^{*}(\mathbf{v} - \hat{\mathbf{v}}) = \mathbf{0} \tag{4.14}$$

In the nonlinear iteration, $\hat{\mathbf{v}}$ approaching $\mathbf{v}$ as $\mathbf{M}^{*}$can be expected by linear convergence of the state variables so, Eq.(4.14) will be approaching 0 and satisfying unknown fluid velocity as described in Eq.(4.7).

Thus, in the above formulation using the algebraic splitting, the monolithic equation system is divided into the equilibrium Eqs.(4.8), (4.10), and pressure poison equation Eq.(4.13), and the Schur complement will never be produced.

4.2.4 Parallel computation environment

Since computational cost is very high for Eqs.(4.8), (4.10), and (4.13) in the iterative solver, so the below matrix-vector product should be considered to reduce computation cost using the parallel computation, under the assumption that the number of degrees of freedoms (DOFs) of the micro wing is very small compared to the surrounding air.

$${}_{\tau}\mathbf{G}_{\mathrm{L}}\mathbf{M}^{-1}\mathbf{G}\Delta\mathbf{p} \tag{4.15}$$

The parallel computation is possible using the mesh decomposition method as shown in Fig. 4.2 and from this figure, one can understand that surrounding air mesh Ω_{a} can be divided into several submesh such as Ω_{a1}, Ω_{a2}, …, etc and under the above-described assumption, micro wing mesh Ω_{w} is inside Ω_{a1}.

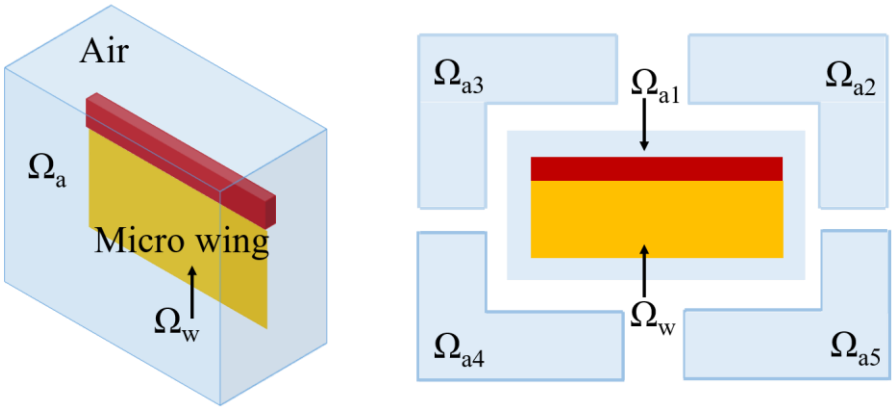

Figure 4.2: Decomposition of fluid mesh for parallel computation

For this setup, computational cost and complexity will be reduced by computing the matrix-vector product at one node of the surrounding air-micro wing interface. Parallel computation will be carried out in two steps as follow.

- Step 1: Eq.(4.15) can be computed using the element-by-element method at the computational node P_i (i= 1,2, 3…, N_d),

$$\mathbf{Ap} = \sum_e \mathbf{A}^{(e)}\mathbf{p}^{(e)} = \sum_e \mathbf{q}^{(e)} = \mathbf{q} \tag{4.16}$$

where **A** = Global matrix, **p** = Global vector, **q** = matrix-vector product, and e represents the element number.

- Step 2: In Eq. (4.16), at the interface between Ω_{ai} and Ω_{aj} ($j \neq i$), the matrix-vector product computed at P_j is transferred to P_i and finally add them to complete the corresponding nodal data computed in Step 1.

4.2.5 Modeling of a micro wing and surrounding fluid domain

During the FSI, a micro wing is designed using mixed interpolation of tensorial components (MITC) shell elements [228, 229] while surrounding air is designed using linear equal-order-interpolation velocity–pressure elements [227], and the same element's nodes are used for the interface of a micro wing and surrounding air, respectively [230]. Therefore, in order to describe the pressure discontinuity between the front and back surface of the micro wing, a pair of two overlapping surrounding air nodes per one micro wing node on the micro wing and surrounding air interface are used. The interface conditions are given by Eqs.(4.4) and (4.5) can be written in matrix form as,

$$\mathbf{v}^{a}_{c} = {}_{\tau}\mathbf{T}\mathbf{v}^{w}_{c} \tag{4.17}$$

$$\mathbf{T}\mathbf{Q}^{a}_{c} + \mathbf{Q}^{w}_{c} = \mathbf{g}^{aw}_{c} \tag{4.18}$$

where **Q** = internal force vector including all effects of the surrounding air or the micro wing, T = interpolation matrix, and subscript c represents the coupled DOFs. These equations can be written in the nodal form as,

$$\begin{Bmatrix} {}_{f}v^{a}_{c} \\ {}_{b}v^{a}_{c} \end{Bmatrix} = \begin{bmatrix} 1 \\ 1 \end{bmatrix} v^{w}_{c} \tag{4.19}$$

$$[1\ 1] \begin{Bmatrix} {}_{f}Q^{a}_{c} \\ {}_{b}Q^{a}_{c} \end{Bmatrix} + \mathrm{Q}^{w}_{c} = \mathrm{g}^{aw}_{c} \tag{4.20}$$

where v, Q, and g denote the nodal components of the velocity, and the internal and external force vectors, respectively. The subscripts f and b represent the front and back sides of the micro wing, respectively.

4.3 Computational flight performance of flapping-wing nano air vehicles

In order to evaluate the flight performance, two design solution of the polymer micromachined FWNAV has been considered, the first prototype and its miniaturized version. Miniaturized design of FWANAV has been obtained using iterative design window methodology from the initial FWNAV design, discussed in Chapter 3. Fig. 4.3 shows the plain and cross-sectional views of the detailed design of FWNAV where the length of support frame L_s = 26.9 mm and hinge gap h = 160 μm for the first prototype while L_s =10 mm and h = 280 μm for miniaturized design. In the following sub-section, the flight performance of these FWNAV designs has been estimated using nonlinear structural dynamic analysis of FWNAV and FSI analyses of the micro wing.

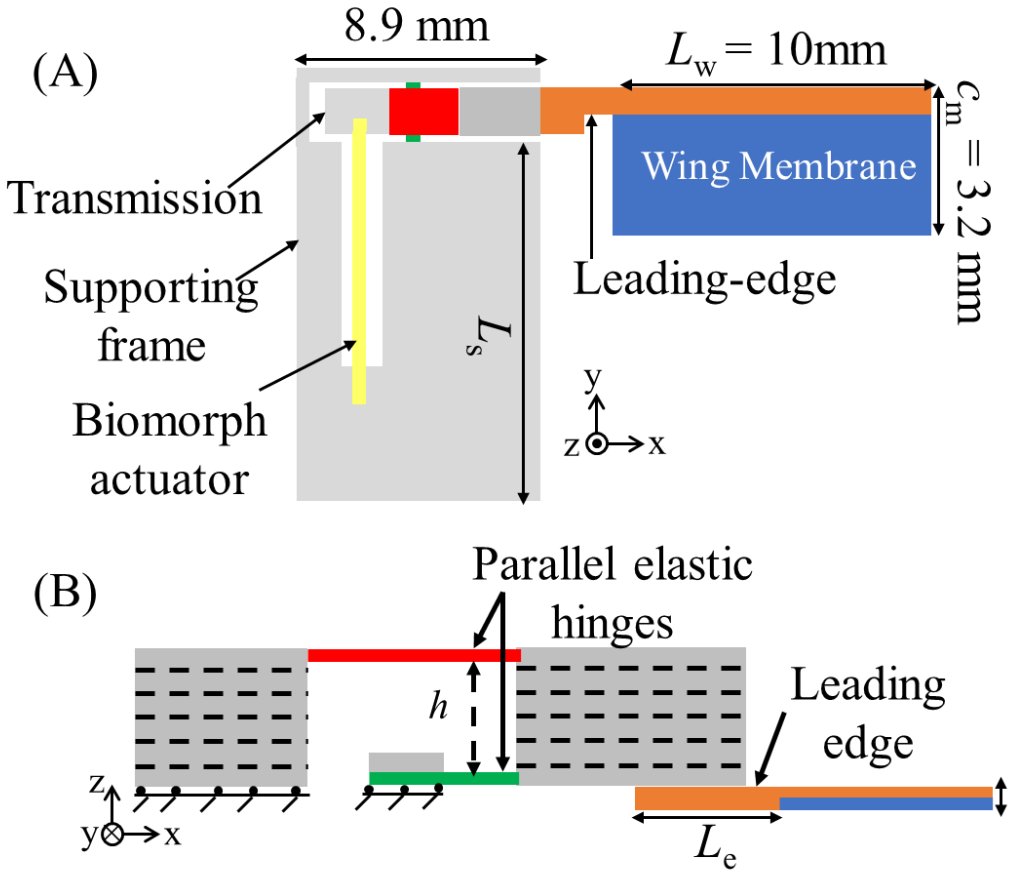

Figure 4.3: Detailed design of flapping wing nano air vehicle (FWNAV) in plain view (A), the cross-sectional view (B)

4.3.1 Nonlinear structural dynamic analysis of the flapping wing nano air vehicles

Fig. 4.4 shows the problem setup for nonlinear structural dynamic analysis of the FWNAVs, and the material property is shown in Table 4.1 while material distribution in FWNAV is shown in Fig. 4.5. The sinusoidal forced vibration $u_x = U_x \times \sin 2\pi f t$ (U_x is the forced vibration amplitude, and f is the flapping frequency) is applied to the transmission's area, where the free end of the bimorph is attached. The evaluation of U_x = 81 μm has been discussed in Chapter 2. The flapping frequency for the first prototype is f = 50 Hz, while for the miniaturized design f = 100 Hz, the reason for selecting this individual f is to avoid the sticking between elastic hinges during flapping motion which have further explained in this sub-section.

The lower part of the supporting frame is fixed in the problem setup where bimorph actuator is attached. In this setup, the finite element mesh for the first

prototype is 19,582 elements and 98,451 nodes while for the miniaturized design is 17,582 elements and 78,451 nodes used. The time increment is $\Delta t = T/4000$, and T is the flapping period and is equal to the inverse of f.

The nonlinear dynamic simulation is conducted using nonlinear finite element transient analysis of MARC solver with 20-node solid hexahedral elements [149], where the following transient finite element discrete equation is solved:

$$\mathbf{Ma} + \mathbf{Cv} + \mathbf{Q(u)} = \mathbf{F}, \tag{4.21}$$

where **M** and **C** are the mass and diffusive matrices, respectively; **Q** is the interior force vector; **a**, **v**, and **u** are the acceleration, velocity, and displacement vectors, respectively; **F** is the external force vector.

Nonlinear structural dynamic analysis results of FWNAVs have been divided into two parts for easy understanding to the readers, the first is flapping performance i.e., stroke angle and flapping velocity, and the second is the hinge gap study during flapping motion.

Firstly, flapping performances of the FWNAVs have been discussed. Fig. 4.6 shows the flapping angular displacement of leading-edge and wing attachment for the first prototype and miniaturized design.

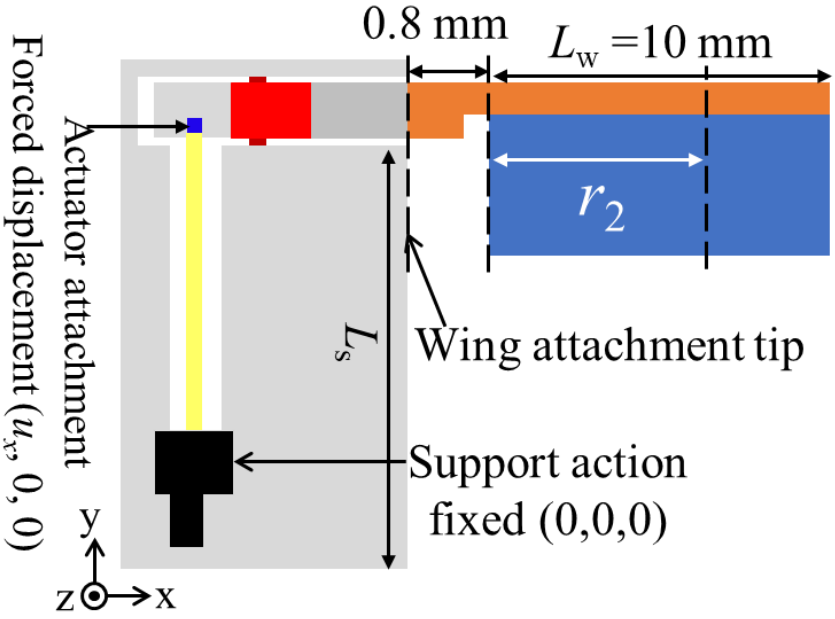

Figure 4.4: Problem setup for nonlinear structural dynamic analysis of FWNAVs

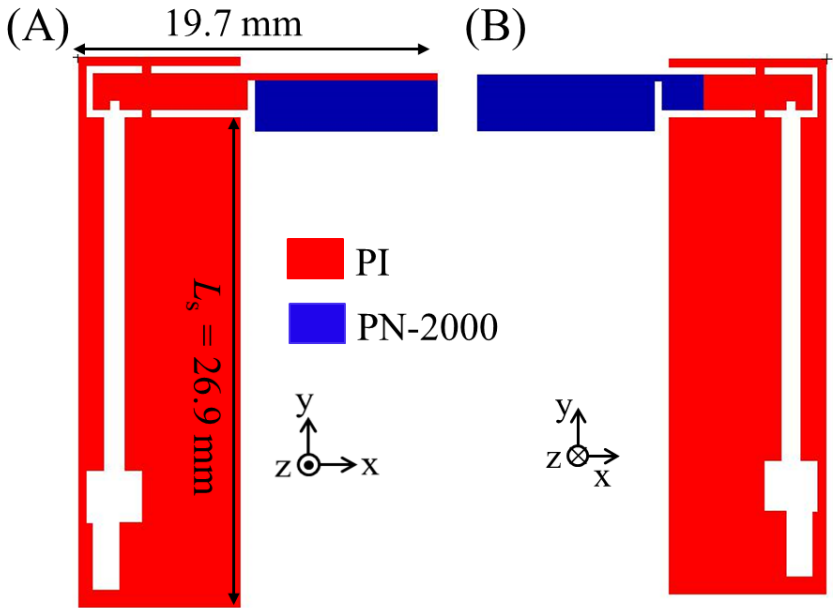

Figure 4.5: Material distribution in FWNAV front side (A), rear side (B), in plain view

Table 4.1: Properties of polyimide (PI) material

Material	Young's modulus	Mass density	Poisson's ratio	Breaking strength
PI*	2.5 GPa	1420 kg/m^3	0.289	109 MPa
PN-2000**	3.5 GPa	1420 kg/m^3	0.30	109 MPa

* Photosensitive polyimide adhesive sheet,** Photosensitive polyimide solution [153]

In the first prototype, the leading-edge stroke angle Φ_L = 43.80° and wing attachment stroke angle Φ_w =35.10° whereas in the miniaturized design Φ_L = 87.02° and Φ_w = 39.25°. Due to the large bending of the leading-edge beam Φ_L is greater than Φ_w as shown in Fig. 4.7 which also demonstrates the location, Φ_L and Φ_w have been evaluated.

Fig. 4.8 shows the time history of the flapping velocity for the first prototype and miniaturized design at the position of r_2 from the wing base, see Fig. 4.4 and the mean flapping velocity for first prototype $U_{m,Dynamic}$ = 0.69 m/sec while for miniaturized design $U_{m,Dynamic}$ = 2.13 m/sec. This $U_{m,Dynamic}$ have been compared with the mean flapping velocity using a quasi-steady formula which is based on sinusoidal flapping motion. The quasi-steady formula for mean flapping velocity U_m [59] can be expressed as,

$$U_m = 2\, r_2\, \Phi\, L_w f, \tag{4.22}$$

where $r_2 = 0.6$ is the dimensionless radius of the second moment of the wing area, Φ is the stroke angles; $\Phi_L = 43.80°$ and $\Phi_w = 35.10°$ for the first prototype while $\Phi_L = 87.02°$ and $\Phi_w = 39.25°$ for miniaturized design, and $L_w = 10$ mm is the spanwise length of the micro wing, $f = 50$ Hz and 100 Hz is the flapping frequency for the first prototype and miniaturized design. Thus, the quasi-steady mean flapping velocity for Φ_L and Φ_w are $U_{m,L} = 0.52$ m/sec and $U_{m,w} = 0.42$ m/sec, respectively for first prototype whereas $U_{m,L} = 2.07$ m/sec and $U_{m,w} = 0.93$ m/sec, respectively for miniaturized design. The reason for the difference between $U_{m,L}$ or $U_{m,w}$ and $U_{m,Dynamic}$ is mainly because $U_{m,L}$ or $U_{m,w}$ assumes sinusoidal flapping motion. The calculated lift force using the time history of flapping velocities and theoretical formula have been discussed in Section 4.3.3.

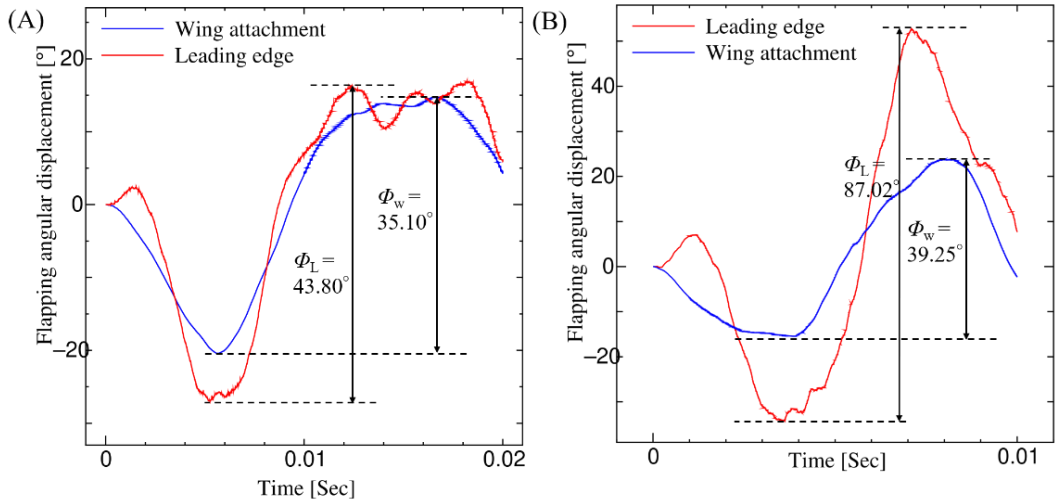

Figure 4.6: Flapping angular displacement of FWNAVs, first prototype (A) miniaturized design (B)

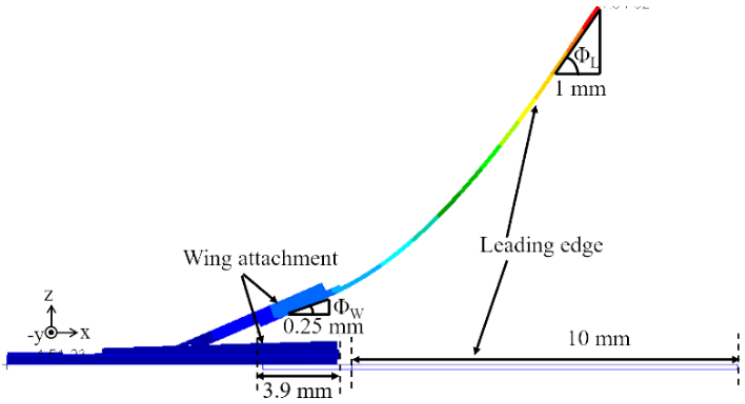

Figure 4.7: Illustration of Φ_L and Φ_w and reason of Φ_L is greater than Φ_w

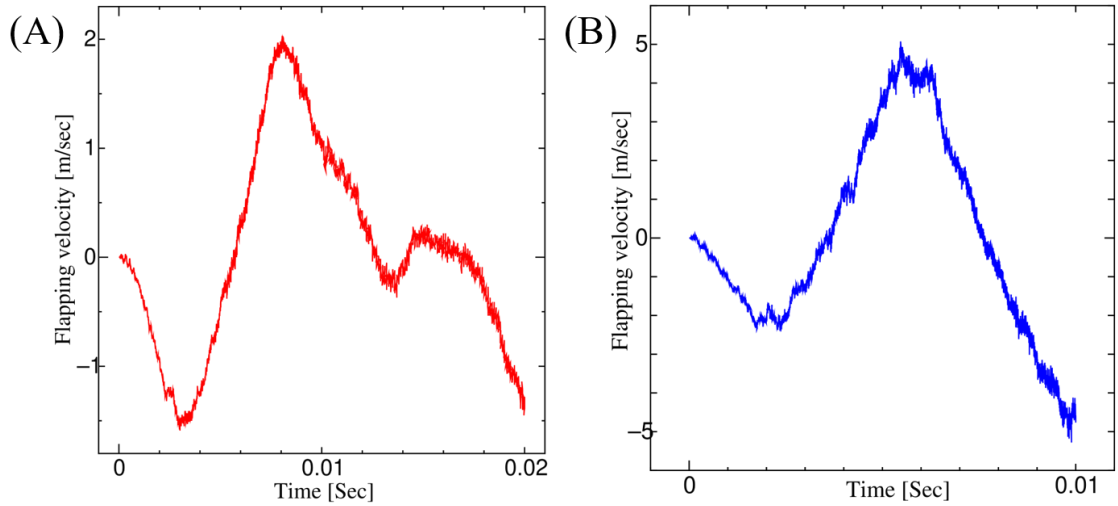

Figure 4.8: Time history of flapping velocity of FWNAVs, first prototype (A) miniaturized design (B)

Secondly, the hinge gap has been studied for the safe working of FWNAVs, it is possible that elastic hinges can stick to each other during flapping, especially in upward flapping motion. Hence, the gap between elastic hinges during upward flapping motion has been studied, see Fig. 4.9 where h = 160 μm and 280 μm for the first prototype and miniaturized design, respectively. Tables 4.2 and 4.3 show the maximum out-of-plane positions at sections A and B of the transmission and the gap between these sections during the upward flapping motion for the first prototype and miniaturized design, respectively. In Fig. 4.8, it can be visual that sections A and B belong to the upper and lower hinges, respectively, and they have the same in-plane position. Tables 4.2 and 4.3 indicate that the gap is positive, and the hinges are not sticking together so FWNAVs will not break during actual working.

Table 4.2: Out-of-plane positions of sections A and B, and their gap for the first prototype

f (Hz)	Z_A	Z_B	Z_A - Z_B	*Sticking*
50 Hz	167.95 μm	92.52 μm	75.43 μm	No

Table 4.3: Out-of-plane positions of sections A and B, and their gap for the miniaturized design

f (Hz)	Z_A	Z_B	Z_A - Z_B	*Sticking*
100 Hz	390.19 μm	291.79 μm	98.40 μm	No

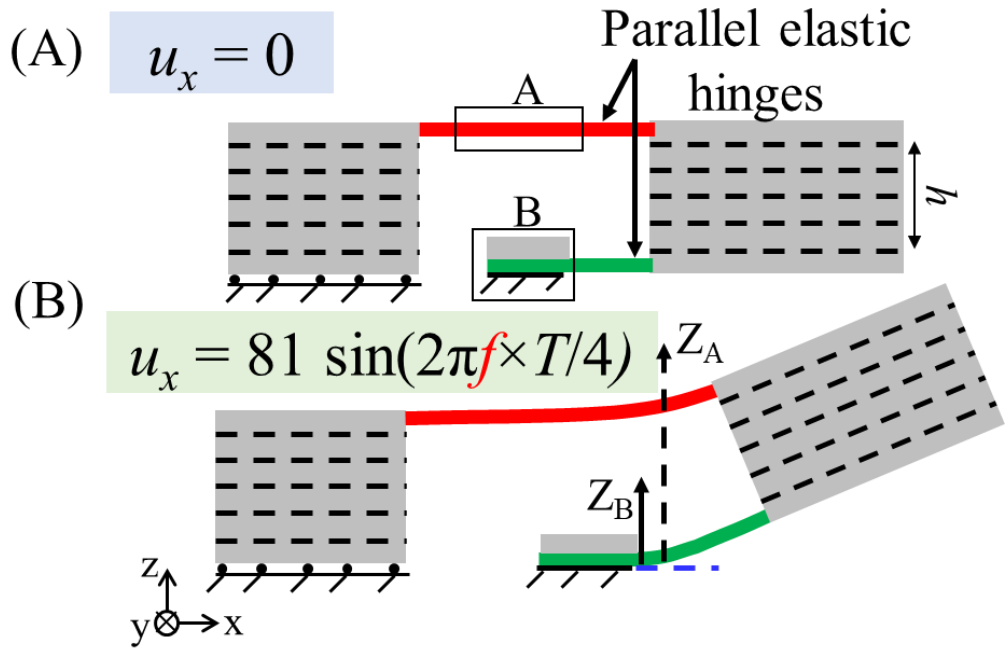

Figure 4.9: A sectional view of the transmission in undeformed condition (A) and deformed condition (B). Z_A and Z_B denote the out-of-plane positions of sections A and B, respectively. Note that h for the first prototype and miniaturized design is h = 160 μm and 280 μm, respectively

4.3.2 Fluid-structure-interaction analysis of the micro wing

Fig. 4.3 shows the detailed design of FWNAV but it does not show the actual design of the micro wing which can be visualized from Fig. 4.10(A). The micro wing is further modified into a rectangular micro wing which is a problem setup for FSI analysis, see Fig. 4.10(B). In this figure, the stroke axis is considered at a position that is similar to the wing attachment tip, see Fig. 4.4, and the MITC shell element is used for the micro wing during the FSI analysis (number of nodes: 143, number of elements: 120) as discussed in Section 4.2. Material properties of the micro wing are given in Table 4.1. However, the leading-edge consists of two polyimide materials (PI and PN-2000) so its equivalent modulus of elasticity is 2.62 GPa.

In FSI problem setup Fig. 4.10(B), sinusoidal angular displacement $\Phi = \Phi_0 \sin 2\pi f t$ has been applied in the flapping motion direction where angular amplitude Φ_0 is equal to the stroke angles Φ_L or Φ_w and f is the flapping frequency, these angular motion parameters are given by the nonlinear structural dynamic

analysis of FWNAVs as discussed in the Section 4.3.1. The stroke angles and flapping frequency for first prototype are $\Phi_L = 43.80°$, $\Phi_w = 35.10°$ and $f = 50$ Hz, respectively whereas for miniaturized design are $\Phi_L = 87.02°$, $\Phi_w = 39.25°$ and $f = 100$ Hz, respectively. The time increment is $\Delta t = T/5000$, and T is the flapping period which is equal to the inverse of f.

Fig. 4.11(A) shows the rectangular fluid tank for FSI analysis and the no-slip condition is imposed on all boundaries on the wall. As discussed in Section 4.2, stabilized linear equal-order-interpolation velocity-pressure elements are used for the fluid mesh, see Fig. 4.11(B) which shows the fluid mesh in 3-Dimension, and Fig. 4.11(C) shows the fluid and micro wing mesh in plain view or xy-plane.

In fluid mesh, the number of nodes is 50460, and the number of elements is 271922. Fluid (air) properties are as follows; mass density $\rho^a = 1205$ kg/m^3 and viscosity $\mu^a = 1{,}837\text{e-}05$ kg/m-sec. FSI analysis has been carried out using the in-house code which is already validated [46, 59] and as described in Section 4.2, parallel computation is executed in a multiple-core processor (10-core Xeon 2.8 GHz × 2 CPUs, 32 GB memory) [46].

Fig. 4.12 shows the FSI analysis result, time history of numerical lift force for the first prototype, and miniaturized design angular motion condition i.e., Φ_L, Φ_w, and f. The mean lift coefficient can be evaluated using a quasi-steady formula under the assumption of sinusoidal flapping motion [74],

$$F_L = 0.5\, \rho^f C_L S\, U_m^2, \tag{4.23}$$

where $\rho^f = 1.205$ kg/m^3 is the fluid mass density, S is the wing's area, which is defined as $S = L_w\, c_w$, where $L_w = 10$mm is the wingspan length, $c_w = 3.2$ mm is the chordwise length of the micro wing, and U_m is the mean flapping velocity given by Eq.(4.22) which is equal to $U_{m,L}$ or $U_{m,w}$ as discussed in Section 4.3.1, and C_L is the mean lift coefficient.

Note that mean lift force from time history is calculated for the cycle which is bounded by a rectangular dash line in Fig. 4.12. Since there are two mean lift forces (two-time history of lift force due to Φ_L and Φ_w), see Fig. 4.12(A) and two mean flapping velocities $U_{m,L}$, $U_{m,w}$ due to Φ_L and Φ_w, respectively for the first prototype as explained above so, there would be two mean lift coefficients as follows, mean lift coefficient due to Φ_w, is $C_{L,w} = 0.72$ and mean lift coefficient due to Φ_L, is $C_{L,L} = 0.79$.

Similarly, the mean lift coefficient for miniaturized design due to Φ_w only is

$C_{L,w} = 2.40$. The reason for mean lift coefficient $C_{L,w}$ only in miniaturized design is that it was found based on the detailed observation that wing membrane thickness is not enough (production of a large feathering angle of about 65° and low lift coefficient of 0.50) with a large stroke angle such as $\Phi_L = 87.02°$ and high flapping frequency like $f = 100$ Hz. Due to this reason, wing membrane thickness has been designed and discussed in Section 4.4.

These mean lift coefficients will be further used to calculate lift force for nonlinear structural dynamic analysis in Section 4.3.3.

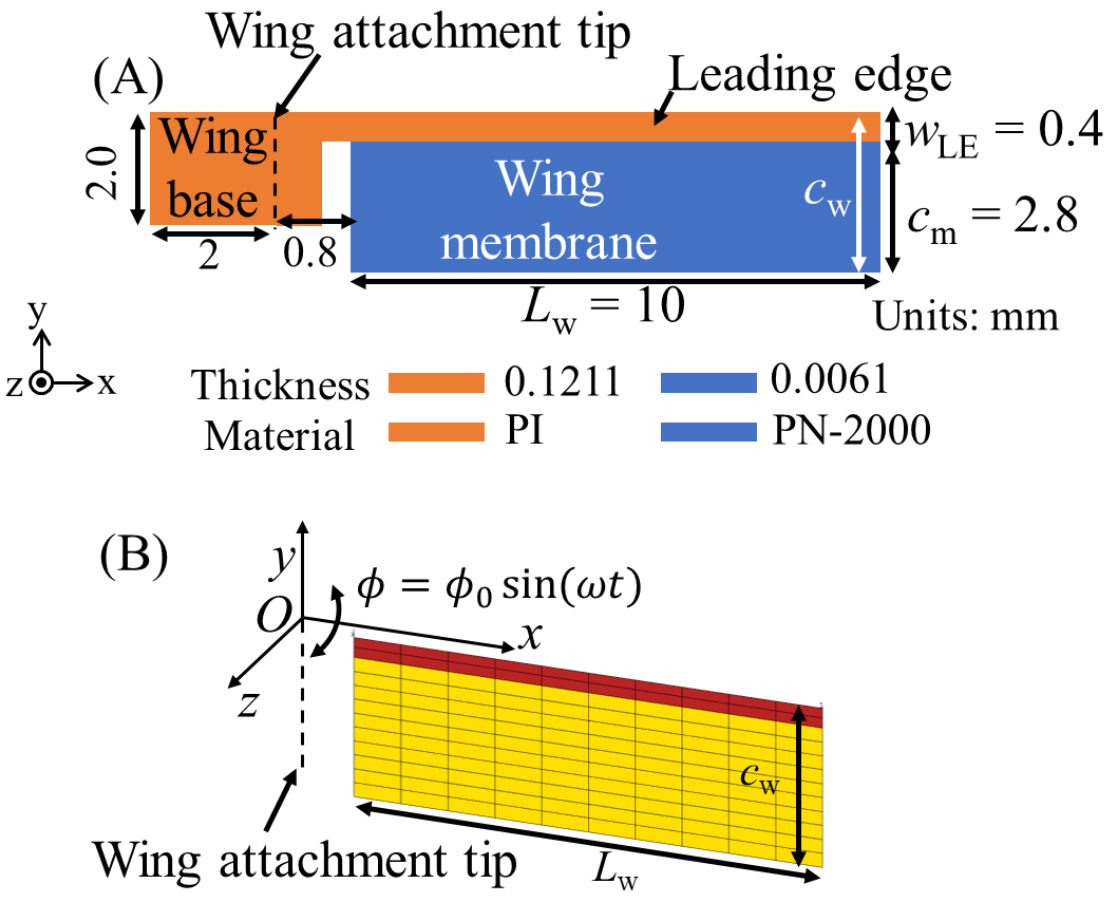

Figure 4.10: Detailed design of micro wing (A), Problem setup for FSI analysis of micro wing with mesh (B)

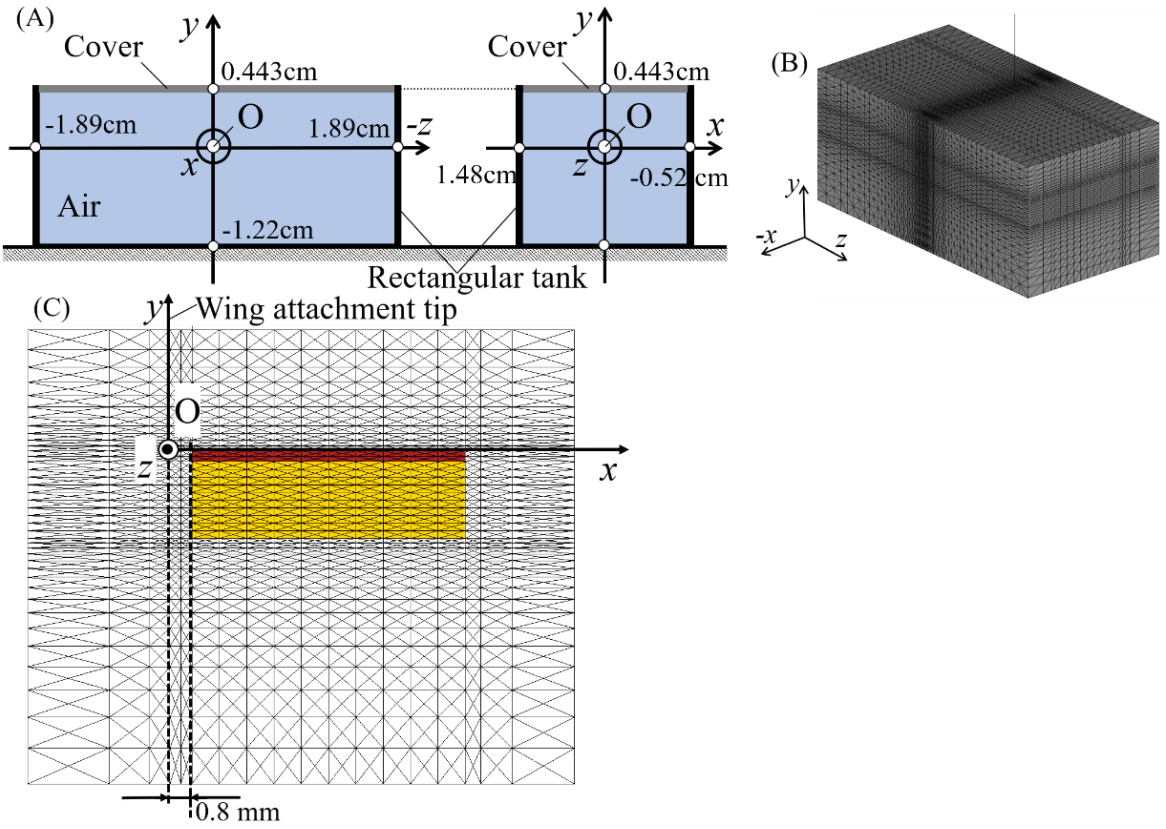

Figure 4.11: The geometry of the rectangular air tank 3.78 × 1.66 × 2 cm^3 (A), employed mesh for fluid in 3-dimensional view (B), fluid and micro wing mesh for FSI analysis in *xy*-plain (C)

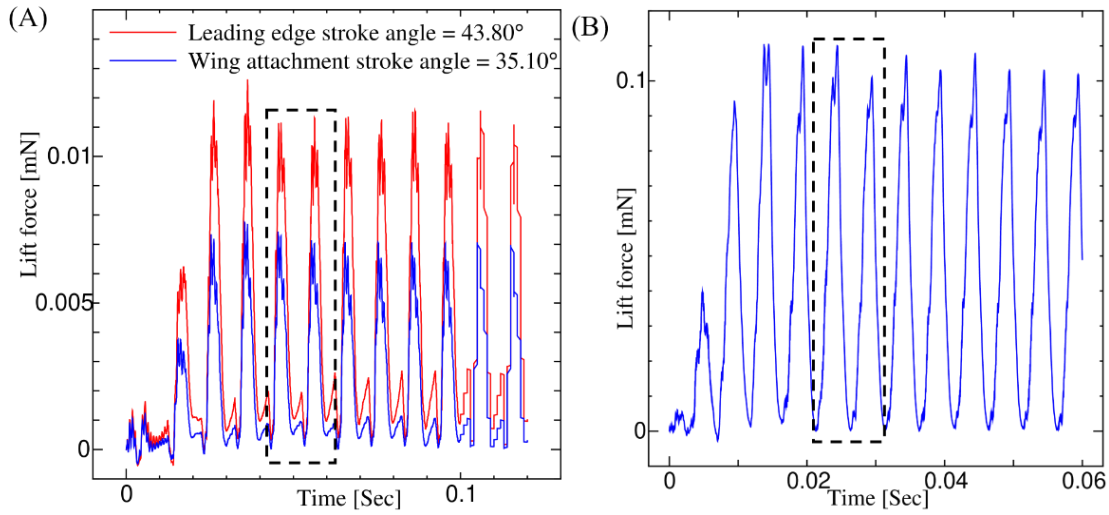

Figure 4.12: Numerical lift force using FSI analysis for angular deformation parameter of the first prototype (A) Miniaturized design (B). Note that mean lift force is calculated for a cycle bounded by a rectangular dash line

4.3.3 Flight performance comparison between structural dynamic and fluid-structure interaction analyses

In this sub-section, flight performance has been compared between the results from nonlinear structural dynamic Section 4.3.1 and FSI analyses Section 4.3.2.

Firstly, the feathering angle is compared between both analyses. Fig. 4.13 shows the feathering angle time history from a nonlinear structural dynamic analysis of the first prototype and miniaturized design, its mean values are $\bar{\theta}_{\text{Dynamic}} = 9.84°$ and $\bar{\theta}_{\text{Dynamic}} = 23.92°$, respectively for the first prototype and miniaturized design.

Fig. 4.14 shows the time histories of the feathering angles from FSI analysis for the first prototype, and miniaturized design angular motion conditions i.e., Φ_L, Φ_w, and f. For the first prototype, the mean feathering angle due to Φ_L and Φ_w is $\bar{\theta}_L = 7.47°$, and $\bar{\theta}_w = 5.32°$, respectively while for the miniaturized design, the mean feathering angle due to Φ_w only is $\bar{\theta}_w = 23.10°$.

These mean feathering angle has been tabulated in Table 4.3 for easy understanding for the reader. in Table 4.3, since $\bar{\theta}_L$ or $\bar{\theta}_w$ is almost similar to the $\bar{\theta}_{\text{Dynamic}}$ so it can be concluded that FSI analysis with a micro wing is sufficient over the FSI analysis of FWNAV to predict the flight simulation and performance and at the same time reduce computational cost and complexity associated with the latter.

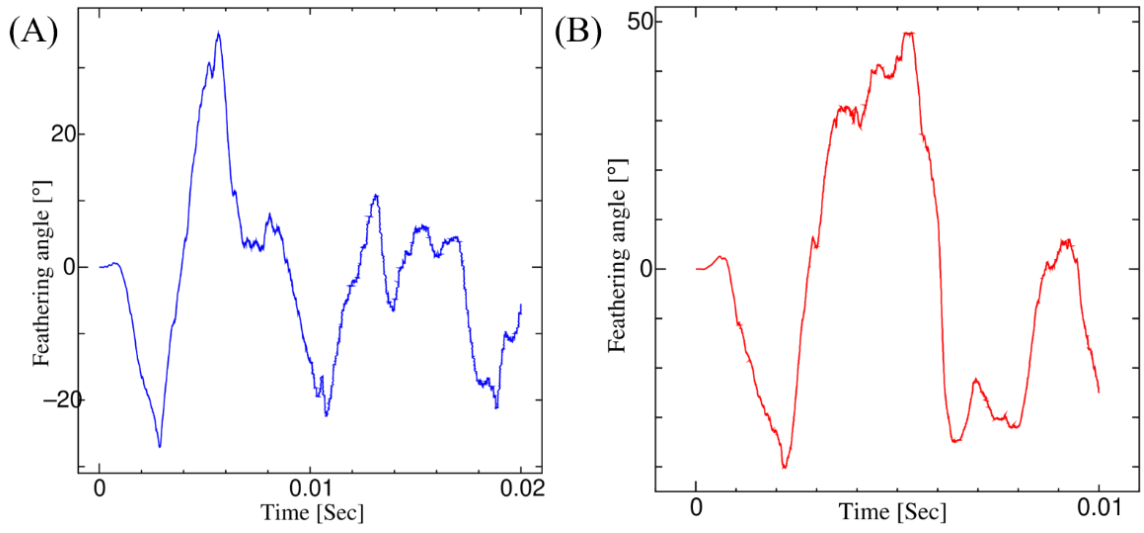

Figure 4.13: Feathering angle from nonlinear structural dynamic analysis of FWNAVs, first prototype (A) miniaturized design (B)

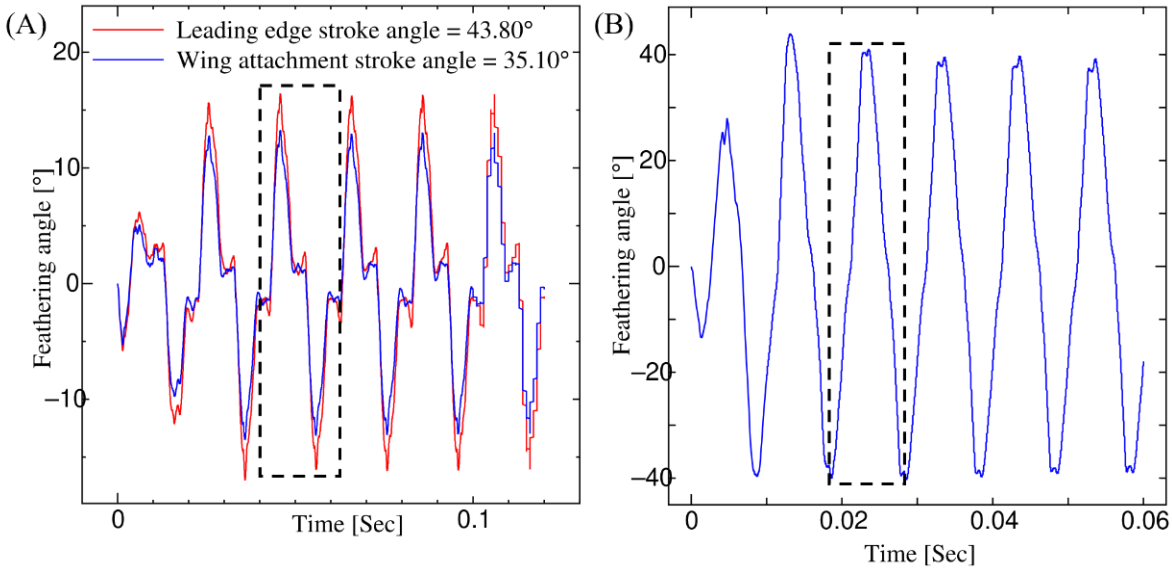

Figure 4.14: Feathering angle from FSI analysis with a micro wing for first prototype (A) miniaturized design (B) angular deformation parameters i.e., $\bar{\theta}_L$ or $\bar{\theta}_w$ and f. Note that the average feathering angle in FSI analysis is calculated for a cycle bounded by a rectangular dash line

Table 4.4: Mean feathering angle from FSI analysis with input angular deformation parameter of nonlinear structural dynamic analysis of FWNAVs; first prototype and miniaturized design

Angular deformation parameter of FWNAVs	Dynamic analysis, $\bar{\theta}_{Dynamic}$	FSI Analysis	
		$\bar{\theta}_w$ due to Φ_w	$\bar{\theta}_L$ due to Φ_L
First prototype	9.84°	5.32°	7.47°
Miniaturized design	23.92°	23.10°	

Next, lift force has been compared between both analyses.

Lift force from FSI for input angular deformation parameter of the first prototype and miniaturized design have been already discussed in the previous sub-section, see Fig. 4.12, from this figure one can estimate the mean lift force due to Φ_L and Φ_w, $F_{L,L} = 0.0041$ mN and $F_{L,w} = 0.0025$ mN, respectively for input angular deformation parameter of the first prototype whereas mean lift force due to Φ_w is $F_{L,w} = 0.04$ mN for input angular deformation parameter of miniaturized design.

Lift force from nonlinear structural dynamic analysis of the first prototype and miniaturized design has been evaluated using Eq.(4.23) where flapping velocity is given by Fig. 4.8 and lift coefficient $C_{L,w}$, and $C_{L,L}$ from the previous sub-

section. Fig. 4.15 shows the time histories of calculated lift force from structural dynamic analysis of the first prototype and miniaturized design with lift coefficients $C_{L,w}$ and $C_{L,L}$.

Hence, the mean lift force for structural dynamic analysis of the first prototype is $F^{w}_{L,Dynamic}$ = 0.019 mN and $F^{L}_{L,Dynamic}$ = 0.021 mN due to $C_{L,w}$ and $C_{L,L}$, respectively whereas the mean lift force for structural dynamic analysis of the miniaturized design is $F^{w}_{L,Dynamic}$ = 0.29 due to $C_{L,w}$. The cause of the difference between mean lift forces from nonlinear structural dynamic and FSI analyses are mainly, differences in flapping velocity which has been explained in Section 4.2.1.

However, the mean lift force from both analyses is less than the weight of the miniaturized FWNAV based on the optimized bimorph actuator dimension as given in Table 4.5, lift force has been optimized to support the weight of FWNAVs explained in Section 4.4.

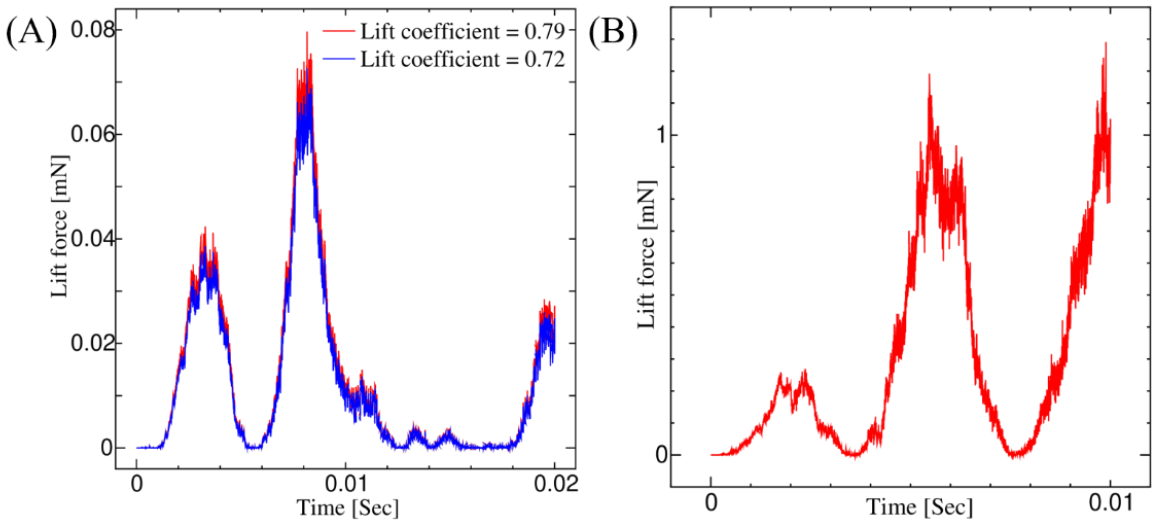

Figure 4.15: Evaluated lift force from theoretical formula and nonlinear structural dynamic analysis of FWNAVs, first prototype (A) miniaturized design (B)

4.4 Optimization of flight performance using fluid-structure interaction analysis

In Section 4.3.2 it was found that a large feathering angle of about 65° and a low lift coefficient of about 0.5 is produced due to a large stroke angle $\Phi = 87°$ and a high flapping frequency $f = 100$ Hz with a membrane thickness of 6.1 μm, designed in Chapter 3. Due to the low lift coefficient, the mean lift force gets reduced so the main theme of this section is to design wing membrane thickness for large stroke angle and high flapping frequency which is very necessary to produce high lift force and support the total weight of FWNAV, Table 4.5.

4.4.1 Basic problem setup for optimization of flight performance

In order to optimize the flight performance by maximizing the lift force to support the weight of FWNAVs Table 4.5, FSI parametric study has been conducted. Figs. 4.12 and 4.13 show the basic problem setup for parametric study over FSI analysis where a fixed flapping frequency $f = 100$ Hz is selected based on the design window search results in Chapter 3, and stroke angles are selected as $\Phi = 75°$, 85°, and 95° based on stroke angle $\Phi_L = 87.02°$ obtained from nonlinear structural dynamic analysis of miniaturized FWNAV design in see Section 4.3.1, and range of wing membrane thickness t_w from 8–10 μm is chosen based on the detailed observation of FSI analysis.

4.4.2 Design of wing membrane thickness for maximizing lift force

We know that lift force increases with the increase of stroke angle and flapping frequency and lift force will be maximum when the amplitude of the feathering angle will be about 45°. Hence, in this sub-section t_w has been designed based on the problem set up in the previous section, and amplitude of feathering angle and mean lift force as an output performance characteristic has been considered.

Fig. 4.16(A) shows the amplitude of the feathering angle against t_w for various stroke angles and fixed flapping frequency as mentioned above, this figure is used to find t_w for which the amplitude of maximum feathering angle is about 45° so that lift coefficient would maximum and consequently lift force would be high.

Fig. 4.16(B) shows mean lift force against t_w for three different stroke angles and $f = 100$ Hz as mentioned above. Figs. 4.16(A) and 4.26(B) indicates that the amplitude of the feathering angle at $t_w = 10$ μm is about 45° and the mean lift

force is comparable to the weight of FWNAV, Table 4.5.

Table 4.5: Components of FWNAV and their weight in the miniaturized design based on the optimized weight of actuator

Components of FWNAV	Mass (mg)
Transmission with support frame	33.26
Micro wing	1.88
Bimorph actuator	20
Total mass	55.14

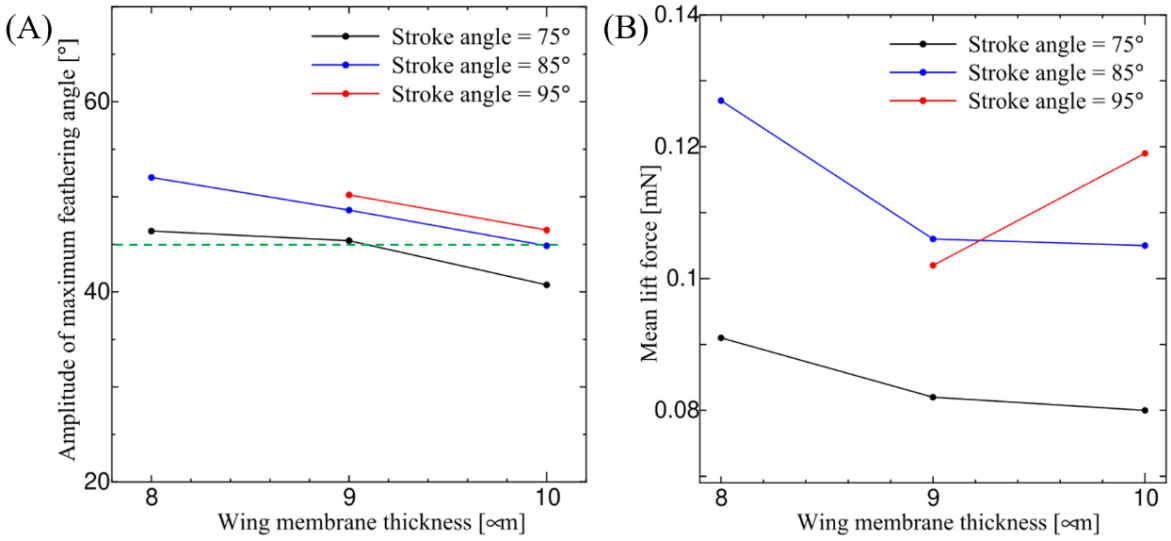

Figure 4.16: Optimization of flight performance, feathering angle (A) mean lift force (B). Note that horizontal green dash line figure (A) indicate the 45° feathering angle

4.5 Conclusion

In this chapter, I have demonstrated the flight simulation and performance of polymer micromachined FWNAVs using two distinguish computational methods. In the computational method, nonlinear structural dynamic analysis has been conducted with FWNAV design whereas FSI analyses have been processed with only micro wing design, to avoid the computational complexity and reduce the computational cost associated with the FSI analysis of FWNAV. However, it was observed that the FSI analysis result with a micro wing is almost similar to the nonlinear dynamic analysis result of FWNAV, and using this one can conclude that the above-mentioned statement is correct.

Here, flight performance has been evaluated for two different designs of FWNAV, the first prototype, and the miniaturized design. The flight performance of the first prototype has shown a small mean feathering angle and low mean lift force because of the small stroke angle and low flapping frequency. Flight performance of miniaturized design indicates good feathering angle and mean lift force is about 10 times that of the first prototype.

Wing membrane thickness has also been designed for large stroke angles and high flapping frequency and it was found that the membrane thickness of 10μm would be preferable. Optimization of flight performance indicates that mean lift force is comparable to the weight of polymer micromachined FWNAV.

Thus, this study shows promising results for miniaturization as well as good flight performance.

CHAPTER 5

DEVELOPMENT OF FLAPPING-WING NANO AIR VEHICLE

5.1 Introduction

In Chapter 3, I have designed the two FWNAVs: the first prototype and the miniaturized version (10mm FWNAV) using an iterative design window search methodology. These FWNAVs produce large stroke angles of about 90° similar to model insects and have enough fatigue life while flapping at frequency f = 100Hz

In Chapter 4, I have evaluated the computational flight performance of FWNAVs using the FSI method which shows that 10mm FWNAV can be able to lift off.

In this chapter, the development of FWNAVs has been discussed using advanced engineering technologies such as microelectromechanical systems (MEMS) technologies. Since the proposed FWNAVs are a complete 2.5-dimensional structure so they can be easily fabricated using polymer micromachining without any post assembly. Micromachining is widely used for developing micro and nano-structure because of the cost reduction and easiness of replicating the structure. Polymer provides the flexibility and softness to the structure which makes it compatible with more standard microfabrication techniques, i.e. photolithography and wet/dry etches [231]

In order to develop FWNAVs, the feasibility of polymer micromachining has been demonstrated by fabricating the transmission with a support frame. Since the transmission is a key and central component of FWNAVs. Fig. 5.1 shows the plain and cross-sectional views of the detailed design of FWNAVs where the length of support frame L_s = 26.9 mm and hinge gap h = 160 μm for the first prototype while L_s =10 mm and h = 280 μm for miniaturized design (10mm FWNAV).

In the next sections, the development of transmission with a support frame of the first prototype using standard microfabrication techniques including the etching, photolithography, deposition, and curing has been discussed as a

demonstration of the feasibility of the fabrication method along with the performance of the fabricate transmission using a static driving test [9].

5.2 Transmission fabrication using polymer micromachining

5.2.1 Fabrication steps of the transmission and the supporting frame

Fig. 5.2 shows the detailed microfabrication steps of the transmission and the supporting frame using photosensitive PI adhesive sheets with a thickness of 40 μm (Toray Industries, Inc.) [153]. This polymer was selected because of its good mechanical, chemical, and thermal properties. It has a modulus of elasticity of 2.5 GPa, a breaking strength of 109 MPa, and an elongation without breaking of 9%. As shown in Figs. 5.2, the process of lamination, exposure, and development of the photosensitive PI adhesive sheet (precursor) over the silicon wafer with the Cu sacrifice layer (thickness of approximately 1.5 μm) are repeated. After the required repetition of this process, the transmission and the supporting frame are cured to imidize the precursor and convert it to polyimide. Finally, the transmission and the supporting frame are released from the substrate.

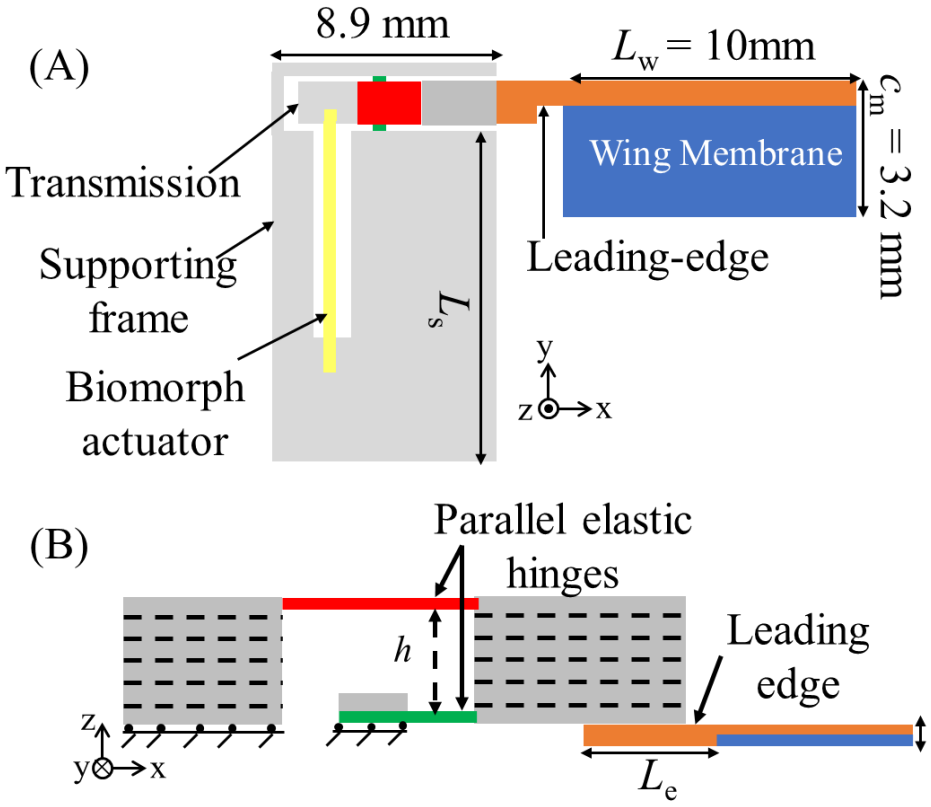

Figure 5.1: Detailed design of flapping wing nano air vehicle (FWNAV) in plain view (A), the cross-sectional view (B)

5.2.2 Fabrication results

The fabricated transmission with the supporting frame using the polymer micromachining process and the photosensitive PI adhesive sheets with a thickness of 40 μm is shown in Figs. 5.3. The proposed transmission was fabricated using the fabrication method described above based on the standard microfabrication technique without any post-assembly. Therefore, it is suitable for the further miniaturization of FWNAVs. The mass of this fabricated transmission is about 76.3 mg, which is evaluated by the structural volume and the mass density of PI material.

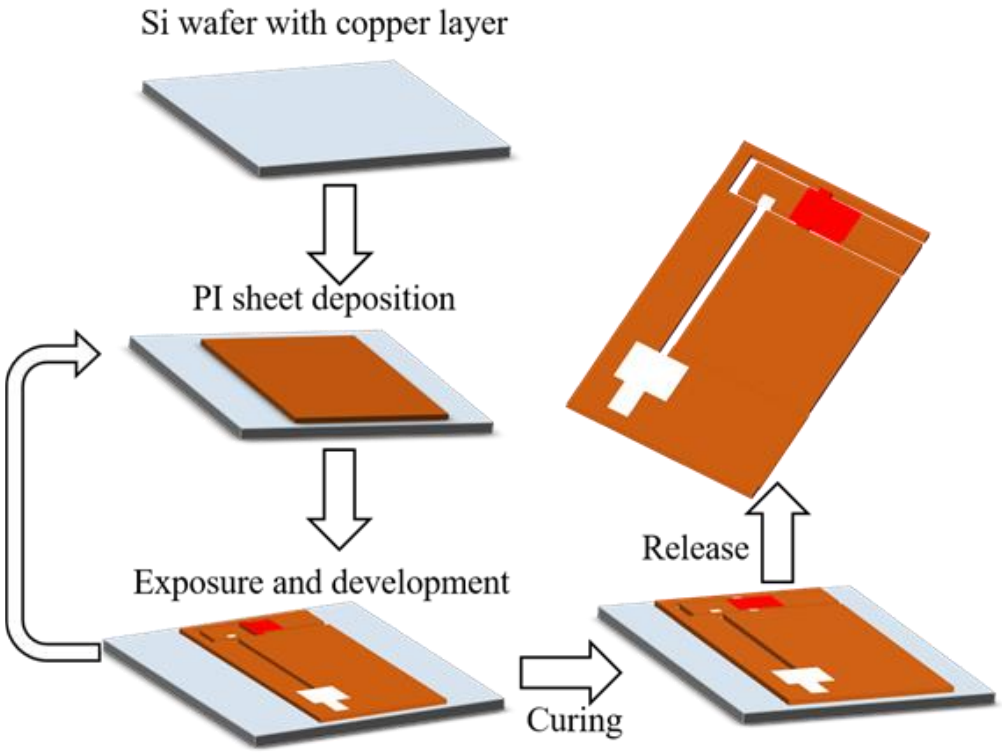

Figure 5.2: Fabrication process consisting of the standard microfabrication steps: (a) deposition, (b) etching, (c) photolithography, (d) curing, and (e) release

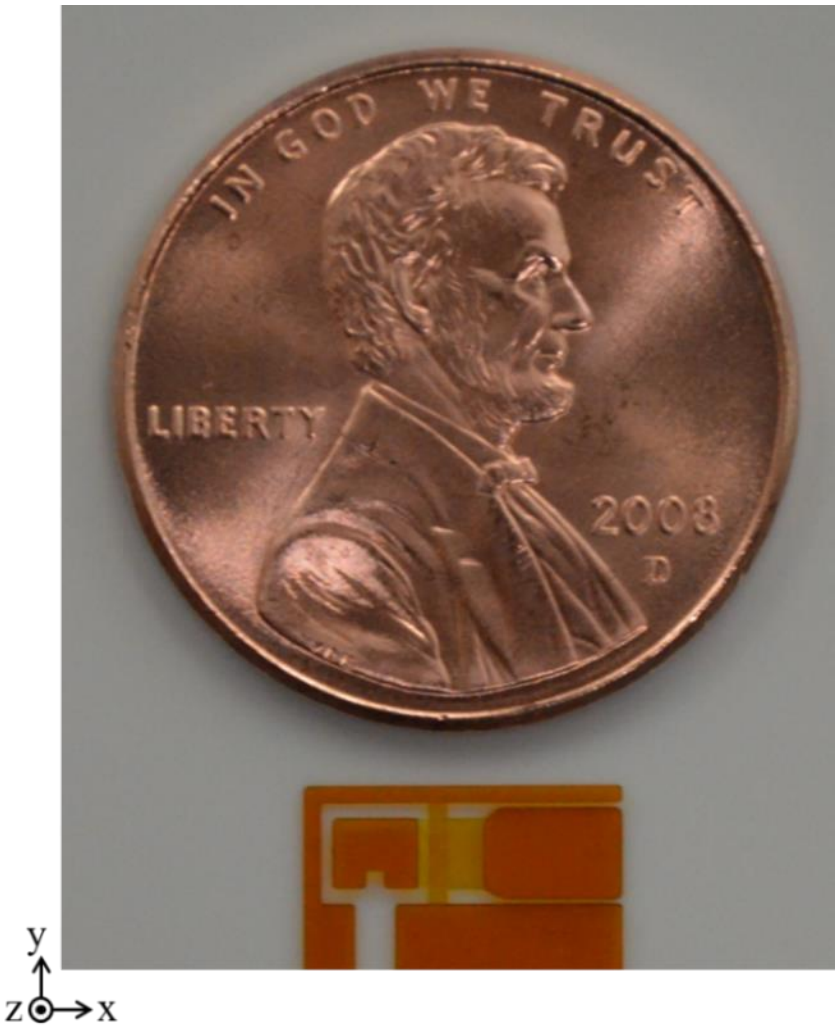

Figure 5.3: Polymer micromachined transmission and supporting frame fabricated using photosensitive polyimide sheets

5.2.3 Fabrication constraint to the gap between the elastic hinges

As shown in Fig. 5.4(A), when two PI sheets (total thickness of approximately 80 μm) were used to create the gap between the elastic hinges, the upper and lower elastic hinges stuck together due to the bending of the upper elastic hinge and less gap width during the development process. In contrast, as shown in Fig. 5.4(B), this problem rarely occurred when four PI sheets (total thickness of approximately 160 μm) were used to create the gap between the elastic hinges. Therefore, at least four PI sheets should be used for the gap between the elastic hinges to avoid the sticking of hinges during the fabrication.

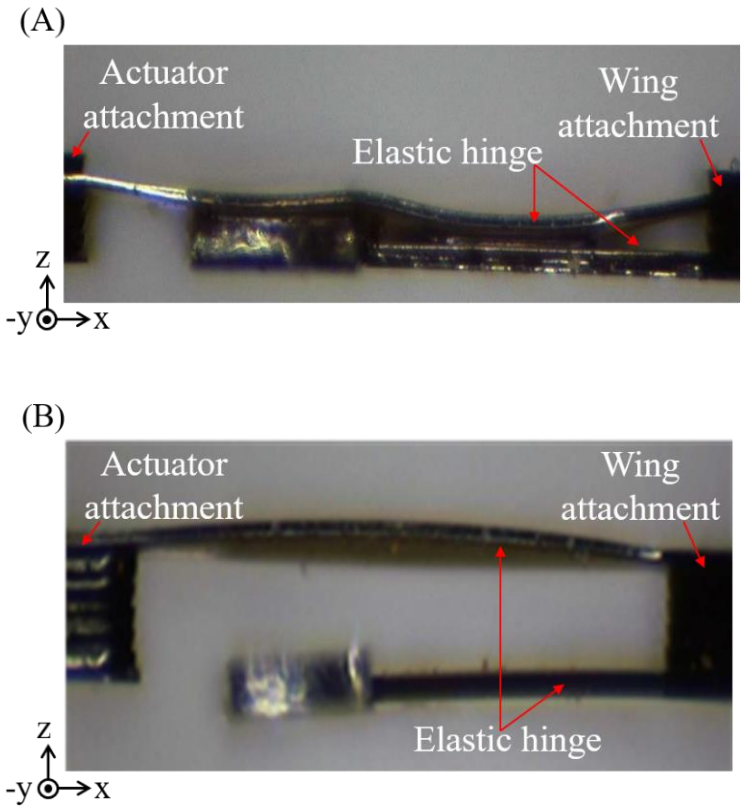

Figure 5.4: (A) Upper and lower elastic hinges stuck together when two PI sheets were used to create the gap between the elastic hinges (B) The Upper and lower elastic hinges did not stick together when four PI sheets were used to create the gap between the elastic hinges

5.3 Evaluation of fabricated transmission

5.3.1 Precision of the fabricated transmission

The precision of the fabricated transmission was studied and is presented here. Each dimension of the fabricated transmission was measured using a micrometer and compared with the design dimension. Fig. 5.5 shows the measured dimensions: the in-plane horizontal and vertical dimensions A and B, the total thickness C, and the elastic hinge thickness D.

Three samples were fabricated, and the dimensions and errors for each sample are given in Table 5.1. In the actual fabrication, a PI precursor liquid was spin-coated as a coupling agent, and its thickness was designed as 7.3 μm. Therefore, this thickness was included in the design dimension C in this table. As demonstrated by the results in Table 5.1, the in-plane precision was

approximately 94% or more, and the total thickness precision was approximately 87% or more. In contrast, it is clear from Table 5.1 that the elastic hinge thickness precision was approximately 60%. The overall precision order was approximately 75%.

The precision of the measurement was determined by approximately one pixel at the edge of the shape, which is approximately 6 μm in Fig. 5.6. The effect of the precision on the performance is discussed in Section 5.4.2.

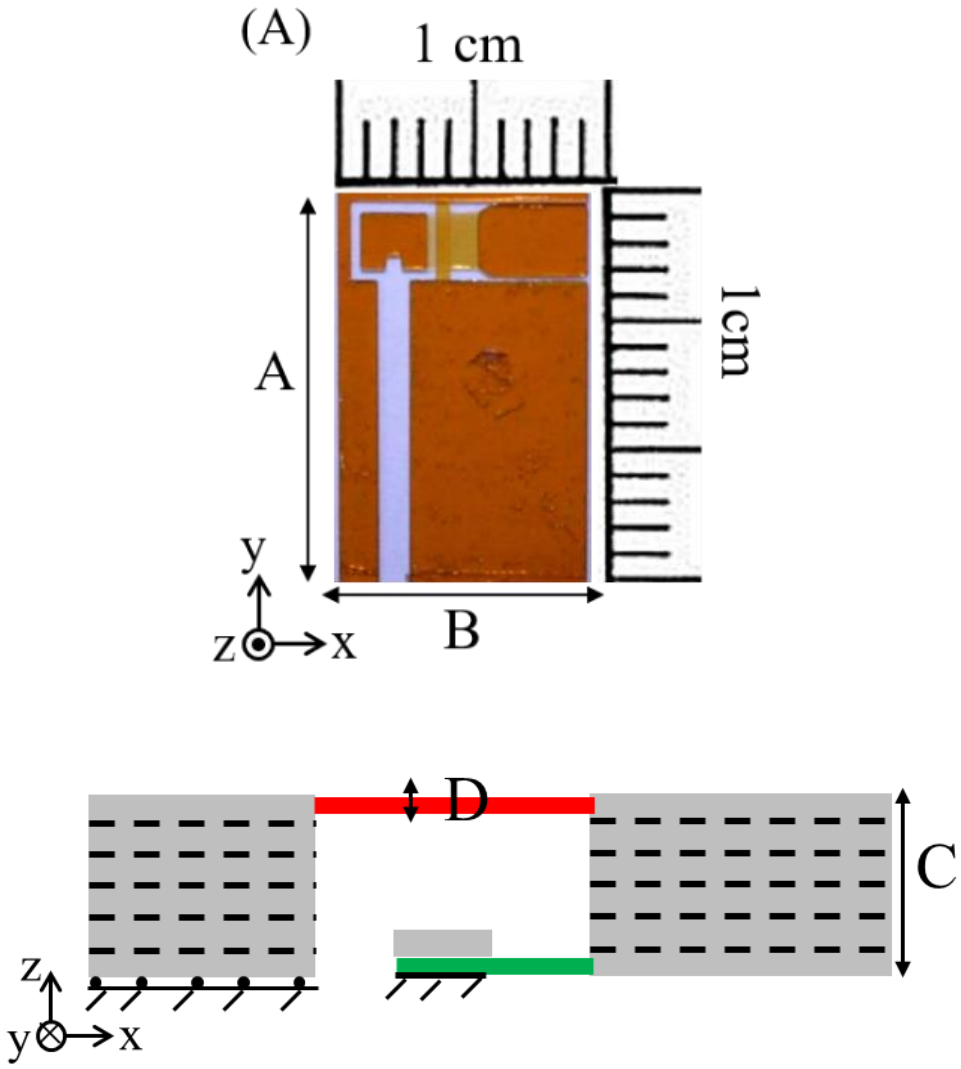

Figure 5.5: (A) Observation of the precision of the in-plane dimension (B) total thickness and elastic hinge thickness of the fabricated transmission

Table 5.1: Dimension measurements and precisions for the fabricated transmission. The dimensions of A, B, C, and D in Fig. 5.5 were measured and compared with the design dimensions

Dimension	Sample 1		Sample 2		Sample 3		Design
	Observed	Precision	Observed	Precision	Observed	Precision	
A	8,621μm	96.87%	8,612μm	96.76%	8,705 μm	97.81%	8,900μm
B	14,865 μm	99.1%	14,213μm	94.75%	14,065 μm	93.77%	15,000 μm
C	215 μm	86.94%	222 μm	89.77%	220 μm	88.96%	247.3 μm
D	24.63 μm	61.57%	27.76 μm	69.39%	27.78 μm	69.45%	40 μm

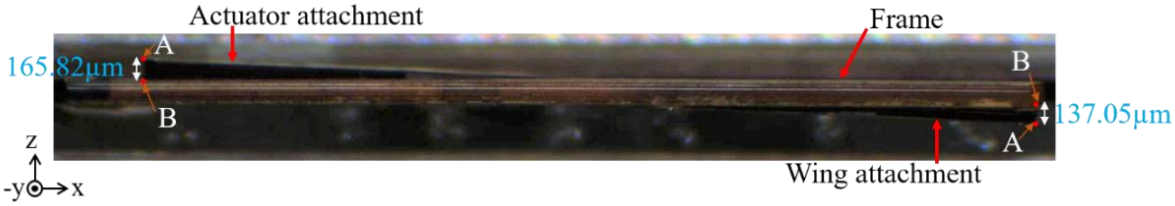

Figure 5.6: *xz* plane view of the fabricated transmission and frame, along with the out-of-plane deviation of the initial structural shape

5.3.2 Initial shape distortion of the fabricated transmission

The fabricated transmission has some deviations from the design shape. Fig. 5.6 shows the *xz* plane view of the fabricated transmission and frame. As shown in this figure, the actuator and wing attachment parts are not quite in the same plane as the frame (*xy* plane). This means that these parts are slightly distorted around the hinge-supporting beam (around the *y*-axis).

Three samples were fabricated, and their initial distortions are given in Table 5.2, where the initial distortion is defined as the distance between the corner of the actuator or wing attachment part and the frame in the *z*-direction (the distance between points A and B along the *z*-direction in Fig. 5.6) with no load. As shown in Table 5.2, the average initial distortion of the actuator and wing attachment parts was approximately 175 μm whose effect on the performance is trivial.

Table 5.2: Initial distortion of the fabricated structural shape

Chip No.	Actuator attachment part initial distortion	Wing attachment part initial distortion
Sample 1	104.61μm	153.86μm
Sample 2	253.90μm	236.99μm
Sample 3	165.82μm	137.05μm

5.4 Performance of fabricated transmission

5.4.1 Evaluation of transmission performance using the static driving test

The static performance of the transmission was evaluated by comparing numerical results obtained by finite element analysis and experimental results. Fig. 5.7 shows a schematic of the experimental apparatus for the static driving test while Fig. 5.8 shows the actual experimental setup. During the static driving test, a forced displacement u_x ranging from 0 to 100 μm in intervals of 10 μm was applied in the x-direction via a microneedle. When the microneedle pushes (pulls) the actuator attachment part to give a positive (negative) u_x, the wing attachment part produces a downward (upward) flapping motion, or a counterclockwise (clockwise) rotation around the y-axis.

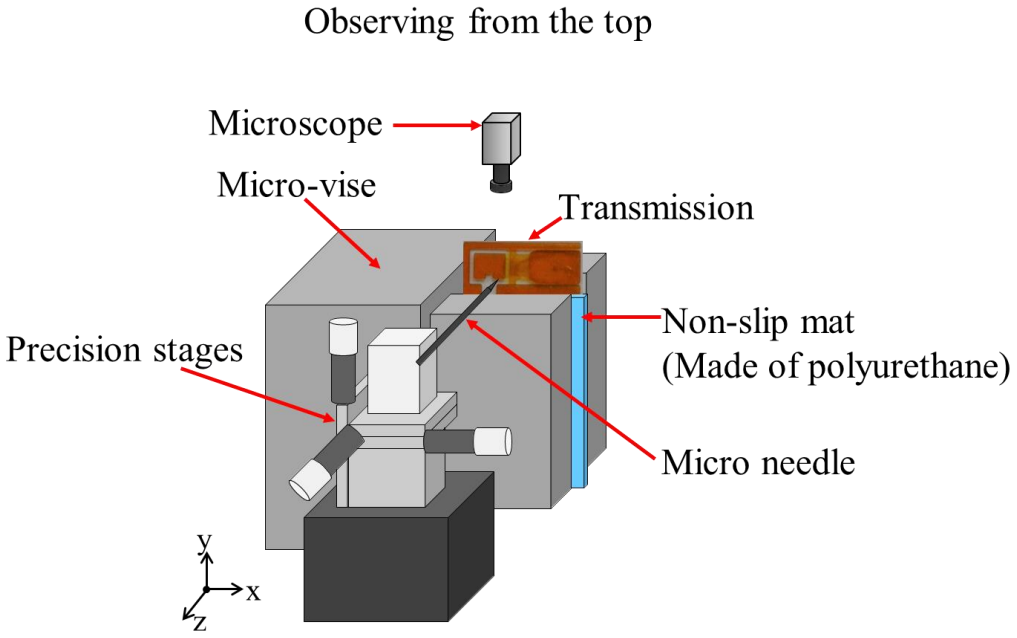

Figure 5.7: Schematic diagram of experimental apparatus for the static driving test

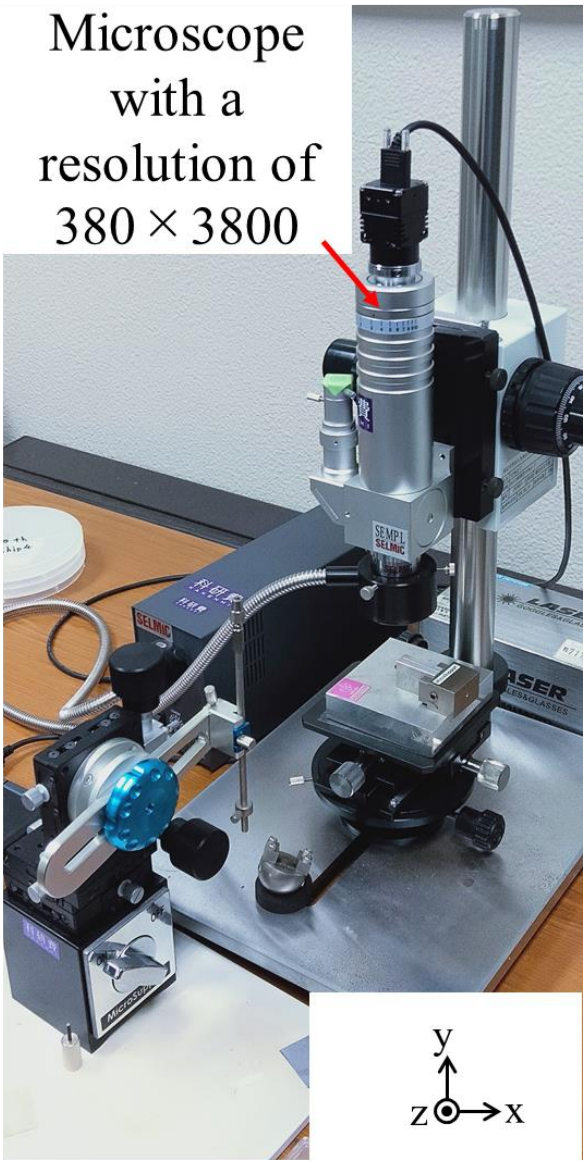

Figure 5.8: Actual experimental apparatus for the static driving test

The numerical problem setups representing the upward and downward flapping motions corresponding to the experiment are shown in Figs. 5.9(A) and (B), respectively. As shown here, both the y- and z-displacements u_y and u_z, as well as the prescribed x-displacement u_x, should be considered as forced displacements in the numerical analysis according to their observations.

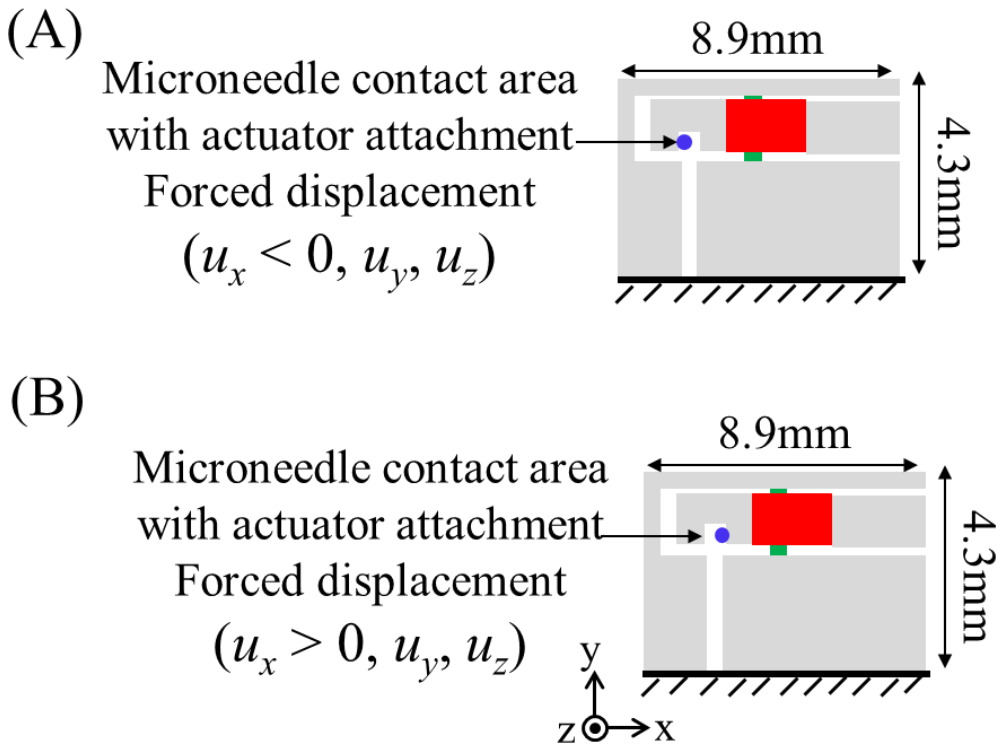

Figure 5.9: Problem setup for the (A) upward and (B) downward flapping motions, where the actuator attachment is pulled and pushed, respectively. Blue points represent the contact points of the microneedle on the sidewall of the actuator attachment

First, the effects of the forced y- and z-displacements u_y and u_z on the performance were evaluated using the numerical models shown in Fig. 5.9. In the models, the forced y-displacement should be evaluated because a slight in-plane rotation of the actuator attachment part occurs during the experimental static driving test, as shown in Figs. 5.10(A) and (B) for the upward and downward flapping motions, respectively, of sample 3.

Additionally, the forced z-displacement should be evaluated because the microneedle position along the z-direction changes during the experimental static driving test, as shown in Figs. 5.11(A) and (B) for the upward and downward flapping motions, respectively, for sample 2.

Figs. 5.10(C) and 5.11(C) show 3D views of the transmission with the supporting frame to demonstrate the in-plane rotation of the actuator attachment and the position of the microneedle along the z-direction, respectively, along with the positions of the actuator, the wing attachments, and the elastic hinges.

The slight rotation gives an additional y-displacement u_y at the contact area

between the microneedle and the actuator attachment, which can affect the flapping motion or the performance of the transmission.

Similarly, the change in position of the microneedle in the z-direction gives an additional z-displacement u_z at the area of contact between the microneedle and the actuator attachment, which can affect the flapping motion or the transmission performance.

Hence, the sensitivity analysis of these additional displacements u_y and u_z should be conducted as shown in the models in Figs. 5.9(A) and (B). The forced displacements in these models were set to $u_x = 100$, $-50\ \mu m \leq u_y \leq 50\ \mu m$, and $u_z = 0\ \mu m$ for the u_y sensitivity analysis, and $u_x = 100\ \mu m$, $u_y = 0$, and $-50\ \mu m \leq u_z \leq 50\ \mu m$ for the u_z sensitivity analysis to understand at what rate the in-plane rotation of the actuator attachment part and the microneedle displacement, respectively, affect the transmission performance.

The sensitivities of the actuator attachment in-plane rotation and microneedle displacement are shown in Figs. 5.12 and 5.13, respectively, for the upward and downward flapping motions. As shown in Fig. 5.12, the rate of change of the wingtip displacement in the z-direction was approximately 4 μm per 1 μm forced displacement u_y. As shown in Fig. 5.13, the rate of change of the wingtip displacement in the z-direction was approximately 2 μm per 1 μm forced displacement u_z.

The forced displacement u_y for the upward (downward) flapping motion observed in Fig. 5.10(A) (Fig. 5.10(B)) was approximately 20 μm (−30 μm), which reduced the magnitude of the wingtip displacement from that with $u_y = 0$ by 3% (10%).

The average forced displacement u_z for the upward (downward) flapping motion was approximately 20 μm (30 μm), as given in Table 5.3, which reduced the magnitude of the wingtip displacement from that with $u_z = 0$ by 1% (2%). It follows from these results and discussion that the forced displacements u_y and u_z do not significantly affect the performance. Hence, they can be considered 0 in the ideal limit. This ideal case can be realized by avoiding needle slippage during the static driving test.

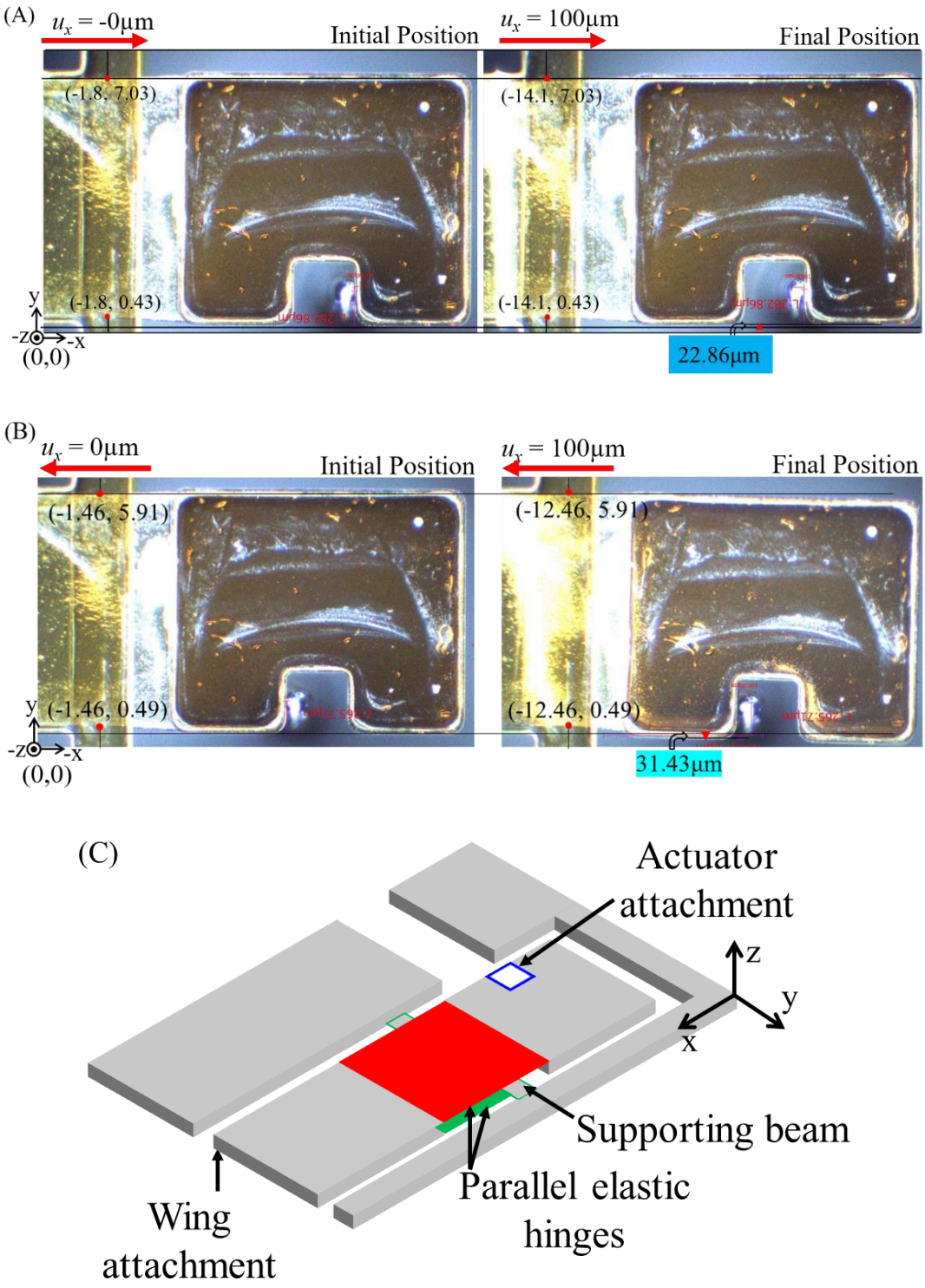

Figure 5.10: Observations of the *y*-displacement for the (A) upward and (B) downward flapping motions, where the actuator attachment is pushed and pulled, respectively (C) 3D view of the transmission with the supporting beam showing the positions of the actuator and wing attachment parts and the elastic hinges

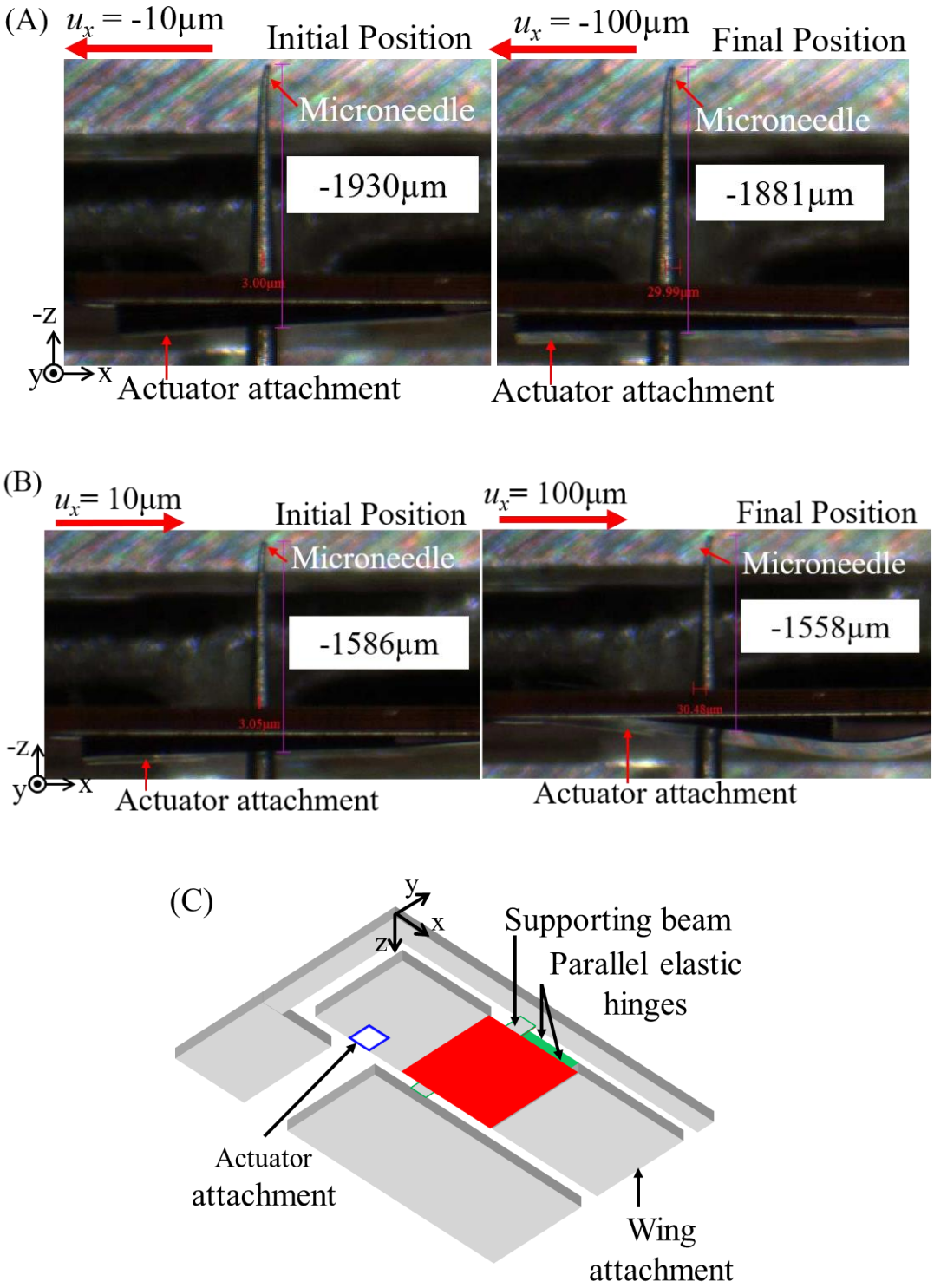

Figure 5.11: Observation of the forced *z*-displacement for the (A) upward and (B) downward flapping motions (C) 3D view of the transmission with the supporting beam

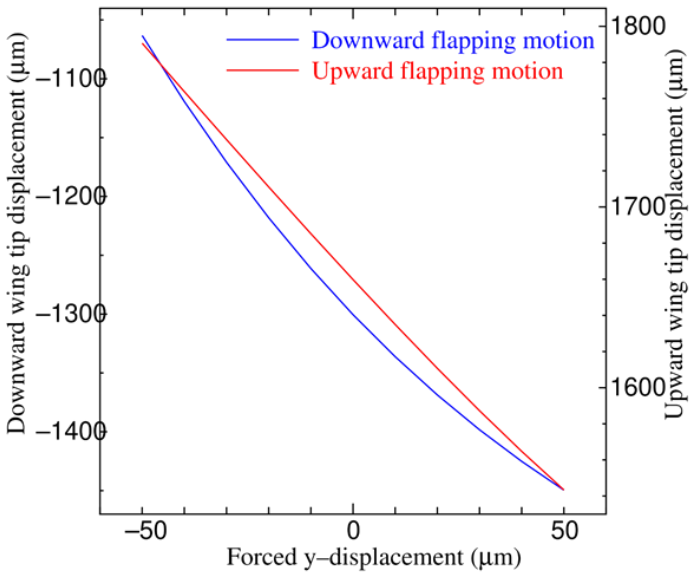

Figure 5.12: Sensitivity of the forced *y*-displacement for the upward and downward flapping motions

Table 5.3: Observation of the change in the position of the needle along the *z*-direction

Flapping motion	Sample 1	Sample 2	Sample 3	Average
Upward	41.0 µm	48.89 µm	-25.92 µm	21.32 µm
Downward	65.63 µm	27.76 µm	11.10 µm	34.83 µm

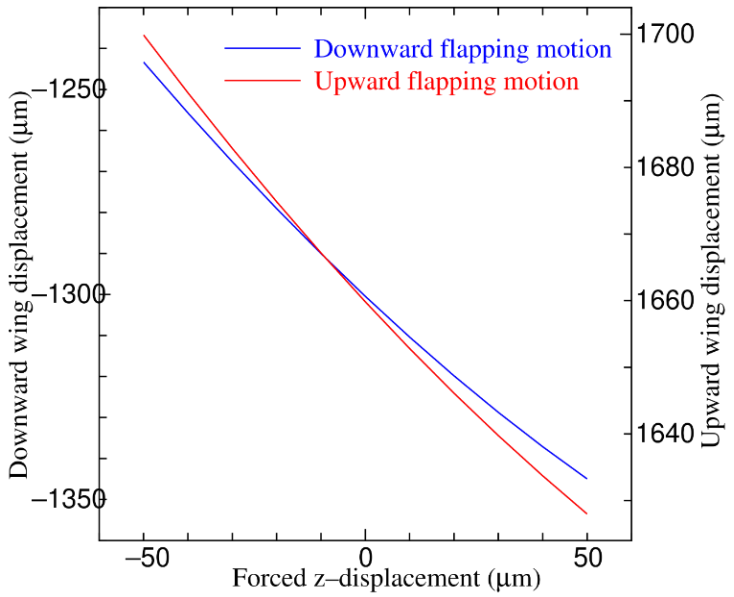

Figure 5.13: Sensitivity of the forced *z*-displacement for the upward and downward flapping motions

Figs. 5.14 and 5.15 show a comparison of the numerical and experimental results for the upward and downward flapping motions, respectively, of the transmission.

Figs. 5.14(A) and 5.15(A) show the static deformation of the transmission in the finite element analysis using Figs. 5.9(A) and (B), respectively, with the forced displacements set as $u_x = -100$ μm, $u_y = 20$ μm, and $u_z = 20$ μm for the former case and $u_x = 100$ μm, $u_y = -30$ μm, and $u_z = 30$ μm for the latter, as per the above discussion.

Figs. 5.14(B) and 5.15(B) show the static deformation of the transmission during the corresponding experimental static driving test, where the prescribed displacements of $u_x = -100$ μm and $u_x = 100$ μm, respectively, were applied quasi-statically using the microneedle, whose x-motion was controlled by the precision stage as shown in Fig. 5.7.

Figs. 5.14(C) and 5.15(C) show comparisons of the experimental and numerical results for the displacement of the wing attachment tip against the frame for the upward and downward flapping motions, respectively. As shown in these figures, maximum errors of approximately 6% and 13% between the experimental and numerical results occurred at the respective forced displacements of $u_x = -100$ and 100 μm.

Finally, the ability of the proposed transmission to produce the necessary stroke angle without any assistance from the mass inertial effect is presented. The stroke angle was evaluated to be approximately 30° from both the experimental and numerical results of the static driving tests for the considered actuator setup. This angle is comparable to the actual observed angle in insect flapping flight. Hence, the proposed transmission will produce a sufficient stroke angle to achieve flapping flight.

5.4.2 Effect of fabrication precision on transmission performance

This sub-section discusses the effect of the precision of various parts of the transmission on the transmission performance using the finite element method, building on the previous discussion of these precisions in Section 5.3.1. The design and observed dimensions of the transmission are taken from Table 5.1. The forced displacements in Figs. 5.9(A) and (B) were set according to the earlier discussion, i.e., $u_x = -100$ μm, $u_y = 20$ μm, and $u_z = 20$ μm for the upward flapping motion, and $u_x = 100$ μm, $u_y = -30$ μm, and $u_z = 30$ μm for the downward flapping motion.

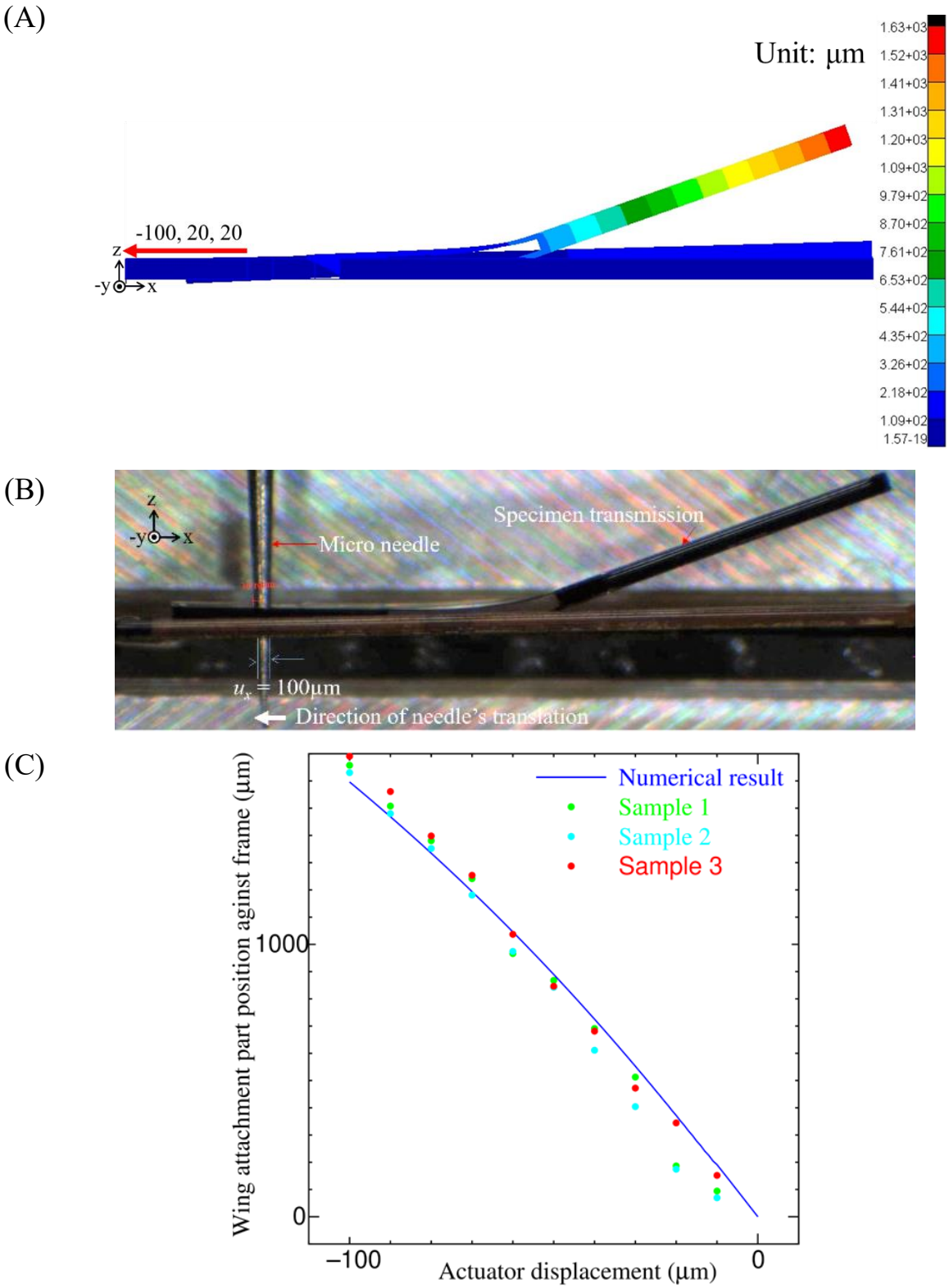

Figure 5.14: Static deformation of the transmission for upward flapping with the above written forced displacement obtained (A) by finite element analysis and (B) in the corresponding experiment (C) Experimental and numerical displacements of the wing attachment tip against the frame

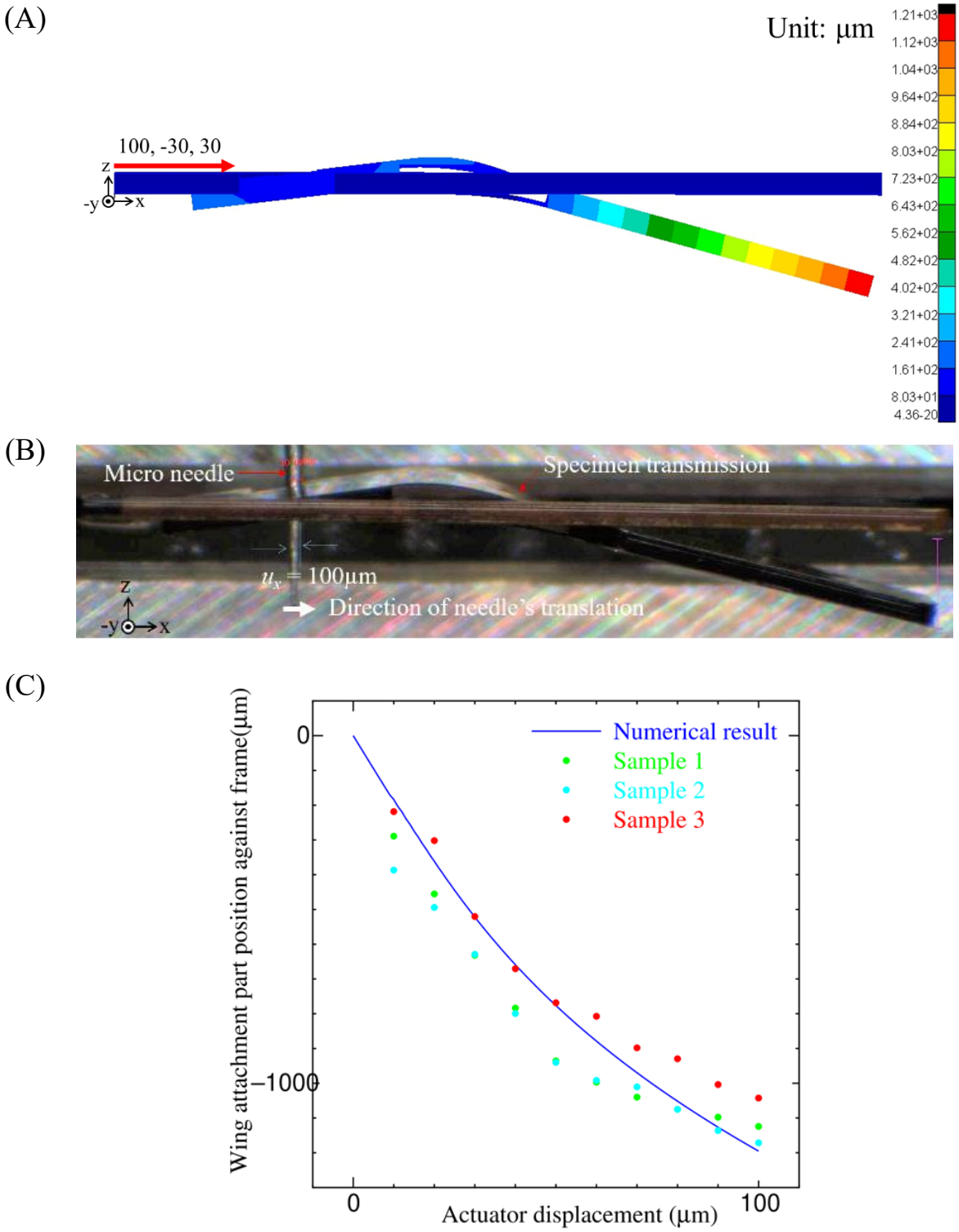

Figure 5.15: Static deformation of the transmission for downward flapping with the above written forced displacement obtained by (A) finite element analysis and (B) in the corresponding experiment (C) Experimental and numerical displacements of the wing attachment tip against the frame

First, only the in-plane dimensions were changed following the observed values, with the out-of-plane dimensions kept fixed at the design values. Table 5.4 shows the effect of this change on the performance of the upward and downward flapping motions. As shown in this table, the average effect of the in-plane precision on the performance was approximately 3%.

Next, the effect of the thickness on the transmission performance was evaluated. In this analysis, only the gap between the hinges was varied, with the other dimensions remaining fixed at the design values. As shown in Fig. 5.16, the average effect of the total thickness precision on the performance was approximately 4%. Fig. 5.17 shows the effect of the change of the elastic hinge thickness on the performance for the upward and downward flapping motions, with the thickness varying from 25 to 40 μm.

The lower bound of this range was selected as the lowest value observed in sample 1, and the upper bound was set as the design value. This parametric study is presented here because the elastic hinge thickness is considered a critical design parameter. The average effect of the elastic hinge thickness precision on the performance was approximately 5%. The average cumulative effect of all of the precisions on the performance was approximately 10–12%. These results indicate that deviations in the dimensions from the design value do not significantly affect the performance.

Table 5.4: Effect of changes of the in-plane dimensions on the error in the upward and downward flapping displacements

	Wing tip displacement [μm]	
	Upward flapping (error)	Downward flapping (error)
Sample 1	1541 (3.45%)	-1163 (2.70%)
Sample 2	1519 (4.82%)	-1151 (3.72%)
Sample 3	1560 (2.22)	-1180 (1.24%)
Design	1596 (base)	-1195 (base)

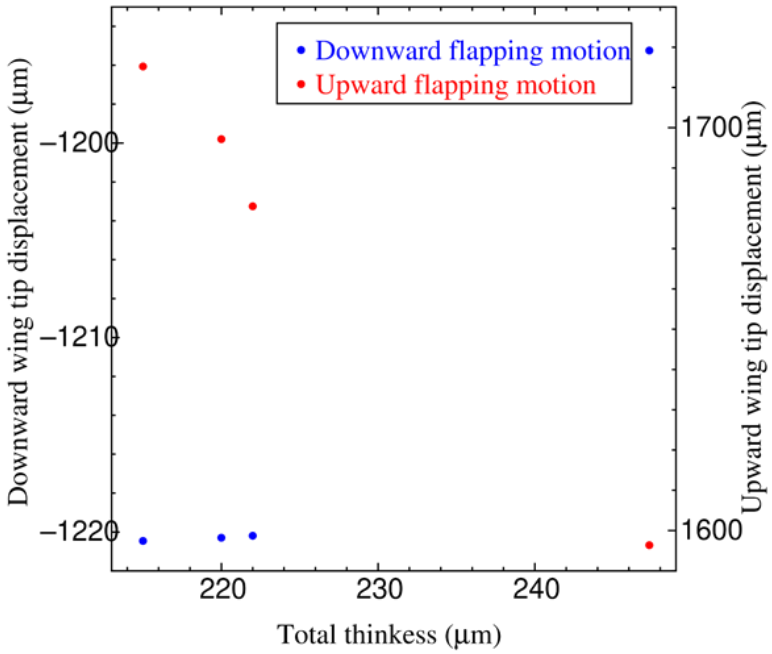

Figure 5.16: Upward and downward wing displacements plotted against the total thickness

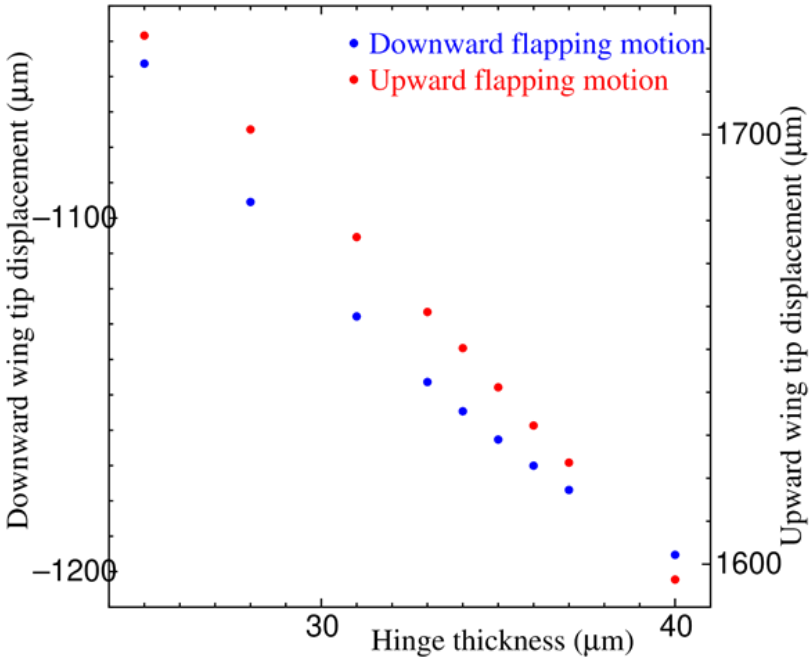

Figure 5.17: Upward and downward wing displacements plotted against the hinge thickness

5.5 Conclusion

In order to demonstrate the feasibility of polymer micromachining for the development of 2.5-dimensional FWNAVs, the proposed transmission of the first prototype has been developed. The novelty of this research is the ability to fabricate the complete 2.5-dimensional structure using standard microfabrication techniques including etching, photolithography, deposition, and curing without any post-assembly. The stroke angle of the proposed transmission is approximately 30° without any assistance from the resonance and the mass inertial effect. This stroke angle is comparable with that of actual insects during flapping flight. The overall average precision order of the fabricated transmission was approximately 75% in agreement with the representative dimensions. During the static driving test, the cumulative maximum error between the experimental and numerical results is about 10–12%, which is equivalent to the overall precision's effect on performance. Errors in the forced displacements u_y and u_z do not significantly affect the performance. The errors observed between experimental and numerical results due to minor errors during fabrication and static driving tests were negligible, and they can be reduced significantly with some care during experiments. It follows from these results that the polymer micromachining is feasible for developing mm size prototype because dimension and performance error between design and fabricated prototype is trivial. Thus, 10mm flyable FWNAV can be developed using polymer micromachining discussed here.

CHAPTER 6

GENERAL CONCLUSIONS

The main objective of this thesis was to design and develop an insect-inspired flapping-wing nano air vehicle (FWNAV), a complete 2.5-dimensional structure using polymer micromachining, and an iterative design window search methodology. In order to develop FWNAV, its main components: micro transmission with support frame and micro wings are designed and developed. In essence, this work is to determine to development of FWNAV and evaluation of its computational flight performance using the nonlinear dynamic and fluid-structure interaction (FSI) analyses.

In this thesis work, the following sub-objectives were proposed to achieve the main objective:

1. Design of a 2.5-dimensional micro transmission with a support frame to convert the translational displacement from the bimorph actuator into rotation displacement using nonlinear static structural analysis such that micro transmission should not break during fabrication and actual working. Evaluate the flapping performance for quasi-static actuation of the proposed transmission, demonstrated in Chapter 2.

2. An iterative design window (DW) search method should be proposed for accompanying the change in design problems which is the essential characteristic of 2.5-dimensional FWNAV. In order to obtain the DW for FWNAVs that satisfy all the necessary design requirements (DRs) like large stroke angle, and safely flap, using the above-mentioned method, sub-design windows should be searched. Firstly, DW should be searched for the mass of the micro wing which can be supported by micro transmission considering an inertial effect, and secondly, DW should be searched for miniaturizing the FWNAV (micro wing + micro transmission) using nonlinear structural dynamic analysis, as discussed in Chapter 3.

3. Computation flight performance of the FWNAVs should be evaluated using nonlinear structural dynamic and fluid-structure interaction (FSI) analyses. Flight performance should be further optimized by designing the wing

membrane thickness for large stroke angle and high flapping frequency using FSI analyses, as described in Chapter 4.

4. In order to fabricate the designed FWNAVs, the feasibility of polymer micromachining should be demonstrated. Micro transmission can be fabricated using polymer micromachining as a demonstration since transmission is a key and central component of FWNAV, discussed in Chapter 5.

These sub-objectives have been achieved to meet the aim of this thesis work. The following are the details.

In Chapter 2, A one wing transmission, whose functionality is based on geometrically nonlinear bending, was proposed in this study, and its design allows further miniaturization for use in FWNAVs. The novelty of this research is (1) the introduction of an elastic hinge in the design; (2) a transmission mechanism based on geometrically nonlinear bending deformation, in which a small translational displacement produces large rotational displacement; and (3) the ability to fabricate the complete 2.5-dimensional structure using standard microfabrication techniques including etching, photolithography, deposition, and curing without any post-assembly. The proposed transmission will increase the fabrication stability during polymer micromachining because of the absence of a hollow structure for sensitive layers.

The stroke angle of the proposed transmission is approximately 30° without any assistance from the resonance and the mass inertial effect. This stroke angle is comparable with that of actual insects during flapping flight. In this design, the maximum von Mises stress during the flapping motion was only 18% of the breaking strength of the PI sheet. Therefore, there is little chance of failure during transmission operation.

It follows from these results that the proposed transmission can enable the further miniaturization of FWNAVs because no post-assembly is required.

In Chapter 3, an iterative design window search methodology has been proposed using the nonlinear dynamic simulation and found the DW of the micro transmission as well as the FWNAV that satisfies the nonlinear and unsteady DRs conflicting with each other simultaneously. Each design solution in the DW shows a large stroke angle, which is comparable to that of the small flies, and it has a sufficient fatigue life.

DW search of transmission shows that it produces a stroke angle of about 50°

with a fatigue life of about 10^3–10^7 cycles for the flapping frequency of 100–150 Hz whereas the DW search on FWNAV indicates that it produces a stroke angle of about 90° with a fatigue life of about 10^3–10^4 cycles for the flapping frequency 100–125 Hz. The micro wing with a mass up to 5.3 mg can be supported by this transmission at the flapping frequency equivalent to the small flies. The proposed DW search results can miniaturize the FWNAV down to 10 mm.

The DW search on available piezoelectric bimorph actuator and length of 10 mm indicates that a voltage of range 300–460V is required to produce a constant vibration amplitude. In future work, we will develop the FWNAV based on the proposed DW using polymer micromachining. This is highly possible because of a 2.5-dimensional structure as already demonstrated in the previous chapter. Hence, this study will contribute to the further miniaturization of FWNAVs.

In Chapter 4, the flight simulation and performance of the first prototype and miniaturized design of polymer micromachined FWNAV which is based on iterative design window search results have been demonstrated using the two distinguish computational methods which include nonlinear dynamic and FSI analyses. The nonlinear dynamic analysis has been done with a complete FWNAV design whereas FSI analyses have been processed with micro wing only, to avoid the computational complexity associated with the FSI analysis of FWNAV. However, it was observed that the FSI analysis result with a micro wing is almost similar to the nonlinear dynamic analysis result of FWNAV, and using this one can conclude that the above-mentioned statement is correct.

The flight performance of the first prototype has shown a small mean feathering angle and low lift force because of the small stroke angle and low flapping frequency. Flight performance of miniaturized FWNAV design indicates good feathering angle and promising lift force to support their weight due to large stroke angle and high flapping frequency. It has been observed that the mean lift force of miniaturized design is about 10 times that of the first prototype.

Wing membrane thickness of 10μm would be preferable for large stroke angles and high flapping frequency. Optimization of flight performance indicates that the mean lift force is comparable to the weight of polymer micromachined FWNAV. Thus, this study shows promising results for miniaturization as well as good flight performance.

In Chapter 5, In order to demonstrate the feasibility of polymer micromachining for the development of 2.5-dimensional FWNAVs, the proposed transmission of the first prototype has been developed. The novelty of this

research is the ability to fabricate the complete 2.5-dimensional structure using standard microfabrication techniques including etching, photolithography, deposition, and curing without any post-assembly.

The stroke angle of the proposed transmission is approximately 30° without any assistance from the resonance and the mass inertial effect. This stroke angle is comparable with that of actual insects during flapping flight.

The overall average precision order of the fabricated transmission was approximately 75% in agreement with the representative dimensions. During the static driving test, the cumulative maximum error between the experimental and numerical results is about 10–12%, which is equivalent to the overall precision's effect on performance. Errors in the forced displacements u_y and u_z do not significantly affect the performance. The errors observed between experimental and numerical results due to minor errors during fabrication and static driving tests were negligible, and they can be reduced significantly with some care during experiments.

It follows from these results that the polymer micromachining is feasible for developing an mm size prototype because dimension and performance error between the design and the fabricated prototype is trivial. Thus, 10mm flyable FWNAV can be developed using polymer micromachining discussed here.

The main contributions of this thesis have been summarized below,

One wing transmission for FWNAV has been proposed to increase the fabrication stability which leads to an increase in yield ratio, its flapping performance for quasi-static actuation indicates that it has a sufficient stroke angle comparable to the natural insects, shown in Chapter 2.

The proposed iterative design window search methodology can be utilized to design and develop any number of FWNAVs and their further miniaturization. In this thesis proposed method has been demonstrated with the development of 10 mm FWNAV, discussed in Chapter 3.

In Chapter 4, computational methods including nonlinear dynamic and FSI analyses have been employed for the evaluation of the flight performance of FWNAVs. This study indicates that 10mm FWNAV can be able to lift off.

The feasibility of polymer micromachining for the development of 10mm FWNAV has been demonstrated by fabricating transmission with a support frame which is a central and key component of FWNAV. This indicates that polymer micromachining is feasible for an mm size FWNAV, as discussed in Chapter 5.

It follows from these results that the 10 mm flyable FWNAV has been designed using an iterative design window search methodology and developed using polymer micromachining.

BIBLIOGRAPHY

1. C. Galinski, “Influence of MAV Characteristics on their Applications”, Aviation, vol. 9, pp. 16–23, December 2005.
2. J. M. Grasmeyer and M. T. Keennon, “Development of the Black Widow Micro Air Vehicle”, 39th Aerospace Sciences Meeting and Exhibit, pp. 0127-0135, January 2001.
3. D. Jo and Y. Kwon, “Vertical Takeoff and Landing Wing Developed for Long Distance Flight and Stable Transit Flight”, International Journal of Mechanical Engineering and Robotics Research, vol. 8, pp. 797–802, September 2019.
4. G. Amendola, et. al., “Preliminary Design Process for an Adaptive Winglet”, International Journal of Mechanical Engineering and Robotics Research, vol. 7, pp. 83–92, January 2018.
5. M. Usman, A. Maqsood, S. R. Mulkana, and R. Riaz, “Gap Effect on Flight Performance and Longitudinal Stability of Biplane Micro Air Vehicles,” International Journal of Mechanical Engineering and Robotics Research, vol. 7, pp. 635–642, October 2018.
6. H. Ucgun, U. Yuzgec, and C. Bayilmis, “A Review on Applications of Rotary-Wing Unmanned Aerial Vehicle Charging Stations”, International Journal of Advanced Robotic Systems, vol. 18, pp. 1–20, May 2021.
7. F. Bohorquez, P. Samuel, J. Sirohi, D. Pines, L. Rudd, and R. Perel, “Design, analysis and hover performance of a rotary wing micro air vehicle”, Journal of the American Helicopter Society, vol. 48, pp. 80-90.

8. V. M. Mwongera, “A Review of Flapping Wing MAV Modelling”, International Journal of Aeronautical Science & Aerospace Research, vol. 2, pp. 27-36, April 2015.
9. Rashmikant, D. Ishihara, R. Suetsugu, and P. C. Ramegowada, “One-wing polymer micromachined transmission for insect-inspired flapping-wing nano air vehicle”, Engineering Research Express, vol. 3, pp. 045006–25, October 2021
10. R. Madangopal, Z. A. Khan, and S. K. Agrawal, “Biologically inspired design of small flapping wing air vehicles using four bar mechanisms and quasi-steady aerodynamics”, Journal of Mechanical Design, vol. 127 pp. 809–824, July 2005.
11. L. Hines, D. Campolo, and M. Sitti, “Liftoff of a motor-driven flapping-wing micro aerial vehicle capable of resonance”, IEEE Transaction on Robotics, vol. 30 pp. 220–232, September 2013.
12. W. Bejgerowski, J. W. Gerdes, S. K. Gupta, and H. A. Bruck, “Design and fabrication of miniature compliant hinges for multi-material compliant mechanisms”, The International Journal of Advanced Manufacturing Technology, vol. 57 pp. 437–452, April 2011.
13. W. Bejgerowski, A. Ananthanarayanan, D. Mueller, and S. K. Gupta, “Integrated product and process design for a flapping wing drive mechanism”, Journal of Mechanical Design, vol. 131, pp. 1-9, June 2009.
14. D. Mueller, H. A. Bruck, and S. K. Gupta, “Measurement of thrust and lift forces associated with drag of compliant flapping wing for micro air vehicles using a new test stand design”, Experimental Mechanics, vol. 50, pp. 725–735, July 2009.
15. R. Sahai, K. C. Galloway, and R. J. Wood, “Elastic element integration for improved flapping-wing micro air vehicle performance”, IEEE Transaction on Robotics, vol. 29 pp. 32–41, October 2012.
16. R. Sahai, K. C. Galloway, M. Karpelson, and R. J. Wood, “A flapping-wing micro air vehicle with interchangeable parts for system integration studies”, Proc. of IEEE/RSJ International Conference on Intelligent Robots and Systems, pp 501–506, October 2012.
17. D. H. Gong, D. W. Lee, J. S. Sang, and S. Y. Kim, “Design and experiment of string-based flapping mechanism and modulized trailing edge control

system for insect-like FWMAV", American Institute of Aeronautics and Astronautics (AIAA) Information Systems- AIAA Infotech @ Aerospace, pp. 1-13, January 2018.
18. C. Chen and T. Zhang, "A Review of Design and Fabrication of the Bionic Flapping Wing Micro Air Vehicles", vol. 10, pp. 1-20, February 2019.
19. G.C.H.E. de Croon, K.M.E. de Clercq, R. Ruijsink, B. Remes, and C. de Wagter, "Design, Aerodynamics, and Vision-Based Control of the DelFly", International Journal of Micro Air Vehicles, vol. 2, pp. 71-97, June 2019.
20. R.J. Wood, "The First Takeoff of a Biologically Inspired at-scale Robotic Insect", IEEE Transactions on Robotics, vol. 24, pp. 341–347, April 2008.
21. L. Petricca, P. Ohlckers, and C. Grinde, "Micro-and Nano-air vehicles: state of the art" International Journal of Aerospace Engineering, volume 2011, 214549-65, February 2011.
22. S. Sudo, K. Tsuyuki, and K. Kanno, "Wing characteristics and flapping behavior of flying insects", Experimental Mechanics, vol. 45 pp. 550–555, December 2005.
23. T. Hylton, C. Martin, R. Tun, and V. Castelli, "The DARPA Nano Air Vehicle Program", 50th AIAA Aerospace Sciences Meeting including the New Horizons Forum and Aerospace Exposition, pp. 0583-91, January 2012.
24. S. S. Baek, K. Y. Ma, and R. S. Fearing, "Efficient resonant drive of flapping-wing robots", Proc. of IEEE/RSJ International Conference on Intelligent Robots and Systems, pp 2854–2860, December 2009.
25. M. Sitti, "Piezoelectrically actuated four-bar mechanism with two flexible links for micromechanical flying insect thorax", IEEE/ASME Transaction on Mechatronics, vol. 8 pp. 26–36, March 2003.
26. V. Arabagi, L. Hines, and M. Sitti, "Design and manufacturing of a controllable miniature flapping wing robotic platform", International Journal of Robotic Research, vol. 31 pp. 785–800, February 2012.
27. M. Karpelson, G. Y. Wei, and R. J. Wood, "Driving high voltage piezoelectric actuators in micro robotic applications", Sensors and Actuators A: Physical vol. 176, pp. 78–89, April 2012.
28. N. O. Pérez-Arancibia, K. Y. Ma, K. C. Galloway, J. D. Greenberg, and R. J. Wood, "First controlled vertical flight of a biologically inspired microrobot", Bioinspiration and Biomimetics, vol. 6, pp. 1-12, August 2011.

29. K. Meng, W. Zhang, W. Chen, H. Li, P. Chi, C. Zou, X. Wu, F. Cui, W. Liu, and J. Chen, “The design and micromachining of an electromagnetic MEMS flapping-wing micro air vehicle”, Microsystem Technologies, vol. 18 pp. 127–36, January 2012.
30. W. Shyy, C. K. Kang, P. Chirarattananon, S. Ravi and H. Liu, “Aerodynamics, sensing, and control of insect-scale flapping-wing flight”, Proceedings of Royal Society A, vol. 472, pp. 20150712, February 2016.
31. B. Singh, “Dynamics and aeroelasticity of hover-capable flapping wings: Experiments and analysis,” Ph.D. Dissertation, University of Maryland, College Park, 2007.
32. Pringle, J.W.S. Insect flight; Cambridge University Press: Cambridge, UK, 1957.
33. H. Dong, A. T. Bode-Oke, and C. Li, “Learning from Nature: Unsteady Flow Physics in Bioinspired Flapping Flight,” in Flight Physics - Models, Techniques and Technologies, K. Volkov, Ed. Intech open, chapter 1, pp. 2-18, February 2018
34. X. Cheng and M. Sun, “Revisiting the clap-and-fling mechanism in small wasp Encarsia Formosa using quantitative measurements of the wing motion”, Physics of fluids, vol. 31, pp. 101903-12, October 2019.
35. M. J. Lighthill, “On the Weis–Fogh mechanism of lift generation”, Journal of Fluid Mechanics, vol. 60, pp. 1-17, August 1973.
36. S. Ho, H. Nassefa, N. Pornsinsirirak, Y. C. Tai, and C. M. Ho, “Unsteady aerodynamics and flow control for flapping wing flyers”, Progress in Aerospace Sciences, vol. 39, pp. 635–681, November 2003.
37. T. Maxworthy, “Experiments on the Weis–Fogh mechanism of lift generation by insects in hovering flight Part I. Dynamics of the ‘fling’”, Journal of Fluid Mechanics, vol. 93, pp. 47-63, July 1979.
38. C. P. Ellington, “Unsteady aerodynamics of insect flight”, Symposia of the Society for Experimental Biology, vol. 49, pp. 109-129, 1995.
39. M. H. Dickinson, F. O. Lehmann, S. P. Sane, “Wing rotation and the aerodynamic basis of insect flight”, Science, vol. 284, pp. 1954-1960, June 1999.
40. Birch, “Investigation of the near-field tip vortex behind an oscillating wing”, Journal of Fluid Mechanics, vol. 544, pp. 201-241, December 2005.

41. T. Maxworthy, “The fluid-dynamics of insect flight”, Annual Review of Fluid Mechanics, vol. 13, pp. 329-350, January 1981.
42. C. B. van den, C. P. Ellington, “The vortex wake of a ‘hovering’ model hawkmoth”, Philosophical Transactions of the Royal Society of London, vol. B 352, pp. 317-328, March 1997.
43. S. P. Sane, M. H. Dickinson, “The aerodynamic effects of wing rotation and a revised quasi steady model of flapping flight” The Journal of Experimental Biology, vol. 205, pp. 1087-1096, April 2002.
44. M. H, Dickinson, “The Effects of wing rotation on unsteady aerodynamic performance at low Reynolds numbers”, The Journal of Experimental Biology, vol. 192, pp. 179-206, July 1994.
45. G. Liu, H. Dong, C. Li, “Vortex dynamics and new lift enhancement mechanism of wing–body interaction in insect forward flight”, Journal of Fluid Mechanics, vol. 795, pp. 634-651, May 2016.
46. D. Ishihara, “Computational Approach for the Fluid-Structure Interaction Design of Insect-Inspired Micro Flapping Wings”, Fluids, vol. 7 (1) 26, January 2022.
47. D. Ishihara, R. Takata, P. C. Ramegowda, and N. Takayama, “Strongly coupled partitioned iterative method for the structure–piezoelectric–circuit interaction using hierarchical decomposition”, Computers & Structures, Vol. 253, pp. 1-17, May 2021.
48. D. Ishihara, H. Liu, and S. Yoshimura, “Computational Biomechanics and Biomimetics of Flapping Flight” Minisymposia at 15th World Congress on Computational Mechanics and 8th Asian Pacific Congress on Computational Mechanics, 2022.
49. D. Ishihara, A. Takei, T. Sawada, H. Kawai, and T. Yamada, “Advanced Numerical Analysis and Software in Multiphysics and Coupled Problems”, a symposium at the 41st JSST Annual International Conference on Simulation Technology, 2022.
50. S. Murakami, D. Ishihara, M. Araki, N. Ohira, T. Ito, and T. Horie, “Microfabrication of hybrid structure composed of rigid silicon and flexible PI membranes”, Micro and Nano Letters, vol. 12, pp. 913–915, August 2017.

51. A. Bontemps, T. Vanneste, J. B. Paquet, T. Dietsch, S. Grondel, and E. Cattan, “Design and performance of an insect-inspired nano air vehicle”, Smart Material and Structures, volume 22, 014008-20, 2013.
52. T. Dargent, X. Q. Bao, S. Grondel, G. Le Brun, J. B. Paquet, C. Soyer, and E. Cattan, “Micromachining of an su-8 flapping-wing flying micro-electro-mechanical system”, Journal of Micromechanics and Microengineering, volume 19, 085028-37, 2009.
53. T. Ozaki, and K. Hamaguchi, “Electro-aero-mechanical model of piezoelectric direct-driven flapping wing actuator”, Applied Sciences, volume 8, 1699-1716, 2018.
54. S. Murakami, D. Ishihara, M. Araki, T. Horie, N. Ohira, and T. Ito, “Microfabrication of hybrid structure composed of rigid silicon and flexible polyimide membranes”, Proc. 12th Annual IEEE International Conference on Nano/Micro Engineered and Molecular System, pp. 840–843, August 2017.
55. D. Ishihara, N. Ohira, M. Takagi, S. Murakami, and T. Horie, “Fluid-structure interaction design of insect-like micro flapping wing”, Proceedings of VII International Conference on Computational Methods for coupled problems in science and Engineering, pp. 870-875, June 2017.
56. D. Ishihara, S. Murakami, N. Ohira, J. Ueo, and M. Takagi, “Polymer micromachined transmission for insect-inspired flapping-wing nano air vehicle”, Proc. 15th Annual IEEE International Conference on Nano/Micro Engineered and Molecular System, pp. 176–179, September 2020.
57. D. Ishihara, T. Horie, M. Denda, “A Two-dimensional computational study on the fluid-structure interaction cause of wing pitch changes in dipteran flapping flight”, The Journal of Experimental Biology, vol. 212, pp. 1-10, January 2009.
58. D. Ishihara, “Role of Fluid-Structure interaction in generating the characteristic tip path of a flapping flexible wing”, Physical Review E, vol. 98, pp. 032411, September 2018.
59. D. Ishihara, T. Horie, and T. Niho, “An Experimental and three-dimensional computational study on the aerodynamic contribution to the passive pitching motion of flapping wings in hovering flies”, Bioinspiration and Biomimetics, vol. 9, pp. 046009-22, November 2014.

60. T. Nakata, and H. Liu, “A fluid-structure interaction model of insect flight with flexible wings”, Journal of Computational Physics, vol. 231, 1822-1847, 2012.
61. D. Ishihara and T. Horie, “A Projection Method for the monolithic interaction system of an incompressible fluid and a structure using a new algebraic splitting”, Computer Modeling in Engineering & Sciences, vol. 101, pp. 421-440, October 2014.
62. Rashmikant, D. Ishihara, R. Suetsugu, S. Murakami, and P. C. Ramegowada, “Improved design of polymer micromachined transmission for flapping-wing nano air vehicle”, Proc. 16th Annual IEEE International Conference on Nano/Micro Engineered and Molecular System, April 2021.
63. Rashmikant and D. Ishihara, “A Design Window Search Using Nonlinear Dynamic Simulation for Polymer Micro-machined Transmission in Insect-inspired Flapping wing Nano Air Vehicles”, Proceedings of 6th International Conference on Robotics and Automation Engineering (ICRAE), pp. 162-167, November 2021.
64. P. C. Ramegowda, D. Ishihara, R. Takata, T. Niho, and T. Hories, “Hierarchically decomposed finite element method for triply coupled piezoelectric, structural, and fluid fields of thin piezoelectric bimorph in fluid”, Computer Methods in Applied Mechanics and Engineering, vol. 375, pp. 113006, June 2020.
65. C. Zuyong, J. Xu, L. Binghe, Y. Zhang, and J. Wu, “Structural integrity analysis of transmission structure in flapping-wing micro aerial vehicle via 3D printing”, Engineering Failure Analysis, vol. 96, pp. 18-30, September 2018.
66. D. Ishihara, M. J. Jeong, S. Yoshimura, and G. Yagawa, “Design window search using continuous evolutionary algorithm and clustering-its application to shape design of microelectrostatic actuator”, Computers and Structures, vol.80, pp. 2469-2481, Dec. 2002.
67. C. P. Ellington, “The Novel aerodynamics of insect flight: applications to micro-air vehicles”, The Journal of Experimental Biology, vol. 202, pp. 3439-3448, November 1999.
68. W. C. Wheeler, M. Whiting, Q. D. Wheeler, and J. M. Carpenter, “The Phylogeny of the Extant Hexapod Orders”, Cladistics, vol. 17, pp. 113–169, July 2000.

69. C. P. Ellington, “The Aerodynamics of hovering insect flight II morphological parameters”, Philosophical Transaction of the Royal Society London, vol. B 305 pp. 17–40, February 1984.
70. A. R. Ennos, “The Kinematics and aerodynamics of the free flight of some diptera”, Journal of Experimental Biology, vol. 142, pp. 49-85, 1989.
71. A. R. Ennos, “A Comparative study of the flight mechanism of diptera”, Journal of Experimental Biology, vol. 127, pp. 355-372, September 1986.
72. M. Pfiester and P. E. Kaufman, “Drone fly, rat-tailed maggot *Eristalis tenax* (Linnaeus) (Insecta: Diptera: Syrphidae)” Electronic document Information system published by University of Florida, vol. EENY-445, pp. 1-6, March 2009.
73. C. P. Ellington, “The Aerodynamics of Hovering Insect Flight. III. Kinematics”, Philosophical Transaction of the Royal Society London, vol. B 305 pp. 41–78, February 1984.
74. Y. Liu and M. Sun, “Wing kinematics measurement and aerodynamics of hovering droneflies”, The Journal of Experimental Biology, vol. 211, pp. 2014-2025, April 2008.
75. J. H. Hu, and M. Sun, “Unsteady aerodynamic forces of a flapping wing”, Journal of Experimental Biology, vol. 207, pp. 1137-1150, January 2004.
76. G. E. Santo, E. B. da Silva, and E. Figueiredo, “Hoverfly (Diptera: Syrphidae) diversity in Tapada da Ajuda, Lisbon – a preliminary study”, Revista de Ciências Agrárias, vol. 41, pp. 133-140, December 2018.
77. Y. P. Liu and M. Sun, “Wing kinematics measurement and aerodynamic force and moments computation of hovering hoverfly”, Proc. 1st International Conference on Bioinformatics and Biomedical Engineering, pp. 452-455, July 2007.
78. T. Weis-Fogh, “Quick estimates of flight fitness in hovering animals, including novel mechanisms for lift production”, Journal of Experimental Biology, vol. 59, pp. 169-230, August 1973.
79. N. Xu, S. Zhou, C. Zhang, and X. Mou, “A Computational Study on Lateral Flight Stability of the Cranefly in Hover”, Computer Modeling in Engineering & Sciences, vol. 128, 669-685, May 2021.

80. V. E. Pilipenko, A. B. Ruchin, and G. B. Semishin, “Cranefly fauna (Diptera: Limoniidae, Pediciidae, Tipulidae) of the Republic of Mordovia, Russia”, Biodiversitas, vol. 21, pp. 355-369, January 2020.
81. S. S. Bhat, J. Zhao, J. Sheridan, K. Hourigan, and M. C. Thompsona, “Aspect ratio studies on insect wings”, Physics of Fluids, vol. 31, pp. 1-19, December 2019.
82. M. Sun and J. Tang, “Unsteady aerodynamic force generation by a model fruit fly wing in flapping motion”, The Journal of Experimental Biology, vol. 205, pp. 55-70, October 2001.
83. J. M. Zanker, “The Wing Beat of Drosophila Melanogaster. I. Kinematics”, Philosophical Transaction of the Royal Society London, vol. B 327, pp. 1-18, February 1990.
84. J. M. Zanker and K. G. Gotz, “The Wing Beat of Drosophila Melanogaster. II. Dynamics”, Philosophical Transaction of the Royal Society London, vol. B 327, pp. 1-18, February 1990.
85. P. M. O'Grady, “Drosophila melanogaster”, Encyclopedia of Insects: 2nd Edition, chapter 80, pp. 301-303, November 2009.
86. A. M. Vidal, Y. Huang, I. S. Ciudad, O. Shimmi, and D. Houle, “Quantitative morphological variation in the developing drosophila wing”, G3: Genes, Genomes, Genetics, vol. 8, pp. 2399-2409, June 2018.
87. M. H. Dickinson, F. O. Lehmann, and K. G. Götz, “The Active control of wing rotation by drosophila”, Journal of Experimental Biology, vol. 182, pp. 173-189, May 1993.
88. F. O. Lehmann and M. H. Dickinson, “The Production of elevated flight force compromises manoeuvrability in the fruit fly drosophila melanogaster” The Journal of Experimental Biology, vol. 204, pp. 627-635, February 2001.
89. C. P. Ellington, “The Aerodynamics of hovering insect flight. IV. aerodynamic mechanisms” Philosophical Transaction of the Royal Society London, vol. B 305 pp. 79–113, February 1984.
90. C. P. Ellington, “The Aerodynamics of hovering insect flight. V. A vortex theory” Philosophical Transaction of the Royal Society London, vol. B 305 pp. 115–144, February 1984.

91. C. P. Ellington, “The Aerodynamics of hovering insect flight. VI. Lift and power requirements” Philosophical Transaction of the Royal Society London, vol. B 305 pp. 145–181, February 1984.
92. R. J. Wood, B. Finio, M. Karpleson, K Ma, NO. P. Arancibia, P. S. Sreetharan, H. Tanaka, J. P. Whitney, “Progress on pico air vehicles”, The International Journal of Robotics Research, vol. 31, pp. 1292-1302, August 2012.
93. H. Liu, and H. Aono, “Size effects on insect hovering aerodynamics: an integrated computational study”, Bioinspiration and Biomimetics, volume 4, 015002-14, 2009.
94. E. Steltz, S. Avadhanula, and R. S. Fearing, “High lift force with 275 Hz wing beat in MFI”, Proc. IEEE/RSJ International Conference on Intelligent Robots and Systems, pp. 3993–3998, October 2007
95. N. T. Jafferies, E. F. Helbing, M. Karpelson, and R. J. Wood, “Untethered flight of an insect-inspired sized flapping-wing microscale aerial vehicle”, Nature, vol. 570, pp. 491-495, June 2019.
96. K. Y. Ma, P. Chirarattananon, S. B. Fuller, and R. J. Wood, “Controlled flight of a biologically inspired, insect-scale robot”, Science, vol. 340, pp. 603–607, May 2013.
97. Y. Zou, W. P. Zhang, and Z. Zhang, “Liftoff of an electromagnetically driven insect-inspired flapping-wing robot”, IEEE Transactions on Robotics, vol. 32, pp. 1285–1289, August 2016.
98. Z. Liu, X. Yan, M. Qi, X. Zhang, and L. Lin, “Low-voltage electromagnetic actuators for flapping-wing micro aerial vehicles”, Sensors and Actuators A: Physical, vol. 265, pp. 1–9, October 2017.
99. C. Cao, S. Burgess, and T. Conn, “Toward a dielectric elastomer resonator driven flapping-wing micro air vehicle”, Frontiers in Robotics and AI, vol. 5, pp. 137-147, January 2019.
100. X. Yan, M. Qi, and L. Lin, “Self-lifting artificial insect wings via electrostatic flapping actuators”, Proc. 28th IEEE International Conference on Micro Electro Mechanical Systems, pp. 22-25, January 2015.
101. A. Bontemps, et. al., “Modeling and evaluation of power transmission of flapping wing nano air vehicle” Proc. IEEE/ASME International Conference on Mechatronic and Embedded Systems & Applications, pp. 1−6, September 2014.

102. J. A. Roll, B. Cheng, X. Deng, “Design, fabrication, and experiments of an electromagnetic actuator for flapping wing micro air vehicles”, Proc. IEEE International Conference on Robotics and Automation, pp. 809-815, October 2013.
103. G. K. Lau, H. T. Lim, J. Y. Teo, and Y. W. Chin, “Lightweight mechanical amplifiers for rolled dielectric elastomer actuators and their integration with bio-inspired wing flappers”, Smart Materials and Structures, vol. 23, pp. 025021-33, January 2014.
104. S. Ryu and H. J. Kim, “Development of a flapping-wing micro air vehicle capable of autonomous hovering with onboard measurements”, Proc. of IEEE/RSJ International Conference on Intelligent Robots and Systems (IROS), pp. 1-7, September 2017.
105. Y. Chen, H. Zhao, J. Mao, P. Chirarattananon, E.F. Helbling, N.S.P. Hyun, D.R. Clarke, and R. J. Wood, “Controlled flight of a microrobot powered by soft artificial muscles”, Nature, volume 575, 324-329, 2019.
106. Z. Liu, X. Yan, M. Qi, Y. Zhu, D. Huang, X. Zhang, and L. Lin, “Design of flexible hinges in electromagnetically driven artificial flapping-wing insects for improved lift force”, Journal of Micromechanics and Microengineering, volume 29, 015011-22, 2019.
107. Y. Zou, W. Zhang, X. Ke, X. Lou, S. Zhou, “The design and microfabrication of a sub 100 mg insect-scale flapping-wing robot”, Micro & nano letters, volume 5, Iss. 5, pp. 297–300, 2017.
108. Y. Zou, W. Zhang, S. Zhou, X. Ke, F. Cui, W. Liu, “Monolithic fabrication of an insect-scale self-lifting flapping-wing robot”, Micro & Nano Letters, Volume 13, Iss. 2, pp. 267–269, 2018.
109. P. S. Sreetharan, J. P. Whitney, M. D. Strauss, and R. J. Wood, “Monolithic fabrication of millimeter-scale machines”, Journal of Micromechanics and Microengineering, volume 22, pp. 055027, 2012.
110. R. J. Wood, “Liftoff of a 60mg flapping-wing MAV”, Proceedings of the IEEE/RSJ International Conference on Intelligent Robots and Systems, pp. 1–6, November 2007.
111. T. Vanneste, J.B. Paquet, S. Grondel, and E. Cattan, “Design of a lift-optimized flapping-wing using a finite element aeroelastic framework of

insect flight", Proc. of 53rd AIAA/ASME/ASCE/AHS/ASC Structures, Structural Dynamics and Materials Conference, pp. 1-12, April 2012.
112. T. Ozaki and K. Hamaguchi, "Bioinspired flapping-wing robot with direct-driven piezoelectric actuation and its takeoff demonstration", IEEE Robotics and Automation Letters, vol. 3, pp. 4217-4224, October 2018.
113. A. J. Bergou, S. Xu, and Z. J. Wang, "Passive wing pitch reversal in insect flight", Journal of fluid mechanics, vol. 591, 321–37, 2007.
114. A. L. Desbiens, Y. Chen, R. J. Wood, "A wing characterization method for flapping-wing robotic insects", Proceedings of IEEE/RSJ International Conference on Intelligent Robots and Systems (IROS), pp. 1–7, November 2013.
115. K. Mateti, R. A. Byrne-Dugan, S. A. Tadigadapa and C. D. Rahn, "Suex flapping-wing mechanisms for pico air vehicles", Proceedings of ASME International Conference on Smart Materials, Adaptive Structures, and Intelligent Systems, 583–90, 2012.
116. K. Mateti, R. A. Byrne-Dugan, S. A. Tadigadapa, and C. D. Rahn, "Wing rotation and lift in SUEX flapping-wing mechanisms", Smart Material and Structure, vol. 22, 014006-16, 2013.
117. R. Zhang, H. Zhang, L. Xu, P. Xie, J. Wu, and C. Wang, "Mechanism and kinematics for flapping wing micro air vehicles maneuvering based on bilateral wings", International Journal of Aerospace Engineering, vol. 2022, 1–10, February 2022.
118. M. Ryan and H. J. Su, "Classification of flapping wing mechanisms for micro air vehicles" Proceedings of International Design Engineering Technical Conference and Computers and Information in Engineering Conference, pp. 105–15, August 2012.
119. C. Zhang and C. Rossi, "A Review of compliant transmission mechanisms for bio-inspired flapping-wing micro air vehicles" Bioinspiration and Biomimetics, vol. 12, pp. 025005–19, February 2017.
120. A. Santhanakrishnan, S. K. Jones, W. B. Dickson, M. Peek, V. T. Kasoju, M. H. Dickinson, and L. A. Miller, "Flow structure and force generation on flapping wings at low Reynolds numbers relevant to the flight of tiny insects", Fluids, vol. 3, pp. 1-22, 2018.

121. Y. Z. Lyu, H. J. Zhu, M. Sun, “Aerodynamic forces and vortical structures of a flapping wing at very low Reynolds numbers”, Physics of Fluids, vol. 31, 041901, 2019.
122. S. Xiao, K. Hu, B. Huang, H. Deng, and X. Ding, “A Review of research on the mechanical design of hoverable flapping wing micro-air vehicles”, Journal of Bionic Engineering, vol. 18, pp. 1235–1254, November 2021.
123. S. Mishra, B. Tripathi, S. Garg, A. Kumar, and P. Kumar, “Design and development of a bio-inspired flapping wing type micro air vehicle”, Procedia Materials Science, vol. 10, pp. 519–526, August 2015.
124. M. Keennon, K. Klingebiel, and H. Won, “Development of the nano hummingbird: a tailless flapping wing micro air vehicle” Proceedings of the 50th AIAA Aerospace Sciences Meeting, pp. 588-602, November 2012.
125. J. H. Jeon, H. Cho, Y. Kim, J. H. Lee, D. H. Gong, S. J. Shin, and C. Kim “Design and analysis of the link mechanism for the flapping wing MAV using flexible multi-body dynamic analysis”, International Journal of Micro Air Vehicles, vol. 9, pp. 253-269, February 2017.
126. T. A. Nguyen, H. V. Phan, T. K. L. Au, and H. C. Park, “Experimental study on thrust and power of flapping-wing system based on rack-pinion mechanism”, Bioinspiration and Biomimetics, vol. 11, pp. 046001, June 2016.
127. C. H. Liu and C. K. Chen, “Kinematic analysis of a flapping-wing micro-aerial-vehicle with Watt straight-line linkage”, Journal of Applied Science and Engineering, vol. 18, pp. 355–362, October 2015.
128. G. K. Lau, Y. W. Chin, J. T. W. Goh, and R. J. Wood, “Dipteran-insect-inspired thoracic mechanism with nonlinear stiffness to save inertial power of flapping-wing flight”, IEEE Transaction of Robotics, vol. 30, pp. 1187–97, October 2014.
129. Y. Zhang, Y. Peng, Y. Cheng, and H. Yu, “A Novel piezo-actuated flapping mechanism based on inertia drive”, Journal of Intelligent Material Systems and Structures, vol. 31, pp. 1782–1792, June 2020.
130. L. L. Howell, Compliant Mechanisms, Wiley, July 2001.
131. K. Mateti, R. A. Byrne-Dugan, C. D. Rahn, and S. A. Tadigadapa, “Monolithic SUEX flapping wing mechanisms for pico air vehicle applications”, Journal of Microelectromechanical Systems, vol. 22, pp. 527–35, December 2012.

132. D. Ishihara and T. Horie, “Fluid-structural interaction modeling of insect flight”, Transactions of the Japan Society of Mechanical Engineers B, volume 72, 1410-1417, 2006.
133. D. Ishihara, Y. Yamashita, T. Horie, S. Yoshida, and T. Niho, “Passive maintenance of high angle of attack and its lift generation during flapping translation in crane fly wing”, The Journal of Experimental Biology, volume 212, 3882-3891, 2009.
134. M. Onishi and D. Ishihara, “Partitioned method of insect flapping flight for maneuvering analysis”, Computer Modeling in Engineering & Sciences, vol. 121, pp. 145-175, 2019.
135. D. Ishihara and T. Horie, “Passive mechanism of pitch recoil in flapping insect wings”, Bioinspiration and Biomimetics, vol. 12, 016008-22, 2017.
136. N. S. Ha, Q. T. Truong, N. S. Gool, and H. C. Park, “Relationship between wingbeat frequency and resonant frequency of the wing in insects”, Bioinspiration and Biomimetics, vol. 8, pp. 046008, 2013.
137. J. A. Miyan and A. W. Ewing, “How Diptera move their wings: A reexamination of the wing base articulation and muscle systems concerned with flight,” Philosphical Transaction Royal Society London, vol. B 311, pp. 271–302, 1985.
138. M. A. Jankauski, “Measuring the frequency response of the honeybee thorax”, Bioinspiration and Biomimetics, vol. 15, pp. 046002, 2020.
139. M. Hrncir, A. -I. Gravel, D. L. P. Schorkopf, V. M. Schmidt, R. Zucchi, and F. G. Barth, “Thoracic vibrations in stingless bees (Melipona seminigra): resonances of the thorax influence vibrations associated with flight but not those associated with sound production”, The Journal of Experimental Biology, vol. 211, 678–85, 2008.
140. J. Zhang and X. Deng, “Resonance principle for the design of flapping wing micro air vehicles”, IEEE Transactions on Robotics, vol. 99, 1-15, 2017.
141. M. Lok, D. Brooks, R. Wood, and G. Y. Wei, “Design and analysis of an integrated driver for piezoelectric actuators” IEEE Energy Conversion Congress and Exposition, pp 2684–91, October 2013.
142. N. T. Jafferis, E. F. Helbling, M. Karpelson, and R. J. Wood, “Untethered flight of an insect-sized flapping-wing microscale aerial vehicle”, Nature, vol. 570, pp. 491–495, June 2019.

143. R. J, Wootton, “Springy shells, pliant plates and minimal motors: abstracting the insect thorax to drive a micro-air vehicle” Flying Insects and Robots (Springer), pp 207–17, August 2009.
144. P. J. Gullan and P. S. Cranston, The Insects: An Outline of Entomology, Wiley, 2014.
145. J. L. Nation, Insect Physiology and Biochemistry, CRC Press, 2008.
146. X. Q. Bao, A. Bontemps, S. Grondel, and E. Cattan, “Design and fabrication of insect-inspired composite wings for MAV application using MEMS technology”, Journal of Micromechanics and Microengineering, vol. 21, pp. 125020-16, November 2011.
147. G. K. Lau, Y. W. Chin, and T. G. La, “Development of elastomeric flight muscles for flapping wing micro air vehicles”, Proceedings of Electroactive Polymer Actuators and Devices, vol. 10163, pp. 1016320-9, April 2017.
148. R. Pelrine, R. D. Kornbluh, Q. Pei, S. Stanford, S. Oh, J. Eckerle, R. J. Full, M. A. Rosenthal, and K. Meijer, “Dielectric elastomer artificial muscle actuators: toward biomimetic motion”, Proceedings of Smart Structures and Materials: Electroactive Polymer Actuators and Devices, vol. 4695, pp 126–37, July 2002.
149. K. J. Bathe, Finite Element Procedures, Prentice-Hall, 1996.
150. Q.M. Wang, and L.E. Cross, “Performance analysis of piezoelectric cantilever bending actuator”, Ferroelectrics, vol. 215, 187-213, 1998.
151. P. C. Ramegowada, D. Ishihara, T. Niho, and T. Horie, “Performance evaluation of numerical finite element coupled algorithms for structure-electric interaction analysis of MEMS piezoelectric actuator”, International Journal of Computational Methods, vol. 16, 1850106-33, 2019.
152. X. Cheng, and M. Sun, “Wing-kinematics measurement and aerodynamics in a small insect in hovering flight”, Nature, vol. 6, 25706-17,2016.
153. https://www.toray.jp/electronic/semicon/poly/index.html.
154. D. Ishihara, M. J. Jeong, S. Yoshimura, and G. Yagawa, “Design window search using continuous evolutionary algorithm and clustering –its application to shape optimization of microelectrostatic actuator”, Computers and Structures, vol.80, pp. 2469-2481, December 2002.

155. M. J. Jeong, Y. J. Kim, D. Ishihara, S. Yoshimura, and G. Yagawa, “Shape design of micro electrostatic actuator using multidimensional design windows”, Transactions of the KSME, vol.25 (A), pp.1796-1801, 2001
156. D. Ishihara, M. J. Jeong, S. Yoshimura, G. Yagawa, H. Komori, and Y. J. Kim, “Automated search for multidimensional design windows using continuous evolutionary algorithms and improved k-means clustering”, Transactions of the Japan Society of Mechanical Engineers, vol.67 (C), pp.460-468, 2001 (in Japanese).
157. D. Ishihara, M. J. Jeong, S. Yoshimura, G. Yagawa, and Y. J. Kim, “Structural design of micro electrostatic actuator for optical memory using design window search method”, Proceedings of the 4th International Conference on Modeling and Simulation of Microsystems, pp.157-160, 2001.
158. D. Ishihara, J. Yokota, M. Onishi, T. Niho, and T. Horie, “A shape simplification modeling of the cambering in insect’s flapping wings using beam and shell”, Transactions of the Japan Society for Computational Engineering and Science, vol. 2018, December 2018.
159. M. Oonishi, and D. Ishihara, “Performance evaluation of the pixel wing model for the insect wing’s camber” Journal of advanced simulation in science and engineering, vol. 8 (2), 163-172, July 2021.
160. W.D.Pilkey, Peterson’s stress concentration factors, Wiley, 1997.
161. https://www.toray.jp/plastics/en/amilan/technical/tec006.html
162. J. Choi, D. Gong, J. Lee, C. Kim, and S. Shin, “Simulation of the flapping wing aerial vehicle using flexible multibody dynamics” International Journal of Micro Air Vehicles, vol. 13, pp. 1–12, October 2021.
163. D. Ishihara, S. Yoshimura, and G. Yagawa, “Multi-steps strong coupling method for interaction of incompressible viscous fluid and an elastic body”, Proceedings of 5th World Congress on Computational Mechanics, pp. 1–10, 2002
164. D. Ishihara, S. Yoshimura, G. Yagawa, “Parallel multi-steps strong coupling method for interaction of incompressible viscous fluid and an elastic body with finite deformation”, Proceedings of the 7th US National Congress on Computational Mechanics, pp. 514, 2003.
165. D. Ishihara, S. Yoshimura, G. Yagawa, “Parallel multi-steps strong coupling method for interaction of incompressible viscous fluid and an elastic

body", Proceedings of 2nd M.I.T. Conference on Computational Fluid and Solid Mechanics, vol.2, pp.1373-1376, June 2003.
166. Q. Zhu, "Numerical simulation of a flapping foil with chordwise or spanwise flexibility", Journal of American Institute of Aeronautics and Astronautics, vol. 45, pp. 2448–2457, October 2007.
167. M. Hanamoto, Y. Ohta, K. Hara, and T. Hisada, "Application of fluid–structure interaction analysis to flapping flight of insects with deformable wings" Advanced Robotics, vol. 21, pp. 1–21, January 2007.
168. W. B. Tay, "Symmetrical and non-symmetrical 3D wing deformation of flapping micro aerial vehicles", Aerospace Science and Technology, vol. 55, pp. 242–251, August 2016.
169. S. K. Chimakurthi, J. Tang, R. Palacios, C. E. S. Cesnik, and W. Shyy, "Computational aeroelasticity framework for analyzing flapping wing micro air vehicles", Journal of American Institute of Aeronautics and Astronautics, vol. 47, pp. 1865–1878, August 2009.
170. S. K. Chimakurthi, C. E. S. Cesnik, and B. Stanford, "Flapping wing structural dynamics formulation based on a corotational shell finite element", Journal of American Institute of Aeronautics and Astronautics, vol. 49, pp. 128–142, January 2011.
171. R. E. Gordnier, S. K. Chimakurthi, C. E. S. Cesnik, and P. J. Attar, " High-fidelity aeroelastic computations of a flapping wing with spanwise flexibility" Journal of Fluids and Structures, vol. 40, pp. 86–104, July 2013.
172. H. Cho, J. Y. Kwak, S. J. Shin, N. Lee, and S. Lee, "Flapping wing fluid–structural interaction analysis using corotational triangular planar structural element", Journal of American Institute of Aeronautics and Astronautics, vol. 54, pp. 2265–2276, June 2016.
173. H. Cho, N. Lee, J. Y. Kwak, S. J. Shin, and S. Lee, "Three-dimensional fluid–structure interaction analysis of a flexible flapping wing under the simultaneous pitching and plunging motion", Nonlinear Dynamics, vol. 86, pp. 1951–1966, August 2016.
174. A. Gogulapati, P. P. Friedmann, E. Kheng, and W. Shyy, "Approximate aeroelastic modeling of flapping wing in hover" Journal of American Institute of Aeronautics and Astronautics, vol. 51, pp. 567–583, February 2013.

175. P. Masarati, M. Morandini, G. Quaranta, D. Chandar, B. Roget, and J. Sitaraman, “Tightly coupled CFD/multibody analysis of flapping-wing micro-aerial vehicles”, Proceedings of 29th AIAA Applied Aerodynamics Conference, pp. 1-12, June 2011.
176. C. Farhat, and V. K. Lakshminaryan, “An ALE formulation of embedded boundary methods for tracking boundary layers in turbulent fluid–structure interaction problems”, Journal of Computational Physics, vol. 264, pp. 53–70, April 2014.
177. V. K. Lakshminarayan, and C. Farhat, “Nonlinear aeroelastic analysis of highly flexible flapping wings using an ale formulation of embedded boundary method”, Proceedings of 52nd AIAA Aerospace Sciences Meeting, pp. 1-20, January 2014.
178. A. Altememe1, O. J. Myers, and A. Hall, “Preliminary design and computational fluid dynamic analysis of flapping wing of micro aerial vehicle for low Reynolds numbers regime”, International Journal of Aeronautics and Aerospace Engineering, vol. 1, pp. 36-45, May 2019.
179. C. Beker, A. E. Turgut, K. B. Arikan, AND D. F. Kurtulus, “Fluid-structure interaction analysis of a four-bar flapping wing mechanism”, Proceedings of IX ECCOMAS Thematic Conference on Smart Structures and Materials, pp. 1-11, July 2019.
180. W. B. Tay, B. W. van Oudheusdena, and H.Bijla, “Numerical simulation of a flapping four-wing micro-aerial vehicle” Journal of Fluids and Structures, vol. 55, pp. 237-261, May 2015.
181. H. Liu, T. Nakata, N. Gao, M. Maeda, H. Aono, and W. Shyy, “Micro air vehicle-motivated computational biomechanics in bio-flights: aerodynamics, flight dynamics and maneuvering stability”, Acta Mechanica Sinica, vol. 26, pp. 863–879, December 2010.
182. S. Deng, M. Percin, B. W. van Oudheusden, H. Bijl, B. Remes and T. Xiao, “Numerical simulation of a flexible x-wing flapping-wing micro air vehicle”, vol. 55, pp. 1-12, May 2017.
183. J. E. Rubio, U. K. Chakravarty, “An Investigation of the aerodynamic performance of a biomimetic insect-sized wing for micro air vehicles”, Proceedings of ASME International Mechanical Engineering Congress and Exposition, pp. 1-7, February 2017.

184. K. Takizawa, T. E. Tezduyar, and N. Kostov, “Sequentially-coupled space–time FSI analysis of bio-inspired flapping-wing aerodynamics of an MAV”, Computational Mechanics, vol. 54, pp. 213–233, February 2014.
185. D. Ishihara, T. Horie, and T. Niho, “Fluid-structure interaction analysis for the aerodynamic contribution to the passive pitching motion of dipteran flapping wings”, Proceedings of the 8th Asian-Pacific Conference on Biomechanics, pp. 66, September 2015
186. T. Nakata, R. Noda, and H. Liu, “Fluid-structure interaction enhances the aerodynamic performance of flapping wings: a computational study”, Journal of Biomechanical Science and Engineering, vol.13, pp. 1-9, May 2018.
187. D. Ishihara and S. Yoshimura, “A monolithic approach for interaction of incompressible viscous fluid and an elastic body based on fluid pressure Poisson equation”, International Journal for Numerical Methods in Engineering, vol.64, pp.167-203, April 2005.
188. D. Ishihara and T. Horie, “A projection method for the interaction of an incompressible fluid and a structure using new algebraic splitting, Computer Modeling in Engineering and Sciences”, vol.101, pp.421-440, 2014.
189. D. Ishihara and T. Horie, “A monolithic method for fluid-shell interaction based on consistent pressure Poisson equation”, Proceedings of the First International Conference on Computational Methods for Coupled Problems in Science and Engineering, pp. 1-17, 2005.
190. D. Ishihara, T. Horie, and T. Niho, “A Three-dimensional computational study on the fluid-structure interaction cause of wing pitch changes in insect flapping flight”, Proceedings of the 9th World Congress on Computational Mechanics and 4th Asian Pacific Congress on Computational Mechanics, pp.27-28, 2010.
191. D. Ishihara, T. Horie, and T. Niho, “Parallel monolithic approach for shell-fluid interaction analysis of flapping flexible wing”, Proceedings of 4th Korea-Japan COSEIK-JSCES Workshop on Computational Engineering, pp.26-27, May 2010.
192. D. Ishihara, T. Horie, T. Niho, and A. Baba, “Finite element analysis for coupled problems of structure, fluid and electrostatic field in micro cantilever beam”, Proceedings of 2nd International Workshops on Advances in Computational Mechanics, pp. 121, 2010.

193. D. Ishihara, T. Horie, T. Niho, and A. Baba, “Finite element analysis for interaction problems of structure, fluid and electrostatic field in micro cantilever beams”, Proceedings of KSME-JSME Joint Symposium on Computational Mechanics and Computer Aided Engineering, pp.255-260, 2012.
194. D. Ishihara and T. Horie, “A consistent projection method for monolithic fluid-structure interaction systems”, Proceedings of the V International Conference on Coupled Problems in Science and Engineering, pp. 1, August 2013
195. D. Ishihara, T. Horie, and T. Niho, “Hierarchically decomposed finite element analysis of the structure-fluid-electrostatic interaction”, Proceedings of the KSME-JSME Joint Symposium on Computational Mechanics and Computer Aided Engineering, pp. 20-21, 2015.
196. D. Ishihara, T. Horie, and T. Niho, and A. Baba, “Finite element analysis using a hierarchal decomposition for the interaction of structure, fluid and electrostatic field in MEMS”, Proceedings of the VI International Conference on Coupled Problems in Science and Engineering, pp. 1023-1028, May 2015.
197. D. Ishihara, S. Murakami, M. Araki, and T. Horie, “Fluid–structure interaction design of micro flexible wing mimicking insect flapping flight”, Proceedings of the 12th World Congress on Computational Mechanics, pp. 1764, July 2016.
198. D. Ishihara, N. Ohira, M. Takagi, S. Murakami, and T. Horie, “Design of micro flexible wing mimicking insect flapping flight using fluid-structure interaction analysis”, Proceedings of the JSME-KSME Joint Symposium on Computational Mechanics and Computer Aided Engineering, pp. 111-112, 2017.
199. P. C. Ramegowda, D. Ishihara, T. Niho and T. Horie, “A Finite element approach for a coupled numerical simulation of fluid–structurte–electric interaction in MEMS”, Proceedings of the VIIth International Conference on Computational Methods for Coupled Problems in Science and Engineering, pp. 999-1007, June 2017.
200. P. C. Ramegowda, D. Ishihara, R. Takata, T. Niho, and T. Horie, “Fluid-Structure and Electric Interaction Analysis of Piezoelectric Flap in a Channel

Using a Strongly Coupled FEM Scheme", Proceedings of the 6th European conference on computational mechanics, pp. 1-12, June 2018.

201. P. C. Ramegowda, D. Ishihara, R. Takata, T. Niho, and T. Horie, "Triply coupled analysis method for thin flexible piezoelectric bimorph in fluid", Proceedings of 8th International Conference on Computational Methods for Coupled Problems in Science and Engineering, pp. 1-11, June 2019.
202. M. Onishi and D. Ishihara, "Computational fluid-structure interaction framework for simulating characteristic deformations in insect flapping wings", Proceedings of 9th International Conference on Computational Methods for Coupled Problems in Science and Engineering, pp. 1-6, June 2021.
203. P. C. Ramegowda, D. Ishihara, "Hierarchically decomposed finite element method for the coupled four fields of the fluid-structure–piezoelectric–circuit interaction", Proceedings of 9th International Conference on Computational Methods for Coupled Problems in Science and Engineering, pp. 1-12, June 2021.
204. D. Ishihara, "Efficient strong coupling method for fluid-structure interaction based on explicit method for structure and semi-implicit method for fluid", Transactions of the Japan Society of Mechanical Engineers, vol. B 70, pp.3098-3105, December 2004 (in Japanese).
205. D. Ishihara, S. Yoshimura, and G. Yagawa, "Multi-step strong coupling method for interaction of incompressible viscous flow and an elastic body", Transactions of the Japan Society of Mechanical Engineers, vol. B 68, pp.2451-2459, 2002 (in Japanese).
206. D. Ishihara and T. Horie, "Development of strong coupling method considering non-conforming mesh on fluid-structure interface", Transactions of the Japan Society of Mechanical Engineers, vol. B 71, pp.1346-1353, 2005 (in Japanese).
207. D. Ishihara and S. Yoshimura, "Monolithic approach for fluid-structure interaction based on consistent pressure Poisson equation", Transactions of the Japan Society of Mechanical Engineers", vol. B 71, pp.1565-1572, June 2005 (in Japanese).

208. D. Ishihara and T. Horie, “Fluid-structure interaction modeling of insect flight”, Transactions of the Japan Society of Mechanical Engineers, vol. B 72, pp.1410-1417, 2006 (in Japanese).
209. D. Ishihara, S. Kanei, S. Yoshimura, and T. Horie, “Efficient parallel analysis of shell-fluid interaction problem by monolithic method based on consistent pressure poisson equation”, Transactions of the Japan Society of Mechanical Engineers, vol. A 73, No. 724, pp. 34-41, 2007 (in Japanese).
210. D. Ishihara and J. Matsumoto, “Incremental formulation of pressure based method for fluid-rigid body interaction using intermediate variable and its verification”, Transactions of the Japan Society of Mechanical Engineers, vol. B 74, pp.2419-2425, December 2008 (in Japanese).
211. D. Ishihara, A. Kubota, T. Horie, T. Niho, and S. Yoshimura, “Development of strongly coupled method for interaction of structure, incompressible viscous fluid and electrostatic field”, Transactions of the Japan Society of Mechanical Engineers, vol. A 74, pp.1068-1075, August 2008 (in Japanese).
212. D. Ishihara, S. Kanei, S. Yoshimura, and T. Horie, “Efficient parallel analysis of shell-fluid interaction problem by using monolithic method based on consistent pressure poisson equation”, Journal of Computational Science and Technology, vol.2, pp.185-196, January 2008.
213. D. Ishihara, T. Horie, and M. Denda, “A two-dimensional computational study on fluid-structure interaction cause of wing pitch changes in dipteran flapping flight”, The Journal of Experimental Biology, vol.212, pp.1-10, January 2009.
214. D. Ishihara, S. Yoshida, T. Shimura, T. Horie, and T. Niho, “Evaluation using dynamically scaled experiment of dipteran passive pitching motion caused by fluid-structure interaction”, Transactions of the Japan Society of Mechanical Engineers, vol. B 78, pp.300-310, February 2012 (in Japanese).
215. D. Ishihara and T. Horie, “Consistent projection method for the interaction of an incompressible fluid and a structure”, Transactions of the Japan Society of Mechanical Engineers, vol. A 79, pp.1161-1170, August 2013 (in Japanese).
216. D. Ishihara, T. Horie, T. Niho, and A. Baba, “Finite element analysis using hierarchal decomposition for interaction of structural, fluidic and

electrostatic fields in mems structural components", Transactions of the Japan Society of Mechanical Engineers, vol. A 79, No. 804, pp.1291-1302, August 2013 (in Japanese).
217. D. Ishihara and T. Horie, "Convergence evaluation on a projection method for the interaction of an incompressible fluid and an elastic structure", Transactions of the Japan Society for Computational Engineering and Science, vol.2013, pp. 1-7pages, 2013 (in Japanese).
218. D. Ishihara, T. Horie, and T. Niho, "Numerical study on aerodynamic effects in passive pitching dynamics of insect flapping wings", Transactions of the Japan Society of Mechanical Engineers, vol.80, 2014 (in Japanese).
219. D. Ishihara, T. Horie, and T. Niho, "Hierarchal decomposition for the structure–fluid–electrostatic interaction in a microelectromechanical system", Computer Modeling in Engineering and Sciences, vol.108, pp.429-452, 2015.
220. M. Onishi, and D. Ishihara, "Passive motions and aerodynamic performance of insect's flapping wings simulated using the pixel wing model and the strong coupling method", Proceedings of the 40th JSST Annual International Conference on Simulation Technology, pp. 1-4, September 2021.
221. S. Yoshimura, D. Ishihara, "Integrated cae system for structural design based on object-oriented approach and its application to micromachine design", Journal of Japan Society for Design Engineering, vol.39, pp.584-593, 2004 (in Japanese).
222. D. Ishihara, S. Kanei, and T. Horie, "Development of monolithic method for shell-fluid interaction based on consistent pressure Poisson equation", Transactions of the Japan Society of Mechanical Engineers, vol. A 72, pp.377-384, April 2006 (in Japanese).
223. T. Niho and T. Horie, "Performance of coupled parallel finite element analysis in grid computing environment", Lecture Notes in Computer Science, vol. 4759, pp. 262-270, 2008.
224. D. Ishihara, Y. Yamashita, T. Horie, and T. Niho, "A Study on the Passive Pitching and Lift Generation in Crane-Fly's Flight", Transactions of the Japan Society of Mechanical Engineers, vol. B 76, pp.601-607, 2010 (in Japanese).
225. D. Ishihara, A. Goto, M. Onishi, T. Horie, and T. Niho, "Element-quality-based stiffening for the pseudoelastic moving mesh technique", International Journal of Computational Methods, vol. 17, 1850146-33, October 2020.

226. D. Ishihara, A. Goto, M. Onishi, T. Niho, and T. Horie, “Pseudoelastic mesh moving using a general scenario of the selective mesh stiffening”, Journal of Advanced Simulation in Science and Engineering, vol. 6, pp. 67-74, March 2019.
227. T. E. Tedzduyar, S. Mittal, S. E. Ray, and R. Shih, “Incompressible flow computations with stabilized bilinear and linear equal–order–interpolation velocity–pressure elements”, Computer Methods in Applied Mechanics and Engineering, vol. 95, pp. 221–242, March 1992.
228. K. J. Bathe and E. N. Dvorkin, “A four-node plate bending element based on Mindlin/Reissner plate theory and a mixed interpolation”, International Journal for Numerical Methods in Engineering, vol. 21, pp. 367–383, 1985.
229. N. Noguchi and T. Hisada, “Sensitivity analysis in post-buckling problems of shell structures”, Computer and Structure, vol. 47, pp. 699–710, June 1993.
230. Q. Zhang and T. Hisada, “Analysis of fluid-structure interaction problems with structural buckling and large domain changes by ALE finite element methods”, Computer Methods in Applied Mechanics and Engineering, vol. 190, pp. 6341–6357, September 2001.
231. B. J. Kim and E. Meng, “Review of polymer MEMS micromachining”, Journal of Micromechanics and Microengineering, vol. 26, pp. 013001-21, November 2015.